

Aus dem Departement für Physik
Universität Freiburg (Schweiz)



Surface scientific aspects of materials relevant to tribology

Inaugural-Dissertation

zur Erlangung der Würde eines
Doctor rerum naturalium
der Mathematisch-Naturwissenschaftlichen Fakultät
der Universität Freiburg in der Schweiz

vorgelegt von

Michael Biemann

aus Rechthalten (Schweiz)

Nummer der Dissertation: 1467
Hausdruckerei Universität Freiburg
2004/05

Von der Mathematisch-Naturwissenschaftlichen Fakultät der Universität Freiburg in der Schweiz angenommen, auf Antrag der Herren

Prof. Dr. Antoine Weis, Universität Freiburg (Präsident der Jury)

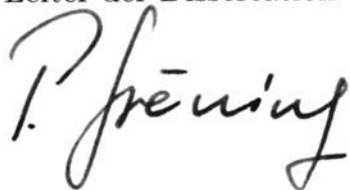
Dr. Pierangelo Gröning, Empa Thun (Leiter der Dissertation)

Prof. Dr. Louis Schlapbach, Empa Dübendorf, Universität Freiburg (Koreferent)

Prof. Dr. Nicolas Spencer, ETH Zürich (externer Gutachter)

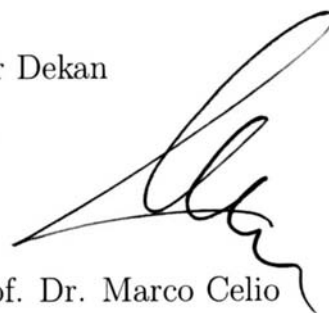
Freiburg, den 23. Dezember 2004

Der Leiter der Dissertation

A handwritten signature in black ink, appearing to read 'P. Gröning', written in a cursive style.

Dr. Pierangelo Gröning

Der Dekan

A handwritten signature in black ink, appearing to read 'M. Celio', written in a cursive style.

Prof. Dr. Marco Celio

Abstract

The presented work is treating surface scientific aspects of selected materials related to tribology. Tribology is one of the oldest problems humans try to master. It is highly interdisciplinary and there is probably no topic, where so much effort has been put into to gain a deeper understanding. But still, while the role of the surface in tribology is perceived and accepted, a general understanding is lacking. The experimental work in this thesis consist of two main parts. The first part discusses the plasma treatment of silver bond pads. This topic is motivated by the so called wirebonding process, a standard in industry for the connection of chip die to the supporting chip enclosure, where the tribology at the interface has a mayor influence. The state of the surface has a direct impact on failure rate and processing speed of this technique, two factors with immediate economical implications. According to experience, H₂/Ar plasma treatments of bond pads prior to wirebonding is known to improve the quality and reproducibility of the process considerably. This is attributed to a cleaning and passivation effect. We examined the impact of H₂ plasma treatments on silver by surface scientific methods to investigate the nature of these empirically observed effects. By the so called bondability analyzer - a newly developed tool from our group based on the wirebonding process - the effect of these treatments could be observed directly under normal processing conditions while Photoelectron Spectroscopy gave us vital information about the impact of the corresponding treatment to the state of the surface.

The second part consist of works related to quasicrystals. Quasicrystals are seen - from an application perspective - as an interesting candidate for tribocoatings due to their very special surface properties (low surface energy, low wear rate, low friction coefficient, low thermal and electric conductivity) . But these systems are complex in every aspect and in general poorly understood. The global understanding does by far not reach the level as for classic crystallographic systems, primary because of the lack of translational symmetry. The work on QC's therefore is fundamental, with the bigger scope of gaining a deeper understanding on QC's as to disentangle the structural and chemical influences on their properties. We investigated copper thin films on i-AlPdMn 5f single crystals on the quest of finding a single element quasicrystal model system by substrate/evaporant layer interaction. Such a system would greatly reduce the complexity we are dealing with and might offer new insights in how atomic order, electronic structure and properties of QC's are interconnected. In the same context, we studied surface alloying of copper with the AlPdMn surface. This topic is oriented towards applications, as the performance of a coating is not only defined by it's surface, the interface of the coating to the substrate has also a dominant role as it defines film adhesion.

The formation of QC thin film coatings by thermal evaporation of the constituents

was a further task during this thesis. The work consisted of constructing a preparation chamber for the deposition of ternary alloys, either by sequential evaporation and subsequent interdiffusion or by coevaporation of the elements. Although a big part of the time was devoted to this project, the results are not presented here. Preliminary results by Photoelectron Spectroscopy and Nanoindentation show a behavior expected for a QC phase but although promising, these results are no unambiguous proof for QC phase formation. Our analytical methods are limited on polycrystal samples as they can only yield conclusive prove of the formation of a QC phase on single crystals surfaces. These samples are analyzed by other external coworkers and unfortunately the results are still pending. But the now accessible experimental possibilities are very valuable in the future.

Shortly resuming, the presented works find themselves motivated by the topic of tribology, either from a very fundamental or from an applied point of view. It underlines the importance of the surface and justifies the study of clean, well ordered model systems. The thesis first introduces the reader superficially in the vast topic of tribology to motivate a surface scientific approach. In the experimental section, the necessary tools and methods are presented as to give the unacquainted the necessary background information on the experimental aspects of the thesis. The introductory chapters are completed by an introduction in quasicrystals. As these materials are very exotic and most readers might know about quasicrystals only from hearsay, it gives some very fundamental basics. These chapters are followed by the publications evolving from the experimental work during this thesis.

Zusammenfassung

Die vorgestellten Arbeiten behandeln oberflächenphysikalische Aspekte ausgewählter Materialien deren Anwendung aus tribologischer Sicht relevant sind. Tribologie ist ein hochgradig interdisziplinäres Thema und eines der ältesten Probleme, die den denkenden Menschen beschäftigen. Obwohl die Wichtigkeit der Oberfläche in der Tribologie wahrgenommen und akzeptiert wird, bleibt das Verständnis bruchstückhaft. Dies bildet die Motivation dieses Problem mit oberflächenphysikalischen Methoden anzugehen. Die in dieser Dissertation vorgestellten Arbeiten bestehen aus zwei thematischen Teilen: Der erste Teil diskutiert die Plasmabehandlung von Silber Bond Pads. Die tribologischen Eigenschaften der Oberfläche eines Bond Pads spielt eine entscheidende Rolle beim Prozess des Drahtbondens, ein Standardprozess in der Halbleiterindustrie, um den Chip Die mit der Aussenwelt, dem Chip Träger zu verbinden. Der Zustand der Oberfläche hat einen direkten Einfluss auf die Fehlerrate und die Prozessgeschwindigkeit - zwei Parameter, die sich unmittelbar ökonomisch niederschlagen. Vorbehandlungen durch H_2/Ar Plasma zeigen erfahrungsgemäss eine stark verbesserte Reproduzierbarkeit und Bondqualität. Dies wird auf eine Reinigung und Passivierung der Oberfläche zurückgeführt. Durch oberflächenphysikalische Methoden haben wir den Einfluss eines H_2 Plasmas auf Silber Oberflächen untersucht, um den physikalischen Bezug mit diesen Erfahrungswerten zu schaffen. Mit dem sogenannten Bondbarkeitsanalysator - einer in unserer Gruppe entwickelten Messmethode basierend auf dem Drahtbondprozess - konnte der Einfluss einer Behandlung direkt mit den relevanten Prozessparametern untersucht werden. Die Korrelation zu den zugrundeliegenden Oberflächenmodifikationen konnte mit Photoelektronenspektroskopie hergestellt werden.

Der zweite Teil der Arbeiten konzentriert sich auf Quasikristalle. Diese Materialien gelten in der Praxis als interessante Kandidaten für tribologische Beschichtungen aufgrund ihrer speziellen Eigenschaften (niedrige Oberflächenenergie, niedriger Abrieb, niedriger Reibungskoeffizient, niedrige thermische und elektrische Leitfähigkeit). Trotz des hohen Forschungsaufwandes ist der Grad des Verständnisses bei weitem nicht vollständig. Dies ist darauf zurück zu führen, dass diese Systeme hochgradig komplex sind (keine Translationssymmetrie, binäre und ternäre intermetallische Verbindungen) und andererseits darauf, dass es sich um ein eher junges System handelt. Die Wissenschaft beschäftigt sich erst seit der Entdeckung 1984 mit diesen neuartigen Materialien. Das Verständnis von Quasikristallen ist weit davon entfernt mit dem klassischer, kristalliner Systeme gleichzuziehen. Der Hauptgrund liegt darin, dass die theoretischen Konzepte sich häufig auf Translationssymmetrie stützen, welche bei Quasikristallen nicht existiert. Arbeiten mit Quasikristallen sind fundamental - mit dem Ziel, ein tieferes Verständnis zwischen atomarer Struktur, chemischer Zusammensetzung und deren Auswirkungen auf die physikalischen

chen Eigenschaften herzustellen. In diesem Zusammenhang wurden Nanometer dicke Kupferfilme auf ikosahedralen AlPdMn 5f Einkristallen untersucht. Diese Arbeiten wurden motiviert durch den Wunsch eines Modellsystems, bei dem sich strukturelle und elektronische Eigenschaften besser trennen lassen. Sollte es gelingen, über Substrat/Film-Wechselwirkung einem einzelnen Element die quasikristalline Struktur aufzudrängen, wäre dies das optimale Modellsystem - könnte so doch der Einfluss der atomaren Struktur auf die elektronische Struktur eines bekannten Systemes direkt studiert werden. Dies bildet die Basis für die Arbeiten von Kupfer auf QC Einkristallen. Im selben Zusammenhang wurde die Bildung einer intermetallischen Verbindung von Kupfer mit der ikosahedralen AlPdMn Oberfläche untersucht. Dies ist aus Anwendungssicht äusserst relevant - Beschichtungen sind nur so stark wie ihr schwächstes Glied - und oft ist dies die Verbindung der Schicht zum Trägermaterial.

Eine weitere Aufgabe war die Herstellung von quasikristallinen Dünnschichten durch thermisches Verdampfen. Für diese Arbeiten wurde eine Präparationskammer gebaut, die es uns erlaubt, ternäre intermetallische Verbindungen über sequentielle Abscheidung und Interdiffusion oder über Koevaporation herzustellen. Die vorläufigen Resultate dieser Arbeiten werden hier aber nicht präsentiert. Erste Resultate in der Photoelektronenspektroskopie zeigen ein Verhalten wie dies für QC's erwartet wird. Auch erste Indentationsmessungen sind vielversprechend. Aber leider sind dies nur Indizien, weil unsere Messmethoden die Bildung einer quasikristallinen Phase nur auf Einkristallen schlüssig nachweisen können. Diese Proben werden von externen Projektmitarbeitern weiter untersucht und die Resultate sind noch ausstehend. Nichtsdestotrotz sind die nun zur Verfügung stehenden präparativen Möglichkeiten enorm.

Zusammenfassend hängen die Arbeiten, so unterschiedlich sie auch thematisch sind, damit zusammen, dass sie sich mit Oberflächen befassen, deren Relevanz anwendungsorientiert in der Tribologie zu suchen ist. Die Oberfläche ist in dieser Thematik von entscheidender Bedeutung - definiert sie doch den Kontakt zwischen zweier Materialien und damit deren Wechselwirkung untereinander. In einem ersten Kapitel wird dem Leser die Wichtigkeit der Oberfläche in der Tribologie vor Augen geführt. Es soll die Motivation für unseren Ansatz, mit oberflächenphysikalischen Methoden solche Phänomene anzugehen, klar unterstreichen. Darauf folgend werden die experimentellen Methoden, die zur Anwendung kamen, vorgestellt, um dem unvertrauten Leser die verwendeten Techniken näher zu bringen. Abgeschlossen werden die Einleitungen mit einer kurzen Einführung über Quasikristalle. Da dieses Thema nur selten zum Grundwissen gehört, scheint eine informative Übersicht angebracht. Der eigentliche Hauptteil - die Vorstellung der wissenschaftlichen Forschung - schliesst diese Dissertation ab.

Contents

Preface	1
I Introductory Chapters	3
1 Tribology and Surfaces	5
1.1 Motivation	5
1.2 Macroscopic friction laws	6
1.3 Microscopic friction	6
1.4 Dry friction	6
1.4.1 Ag bond pads in wirebond pads	7
1.4.2 Quasicrystal surfaces	8
2 Experimental Methods	11
2.1 Introduction	12
2.2 Spectrometer and Preparation Chamber	12
2.3 Photoelectron Spectroscopy (PES)	14
2.3.1 X-Ray Photoelectron Spectroscopy (XPS)	15
2.3.2 Ultraviolet Photoelectron Spectroscopy (UPS)	16
2.3.3 X-Ray Photoelectron Diffraction (XPD)	18
2.4 Low Energy Electron Diffraction (LEED)	20
2.4.1 LEED from periodic crystals	21
2.4.2 LEED from quasiperiodic crystals	22
2.5 Thin Film evaporation	24
2.5.1 Vapor pressure	24
2.5.2 Al cold lip evaporator	26
2.5.3 E-Beam evaporation	26
3 Introduction Quasicrystals	31
3.1 History	32

3.2	What is different to classical crystals?	32
3.2.1	Theoretical description of classical crystals	32
3.2.2	Theoretical description of quasicrystals	32
3.3	Tilings	34
3.3.1	Penrose Tilings	34
3.3.2	Cluster model - the quasi unit-cell	36
3.4	Embedding	37
3.4.1	The Fibonacci sequence	37
3.4.2	Extension to n-Dim	38
3.4.3	Phasons	40
3.5	Classification of QC Systems	41
3.5.1	Classification by structure	41
3.5.2	Classification by composition (selection)	42
3.6	Physical Properties	42
3.7	Photoemission from QC's : AlPdMn	44
3.7.1	X-ray Photoelectron Spectroscopy	44
3.7.2	Ultraviolet Photoemission Spectroscopy	46
3.7.3	X-ray Photoelectron Diffraction	46
3.8	QC's are electronically stabilized	48

II Oxidation and Reduction of Ag by Plasma treatment 55

4	H₂ plasma treatment of silver contacts: impact on wirebonding performance	57
4.1	Introduction	58
4.2	Experimental	60
4.2.1	Equipment	60
4.2.2	Sample Preparation	61
4.3	Results and Discussion	61
4.3.1	Oxidation	61
4.3.1.1	QCM measurements	61
4.3.1.2	Photoelectron spectroscopy measurements	62
4.3.2	H ₂ plasma treatments	62
4.3.2.1	QCM measurements	62
4.3.2.2	Photoelectron spectroscopy measurements	64
4.4	Conclusions	65
4.5	Acknowledgements	66

5	AgO investigated by Photoelectron Spectroscopy: Evidence for mixed valence	69
5.1	Introduction	69
5.2	Experimental	71
5.3	Results and Discussion	72
5.3.1	QCM	72
5.3.2	XPS	73
5.3.3	UPS	76
5.3.4	Stability	76
5.4	Discussion and Summary	77
5.5	Acknowledgements	78
III	Growth of Cu thin films on i-AlPdMn 5f single crystals	81
6	Evidence for strained cubic structure in 1D quasiperiodic buckling of Cu thin films on icosahedral AlPdMn	83
6.1	Introduction	85
6.2	Experimental	86
6.3	Results and Discussion	87
6.4	Summary	97
6.5	Acknowledgements	98
7	Formation of Al₄Cu₉ on the 5 fold surface of icosahedral AlPdMn	101
7.1	Introduction	102
7.2	Experimental	102
7.3	Results and Discussion	104
7.3.1	XPS Measurements	104
7.3.2	XPD Analysis	105
7.3.3	LEED Analysis	107
7.4	Summary	108
7.5	Acknowledgements	109
	Danksagung	113
	Curriculum vitae	115

Preface

Nothing shocks me. I'm a scientist.

Harrison Ford (1942 -), as Indiana Jones

This thesis is based on research carried out at the Department of Physics at the University of Fribourg, Switzerland and at Empa Materials Science and Technology, Thun, Switzerland.

Currently published articles included in this thesis are:

1. AgO investigated by photoelectron spectroscopy: Evidence for mixed valence
M. Biemann, P. Schwaller, P. Ruffieux, O. Gröning, L. Schlapbach, and P. Gröning
Phys. Rev. B **65**, 235431 (2002)
2. H₂ plasma treatment of silver contacts: impacts on wirebonding performance
M. Biemann, P. Ruffieux, P. Schwaller, P. Sudan, L. Schlapbach and P. Gröning
J. Electron. Mat. (**31**)12, 1316 (2002)

Currently unpublished articles included in this thesis are:

1. Cu on AlPdMn5f paper
M. Biemann, J. Ledieu, O. Gröning, P. Ruffieux, R. Fasel, R. Widmer, D. Naumović, and P.A. Gröning
To be submitted
2. Formation of Al₄Cu₉ approximant on the 5 fold surface of icosahedral AlPdMn
M. Biemann, P. Ruffieux, O. Gröning, R. Fasel, A. Barranco, R. Widmer, and P.A. Gröning
To be submitted

Part I
Introductory Chapters

Chapter 1

Tribology and Surfaces

”tribology :

the study of the interaction of sliding surfaces. It includes three subjects: friction, wear, and lubrication. There is a difficulty in that friction is generally characterized as a branch of physics or mechanical engineering, wear is part of the material science of metallurgy, while lubrication is a branch of chemistry....” (Encyclopedia Britannica)

1.1 Motivation

Tribology is a multi-disciplinary subject, embracing different branches. Due to its high economical impact, there is a very strong interest in the topic. It is estimated that one third of worlds energy consumption can be related to friction in one form or another. While friction might be a highly desirable phenomenon in some applications (welding, brake discs, etc), the reduction of friction by surface tailoring and/or use of proper lubricant systems is highly beneficial in other fields (artificial joint implants, bearings, dry lubrication systems). The study of tribological phenomena goes back further than recorded history and was for instance depicted in old Egyptian paintings. Its importance was therefore already realized in ancient times [1]. Different domains of tribological behavior can be identified, each having its proper characteristics. In this chapter, we want to motivate our works and relate them to the aspects of tribology interesting for a surface scientist: Dry friction. It is the special branch of tribology, where eventual lubricating systems do collapse or are completely absent and the surfaces involved get in contact to each other. This is an ultimate surface scientific problem, as the physical contact between to bulk systems involves the two surfaces of the bodies. Furthermore, it is a problem at the μm to nm scale, as the physical contact is established at some asperities of the individual surfaces only. While surface corrugation is an important factor in tribosystems, we focus on single asperity contacts. The study of single crystal surfaces can address fundamental questions about structural, chemical and electronic influences of the two material brought

to intimate contact.

1.2 Macroscopic friction laws

The macroscopic friction laws have been established by Leonardo da Vinci, Amontons, Euler and Coulomb [1]. These laws are the ones generally taught in high school education.

$$F \neq f(A) \quad \text{da Vinci's Law}$$

$$F = \mu \cdot N \quad \text{Amontons Law}$$

$$F \neq f(v) \quad \text{Coulomb's Law}$$

Leonardo da Vinci made experiments with wooden blocks on an inclined plane and came to the conclusion, that the friction force is independent of the area of contact. Amontons proved the friction force to be proportional to the normal load, the proportionality constant μ was named *friction coefficient*. Coulomb found the friction to be independent of sliding velocity. Especially da Vinci's and Coulomb's laws contradict our intuition about how friction should behave. This was only resolved in the 20th century by studies on microscopic friction.

1.3 Microscopic friction

In 1950, Bowden and Tabor published their book which served as the standard book for tribology for decades [2]. They found, that one needs to distinguish between macroscopic area of contact and the area of real contact. Only a small percentage of the total surface area is involved in the contact of two bodies. The real area of contact depends on the normal load mainly, which alleviates the paradoxon to our intuition of da Vinci's law: The real area of contact is the same and depends only on the normal force no matter on which side the wooden block is sliding. It is established so that the physical load can be supported by the very few asperities in intimate contact. These asperities might deform plastically at first, leading to a growth of contact area, until the contact pressure is distributed over a large enough area to be supported elastically [3] as presented in Fig. 1.1.

1.4 Dry friction

There are many domains discernable for frictional processes, mostly involving lubricants. The idea of lubricants is to prevent direct physical contact between the surfaces under

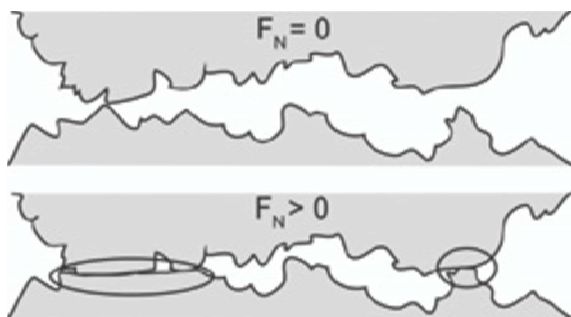


Figure 1.1: Establishing Contact on a micrometer scale: Asperities are plastically deformed to increase the real area of contact until the physical load can be supported by elastic deformations. The real area of contact is therefore directly connected to the normal force F_N and the material properties. The zones of plastic deformation are marked by circles.

consideration, and therefore, friction is mainly defined by the friction in the lubricating film [4]. If one approaches the surfaces further, only a few monolayers of lubricant remain between the surfaces. In this case one speaks of boundary lubrication. The most interesting case for us is, when the lubrication film fails and the two surfaces get into intimate contact: dry friction. It is this case, where the properties of the surfaces involved are most important. Technologically, this case arises in lubrication failure or for instance in space/UHV applications, when no liquid lubricant can persist. Even though there exist solid state lubricants (like MoS_2) these lubricating layers can be squeezed out of the contact area under lateral movement and high load, leading to direct physical contact of the two surfaces. This is in general also true for present contaminant layers on a surface, which can act as a lubricant [4, 5]. In this case, the material properties of the surface dominate and effects as microwelding, interdiffusion and alloying may occur, defining friction and wear characteristics. It is this so called single asperity contact region we are focussing on. Parameters like pressure, temperature, chemistry, electronic and crystal structure define how the materials in intimate contact will interact chemically (bonding) and spatially (interdiffusion). It is in this region, where the approach of studying well defined, clean surfaces makes sense and can give a fundamental understanding of macroscopical behavior based on effects occurring on the very local scale. We will address two systems with a different scope:

1.4.1 Ag bond pads in wirebond pads

In wirebonding, friction is a welcome and necessary process. The wirebonding process can be grossly described as a high pressure/high temperature regime of two surfaces in contact. Two surfaces are brought to intimate contact and contact pressures in the GPa regime

are established. The two surfaces are then actuated with ultrasonic frequency. Frictional heating leads to interdiffusion and welding of atoms close to the interface. The state of the two surfaces strongly influences this process. We investigate the chemical nature of the surface by XPS (X-ray Photoelectron Spectroscopy) and the surface termination by ARUPS (Angular Resolved Photoemission Spectroscopy). The frictional behavior is analyzed by a so called thermosonic bondability analyzer. We further elaborate how plasma treatment of a specific system can greatly improve the performance of such a tribocontact and what physical processes lead to this behavior.

1.4.2 Quasicrystal surfaces

From an engineers point of view, it is known that quasicrystal surfaces do exhibit an interesting tribological behavior. They have a low surface energy, low wear and low friction under certain conditions. The interest in QC's with respect to tribology therefore generally stems from an application as tribocoating. The interconnection between these facts and a deeper understanding from the materials properties from a fundamental point of view are very limited. This problem arises among others from the fact that QC's are extremely complex in every aspect. Mostly, stable quasicrystals are binary or ternary alloys, rising the difficulty of understanding considerably. Moreover, the completely different structure - being highly ordered but not offering translational symmetry - poses a challenge for theoretical approaches. Using quasicrystals for the purpose of tribocoatings therefore remains to some extent to be trial-and-error. It is the task of a surface scientist to push the level of understanding to the point where the deeper understanding let's us engineer the systems as to react in a predictable manner. The development of a connection between systematic understanding of the surface and reaction in intimate contact is a prerequisite for this task. Therefore, it is our motivation to find ways of producing model surfaces to gain such an understanding. For quasicrystals, the perfect model system would be a single element ordering in a QC phase with very well known properties. No such element is known or such a phase might not exist. But as a thin film in a low coverage regime, surface/film interactions might mediate QC ordering to the film material. This is the basis of the work related to Cu films on i-AlPdMn presented later.

References for Chapter 1

- [1] D. Dowson, *History of Tribology*, 2nd edition, (Longman, New York, 1998)
- [2] F.P. Bowden, D. Tabor, *The friction and lubrication of solids*, (Clarendon Press, Oxford, first published 1950)
- [3] J.H. Dietrich, B.D. Kilgore: *PAGEOPH* **143**, 283 (1994)
- [4] B.N.J. Persson, *Sliding Friction: Physical Principles and Applications*, (Springer, Berlin, 1998)
- [5] B. Bhushan, Ed. *Handbook of Micro/Nano Tribology*, 2nd Edition, (CRC Press, Washington, 1999)

Chapter 2

Experimental Methods

It is the purpose of this chapter to present the unacquainted reader the experimental methods and machinery applied throughout this work. In this section, questions related to analysis and surface preparation are addressed. To the reader familiar with those methods, this section may be skipped as it does only contain the basic tools for the understanding of the experimental contents and conclusions of this thesis.

"I have not failed, I have just found 10'000 ways that won't work"

Thomas Edison

"The best way to escape from a problem is to solve it."

Alan Saporta

2.1 Introduction

2.2 Spectrometer and Preparation Chamber

All experiments were performed in a modified photoelectron spectrometer of Omicron Nanotechnology GmbH. The vacuum and gas system is not presented for sake of simplicity. One of the main tasks of this PhD thesis was the planing and construction of a new preparation chamber, denoted Prep. 2 in Fig. 2.1, and a multi purpose sample manipulator for this chamber.

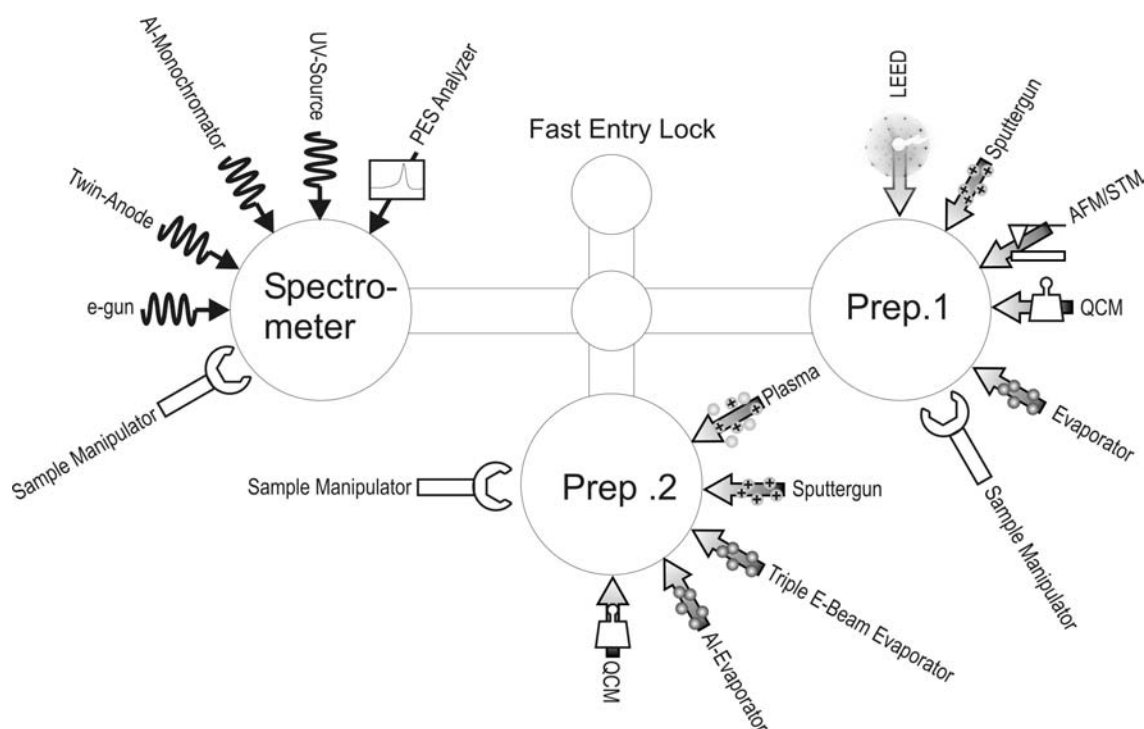


Figure 2.1: Schematic description of the surface analysis system. The individual available methods are described in this section.

- Analysis Chamber** : The analysis chamber basically consists of a commercial Omicron Photoelectron Spectrometer based on an EA 125 HR electron analyzer. The spectrometer is modified for Angular Resolved measurements through a manipulator offering the possibility to orient the sample with respect to the analyzer (and therefore with respect to the measured sample normal). As photon sources we have non-monochromatized Mg $K\alpha$ X-rays (1253.6eV), monochromatized Al $K\alpha$ X-rays (1486.6eV) and He I radiation (21.2eV) from a gas discharge lamp at our disposition as well as an e^- -gun for sample flooding and auger measurements .

- **Preparation Chamber 1** : This Chamber consists mainly of the commercial UHV AFM/STM and LEED system of Omicron Nanotechnology GmbH. Additionally, Ar^+ Ion sputtering and sample heating can be performed as well as simple evaporation tasks.
- **Preparation Chamber 2** : Sample production and treatment allowing for the simultaneous deposition of up to 4 elements on a rotatable, cool/heatable sample manipulator. This new chamber is denoted as Prep. 2 and offers very versatile possibilities for sample production and treatment. It offers the possibility of evaporating Al through a commercial Al-evaporator and three other elements by means of a commercial E-Beam evaporator with ion-flux control (EFM3T from Omicron Nanotechnology GmbH). Thickness calibration is accomplished by a Quartz Crystal Monitor (QCM) which can be placed at the sample position. The chamber features also an Electron Cyclotron Resonance (ECR) Plasma head for Plasma treatments with different gases.
- **Fast Entry Lock** : Offers the fast possibility to introduce and remove samples without breaking vacuum of the main chambers.

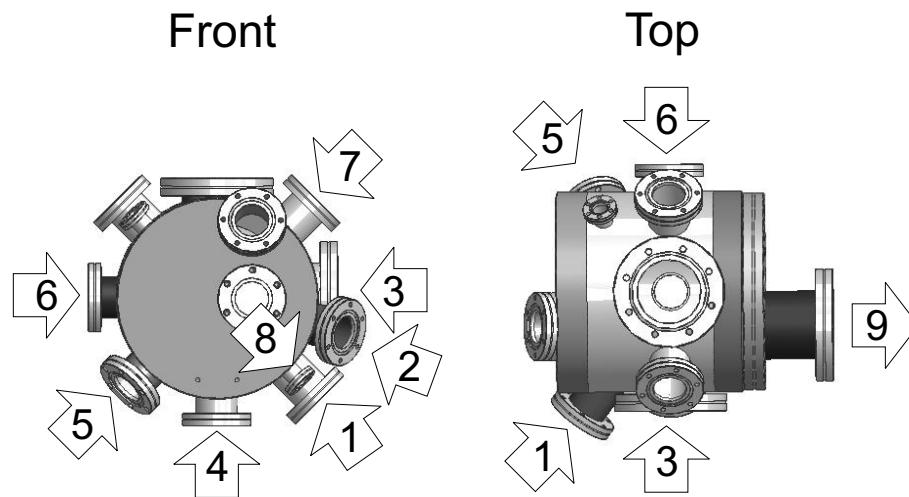


Figure 2.2: Front and Top view of Preparation Chamber 2 for thin film deposition and treatment. The components are as follows: 1) Al-evaporator 2) Triple E-Beam evaporator with ion flux control 3) ECR-Plasma head 4) Quartz Crystal Thickness Monitor 5) Ion-Pump 6) Rotatable, cool/heatable sample manipulator 7) Ar^+ Ion sputter gun 8) Baratron pressure gauge for mbar-pressures (Plasma) 9) Transfer to Fast Entry Lock/Analysis Chamber/Preparation Chamber 1

2.3 Photoelectron Spectroscopy (PES)

The name photoelectron spectroscopy comprises many methods based on the same concept: A sample is illuminated by photons to excite electrons by means of the photoelectric effect [1]. These electrons are partially emitted, collected and analyzed with respect to their kinetic energy. The energy of the radiation to excite the sample lies in general in the 10-1500eV range. Due to large scattering of photoelectrons created by such an excitation, the inelastic mean free path is quite small and follows approximately a universal curve. As depicted in Fig. 2.3, one can clearly see that PES methods are surface sensitive techniques, probing only the top few nm of a surface and the sample depth depends strongly on the kinetic energy of the electrons and also on the interlayer distance d of the sample. The inelastic mean free path can be approximated by the formula [2]:

$$\Lambda[\text{\AA}] = \frac{538 \cdot d}{E_{kin}^2[eV]} + 0.13 \cdot \sqrt{d^3 \cdot E_{kin}[eV]} \quad (2.1)$$

In a first approximation, the first term in equation 2.1 can be neglected in the kinetic energies relevant for XPS (50-2000eV). Therefore, the mean free path can be approximated as follows:

$$\Lambda(E_{kin}) \propto \sqrt{E_{kin}} \quad (2.2)$$

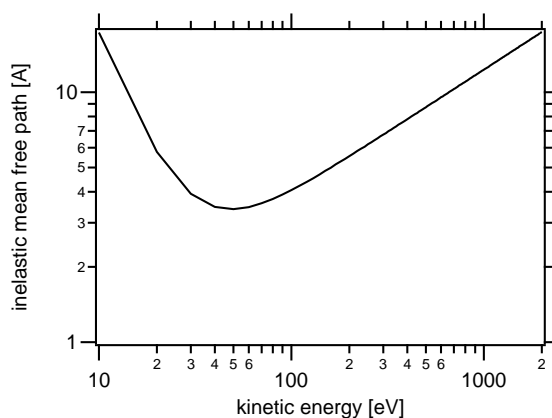


Figure 2.3: Electron mean free path as a function of kinetic energy in the range of 10eV - 2keV

The binding energy of the collected Photoelectrons in the solid can be calculated by analyzing their kinetic energy and using the following formula:

$$E_B = h \cdot \nu - E_{kin} - \phi_{Analyzer} \quad (2.3)$$

Please note, that in the workfunction ϕ_{Sample} is not part of this formula. Effectively, the kinetic Energy of the Photoelectrons as measured by the Analyzer are independent of ϕ_{Sample} and therefore an apriori knowledge of ϕ_{Sample} is not necessary.

2.3.1 X-Ray Photoelectron Spectroscopy (XPS)

XPS has matured from a specialized method to study stainless steel in the late sixties [3] to a well established tool in applied and fundamental research. Standard excitation sources for XPS are Mg $K\alpha$, Al $K\alpha$ or Si $K\alpha$ lines. The emitted photoelectrons give information about the elemental composition within the analysis depth through the characteristic energies and intensity distribution of the core levels and Auger lines. These binding energies of the core levels can differ from their values in a single elemental, bulk sample. Such differences derive from the specific chemical bonding state and coordination the element is subjected to and is conveniently referred to as 'chemical shift'. While this shift is not unique in general, it is a very valuable tool to investigate the surface chemical composition of a sample and is well tabulated for special systems. Hence one refers to PES also as Electron Spectroscopy for Chemical Analysis (ESCA). The intensity detected by the electron energy analyzer is given by the relationship:

$$I \propto n \cdot \sigma \cdot \lambda(E_{kin}) \cdot T(E_{kin}) \cdot \cos(\theta) \quad (2.4)$$

where n is the atom density, σ the photoionisation cross section, $T(E_{kin})$ the transmission function of the analyzer and θ the emission angle with respect to the sample normal. In our works, we used a EA125 analyzer from Omicron Nanotechnology. The transmission function of this analyzer is described in [4]. Quantitative analysis can be performed by using the respective cross section, Transmission function and mean free path approximation.

$$I_{exp} \propto n \propto \frac{I}{\sigma \cdot T(E_{kin}) \cdot \lambda(E_{kin})} \simeq \frac{I \cdot \sqrt{E_{kin}}}{\sigma} \quad (2.5)$$

The quantitative Intensity as described in (2.5) is valid for the Omicron Analyzer as used for our experiment. When measuring at grazing take-off angles, one can improve the surface sensitivity of the measurement and therefore vital information about compositional homogeneity and surface chemistry of the sample can be gained. While 99% of the intensity comes from a region of the surface with thickness $3 \cdot \lambda$ at emission normal to the surface, this layer is reduced by $\cos(\theta)$ due to the longer way the electrons need to travel through the layer. (θ is the angle between sample normal and take-off angle) This fact is illustrated in Fig. 2.4 where the Si 2p core levels are shown in normal emission (NE) and grazing angle (GA) emission measurements. Therefore, by selecting a takeoff angle away from the sample normal, one can get some depth information about the sample. The same holds true for changing the kinetic energy: A higher kinetic energy leads to a deeper

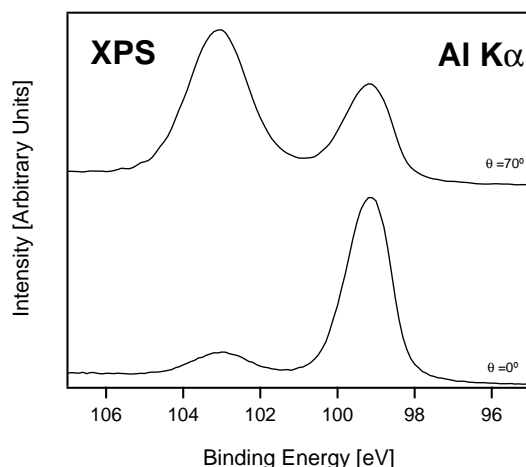


Figure 2.4: a) Si 2p core level spectra at normal emission take-off angle. The lower binding energy component is related to the signal of bulk Si while the higher binding energy component is related to the Si in the native oxide layer on the surface. b) Si 2p core level measured at 70° grazing angle. As the analysis depth is reduced by $\cos(\theta)$ the signal of the bulk is strongly attenuated while the signal of the oxide layer is amplified.

surface probing. All these facts are used in special occasions and prove very helpful for additional hints about sample homogeneity and surface composition within the analysis depth.

2.3.2 Ultraviolet Photoelectron Spectroscopy (UPS)

In UPS one uses primary radiation with a kinetic energy below 100 eV. This radiation can be produced by gas discharge lamps (HeI, HeII etc.) or from synchrotron sources. While XPS is mainly used to probe core levels and therefore composition and binding states at the surface, UPS is mainly used to probe the valence band and the electronic structure in reciprocal space [5]. If the sample orientation is altered with respect to the analyzer, one speaks of Angular Resolved Ultraviolet Photoelectron Spectroscopy (ARUPS). In these experiments, the kinetic energy E_{kin}^{vac} of an electron for a given polar angle θ_{ext} and the azimuthal angle ϕ_{ext} with respect to the surface normal is measured. This method is well established for the studies of single crystal samples and ordered overlayers. The polar angle θ defines the parallel momentum $k_{||}$ in the crystal azimuth ϕ . This is the basis for the band mapping capability of ARUPS. For more detailed information on this vast topic see [6]. The schematic setup is presented in Fig. 2.5. According to the three step model by Berglund and Spicer [7], the Photoemission process can be semi-empirically described by the following processes:

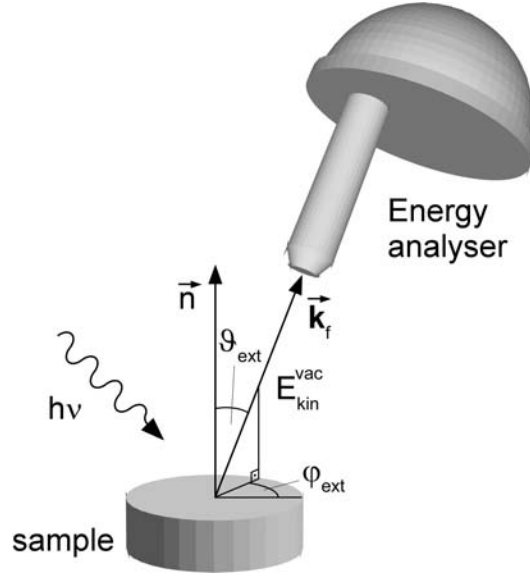


Figure 2.5: Schematic drawing of the source/analyzer/sample setup for angle resolved photoelectron spectroscopy. In this setup, the source and analyzer positions are fixed while the sample is scanned through the polar and azimuthal parameter space.

- The absorption of a photon and excitation of the photoelectron
- The travel of the photoelectron through the solid, including characteristic extrinsic losses
- The escape of the electron into vacuum towards an available final state

If one assumes free electron final states in the vacuum, the momentum of the photoelectron can be described as

$$E_f(\mathbf{k}_f) = \frac{\hbar^2 \mathbf{k}_f^2}{2m} \quad E_{kin}^{vac} = \frac{\hbar^2 \mathbf{k}_{vac}^2}{2m} \quad (2.6)$$

In this context, E_f and \mathbf{k}_f describe the final state in the solid while E_{kin}^{vac} and \mathbf{k}_{vac} describe the electron after escape of the solid to the vacuum. Emission of the electron to the vacuum is influenced by the so called inner potential V_0 , the energy step at the surface originating from the Coulomb and exchange interaction in the solid that create a mean attractive potential. Energy and momentum conservation at the surface can be expressed as:

$$E_f(\mathbf{k}_f) = E_i(\mathbf{k}_i) + h\nu \quad (2.7)$$

$$\mathbf{k}_f = \mathbf{k}_i + \mathbf{k}_{h\nu} + \mathbf{G} \quad (2.8)$$

While \mathbf{G} is a reciprocal lattice vector. At the photon energies below 50eV, the photon momentum can be neglected. Upon leaving the surface, the parallel momentum of the photoelectron is conserved, while the perpendicular component is affected by the inner potential:

$$k_{\parallel} = \frac{\sqrt{2m(h\nu - \Phi - E_b)}}{\hbar} \cdot \sin \vartheta_{ext} \quad (2.9)$$

This relationship directly relates the measured parameters ($E_b, \vartheta_{ext}, \varphi_{ext}$) to k_{\parallel} . In practice, one uses two modes of measurement to characterize the electronic properties of a surface:

- Constant energy maps: The parameter space ($\vartheta_{ext}, \varphi_{ext}$) is scanned at a fixed E_b . This allows for instance the mapping of the fermi energy of a surface.
- Band Dispersion: Spectras are recorded typically along high symmetry directions. For example, spectras are recorded at different angles ϑ_{ext} while holding φ_{ext} fixed to the value of interest. The recorded map can then be related to the dispersion of the respective features of the valence band in k-space .

2.3.3 X-Ray Photoelectron Diffraction (XPD)

Recording the sample intensity as a function of polar and azimuthal take-off angle when exciting the sample by X-Ray radiation, generally referred to as XPD, gives information about the local position and distribution of atoms in the vicinity of a photoelectron emitter. This method was introduced by Siegbahn et al. [8] and later explained by Fadley and Bergström [9] as an elastic scattering process. The situation is schematically depicted in Fig. 2.6. The spherical photoelectron wave is scattered by the neighboring atoms and interferes with the unscattered wave. The parameters dominating the interference are nearest-neighbor distance, atomic type of the scatterer and the relative phase of direct and scattered waves. For kinetic energies above 500eV, the so-called 'forward focussing effect' becomes dominant. This effect leads to a intensity maxima through a focussing of the scattered wave in the direction of nearest-neighbors. In metals, where in a typical XPD experiment the photoelectrons have a kinetic energy around 1keV, this effect usually allows for a very direct structure determination. In an experiment, the photoelectron intensity of a selected core level is collected as a function of polar and azimuthal emission angles over a solid angle of almost 2π . In our case, this is achieved by rotating the sample around the analyzer axis and recording the intensity of the selected core level. In Fig. 2.7, a measurement of the Ag(111) surface is presented. The intensity maxima at $\theta=35^\circ$ can be directly related to the fcc unit cell of Ag(111) as it reflects the angle between the (100) corner atoms and the (111) surface normal. This is underlined by a azimuthal cut through the intensity map along $\phi=0^\circ$. The scattering intensity can be simulated computationally using the underlying physics. In the simple case, only single scattering

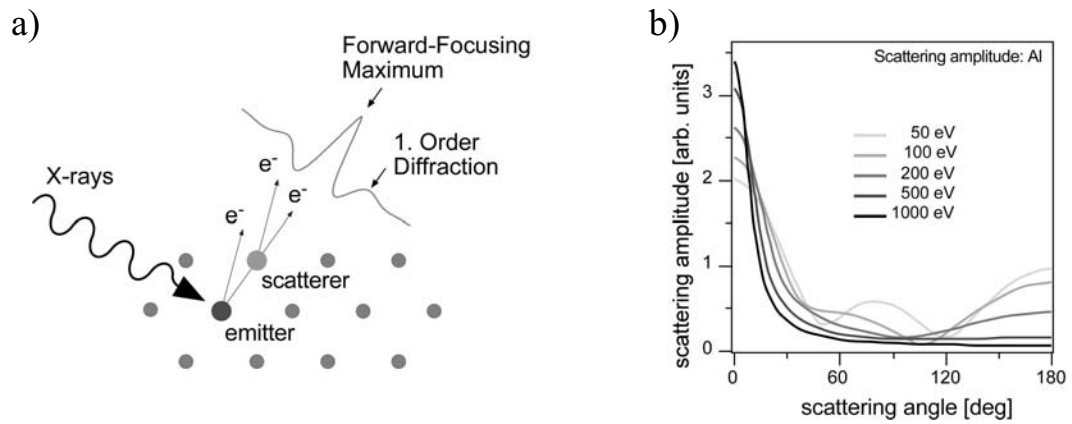


Figure 2.6: a) Schematic representation of the forward-focussing effect along atom chains and interference between scattered and unscattered waves. b) Scattering amplitude along a chain as a function of kinetic energy. It is clearly visible, that at high kinetic energy, electrons are mainly focussed in the direction of nearest neighbors of the emitter while at higher kinetic energy, substantial intensity are present also in other directions due to diffraction.

events are taken into account. In this case, one speaks of Single Scattering Cluster (SSC) calculations [10–12]. In general, this type of calculations reproduce the forward focussing directions quite well (see Fig. 2.7). One can immediately see that the forward focussing maxima are very well reproduced, although the fine structure lacks intensity. This is very often observed in metals because the fine structure is dominated by multiple scattering events. Nevertheless, SSC proves to be a very useful tool to pin down the local structure of a sample under investigation. In some cases, the maxima cannot be directly related to the nearest neighbor directions due to interference effects. Graphite is an example where the geometrical determined angles of expected forward-focussing maxima do not coincide with the detected intensity maxima. Corresponding illustrations of this effect with experimental and SSC data can be found in [13].

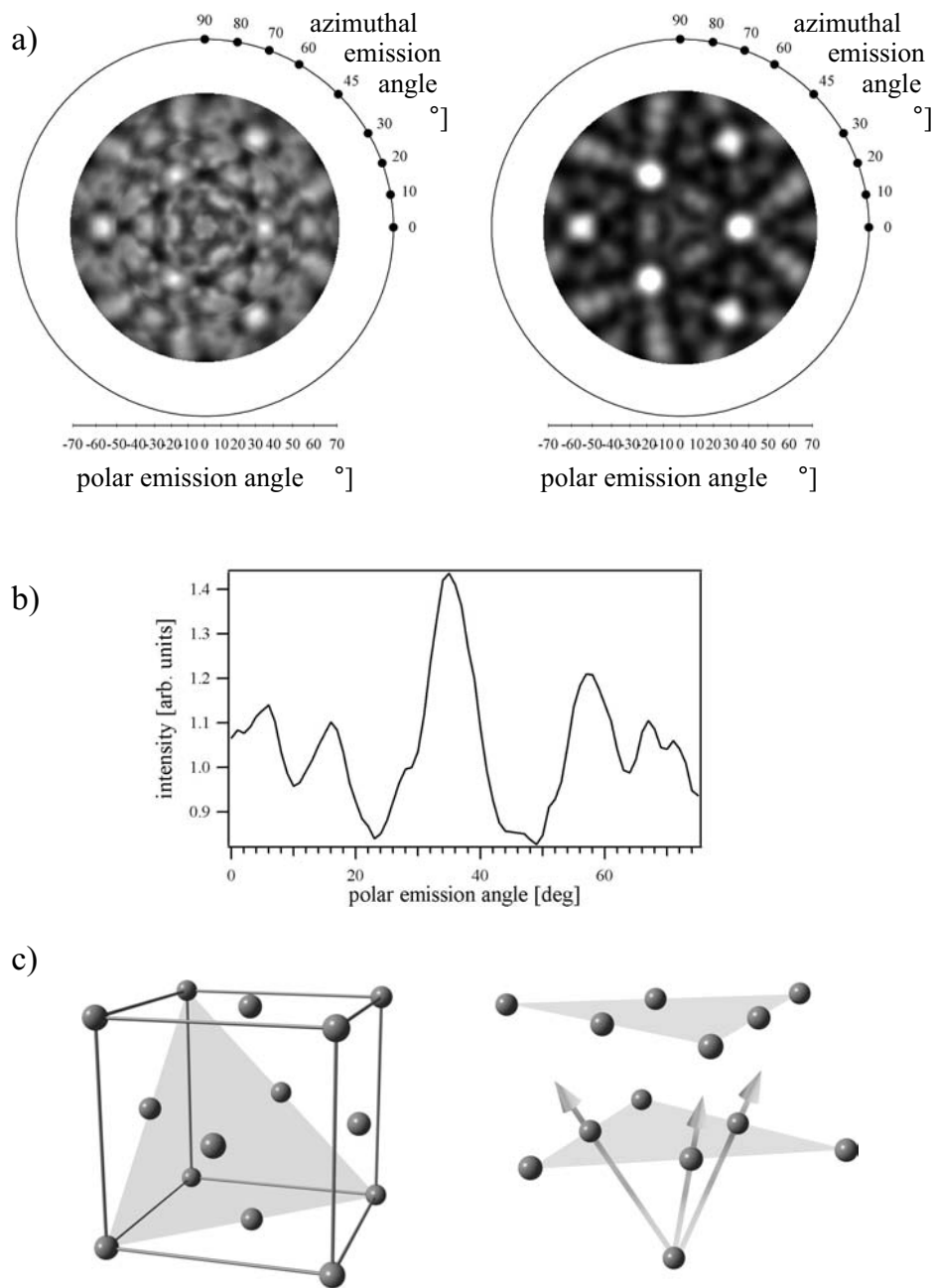


Figure 2.7: a) experimental XPD pattern of the Ag $3d_{5/2}$ core level measured with Mg $K\alpha$ radiation and corresponding SSC calculation. b) Polar cut along $\phi=0^\circ$. The forward focussing maxima can clearly be seen at 35° . c) fcc unit cell and illustration of nearest neighbor forward focussing direction by arrows. The gray shaded triangle depicts the (111) plane.

2.4 Low Energy Electron Diffraction (LEED)

Diffraction techniques are used for almost a century to assess the structure of crystalline samples. In surface science, Low Energy Electron Diffraction (LEED) is the technique

used most often to characterize the geometrical arrangement at the surface of single crystals. Upon the discovery of quasi crystals, the diffraction community was challenged to incorporate these aperiodic structures in theory as up to this point the periodicity - absent in quasi crystals - formed the underpinnings of the theory of diffraction. The classification of crystals has been extended to all systems forming a discrete diffraction pattern as it was realized that only long range positional order and not long range periodic order is necessary for diffraction. As LEED represents a fundamental analysis tool to the surface scientist, we briefly give an overview of LEED applied to periodic structures and a short description why diffraction patterns are observed in ordered but aperiodic structures like QC's. It is the aim of this section to give an overview of the method as far as it is necessary for the understanding of the presented work.

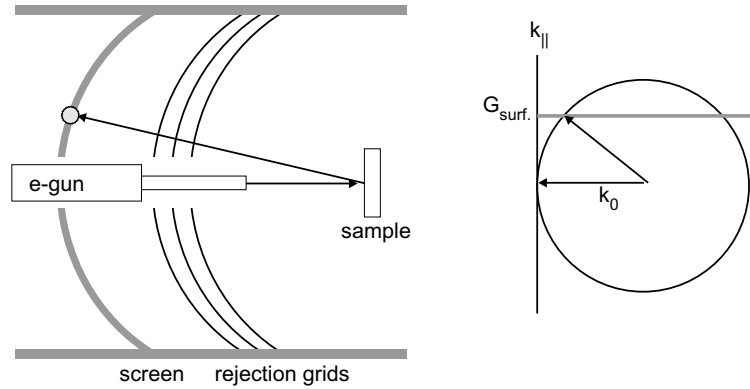


Figure 2.8: Schematic setup of a typical LEED experiment. A monoenergetic electron beam is produced by an electron gun through thermionic emission. The grid array acts as a high-pass filter, which rejects electrons subjected to inelastic scattering. These electrons are then accelerated towards the phosphor screen to produce the corresponding LEED pattern.

2.4.1 LEED from periodic crystals

In a typical LEED experiment, the sample is exposed to a narrow, monoenergetic electron beam. The electrons impinging on the surface are diffracted by interaction with the topmost layer of the surface and the produced pattern can be observed on a fluorescent screen after filtering out inelastically scattered electrons by means of a grid array. The schematic experimental setup is presented in Fig. 2.8

The measured scattering intensity for single scattering events without time dependent scattering density can be approximated as:

$$I(\mathbf{k} - \mathbf{k}_0) \propto \left| \int \rho(\mathbf{r}) e^{-i(\mathbf{k} - \mathbf{k}_0) \cdot \mathbf{r}} d\mathbf{r} \right|^2 \quad (2.10)$$

Where $\rho(\mathbf{r})$ is the complex scattering density of the material. For periodic structures, this scattering density can be expanded in a Fourier series, taking into account the translational symmetry of the material.

$$\rho(\mathbf{r}) = \sum_{\mathbf{G}} \rho_{\mathbf{G}} e^{i\mathbf{G}\cdot\mathbf{r}} \quad (2.11)$$

\mathbf{G} must fulfill conditions to preserve translational invariance of ρ with respect to the lattice. The set of \mathbf{G} -vectors spans the reciprocal lattice. Inserting 2.11 in 2.10, one has:

$$I(\mathbf{K}) \propto \left| \sum_{\mathbf{G}} \rho_{\mathbf{G}} \int e^{i(\mathbf{G}-\mathbf{K})\cdot\mathbf{r}} d\mathbf{r} \right|^2 \quad (2.12)$$

Where $\mathbf{K} = \mathbf{k} - \mathbf{k}_0$ is the scattering vector. Only appreciable intensity can be expected if the so called Laue Condition is fulfilled:

$$\mathbf{K} = \mathbf{G} \quad (2.13)$$

The Laue condition predicts that a diffraction intensity can only be observed if the scattering vector matches a reciprocal lattice vector \mathbf{G} . The Laue Condition can be pictorially described by the so called Ewald construction in Fig. 2.9. As a simple case, we consider a quadratic surface grid. The reciprocal lattice of this surface then comprises periodically spaced rods oriented to the surface normal. The so-called Ewald sphere intersecting those rods has a radius equal to the wavevector k given by the kinetic energy of the impinging electron beam. The intersection of the Ewald sphere with the rods gives the possible observable diffraction spots of the corresponding surface in real space. The magnitude of the wavevector can be varied by altering the kinetic energy of the electron beam and therefore, the intersections with the rods change - leading to a movement of the diffraction spots on the screen and eliminating/producing new diffraction spots. In a perfect 2D system, the intensity along the rods is constant. The 3D nature of the surface leads to intensity variations as different parts of the rods are probed. The analysis of the intensity variation along the rods (probed by varying the electron beam energy) is called I(V)-LEED and is solemnly mentioned for sake of completeness. One should refer to specific literature for additional information.

2.4.2 LEED from quasiperiodic crystals

The reciprocal space is related to the real space by a Fourier transformation. Why do aperiodic crystals offer very precise diffraction conditions? Referring to the Chapter *Introduction to Quasicrystals*, where the Fourier transformation of a 1D array is presented in Fig. 3.7 indeed show that the Fourier transformation of an aperiodic structure like

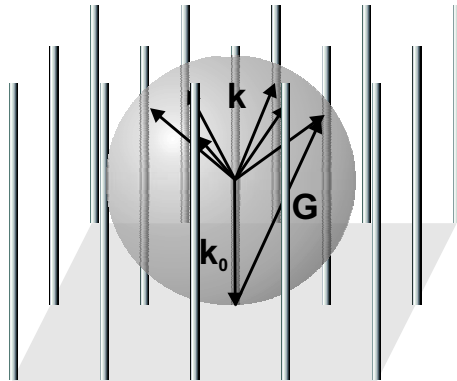


Figure 2.9: Ewald Sphere construction for a two-dimensional periodic lattice. The radius of the Ewald sphere is given by k_0 defined by the kinetic energy of the incident beam. All possible diffraction peaks are located at intersections of the rods with the sphere. The scattering direction is denoted as \mathbf{k} and $\mathbf{K} = \mathbf{k} - \mathbf{k}_0$ is a reciprocal lattice vector \mathbf{G} if scattering conditions are fulfilled.

Quasicrystals does offer very sharp peaks in k -space with an aperiodic relation. The presence of such densely packed sharp diffraction peaks have been described by a structure comprised of two or more mutually incommensurate lattices [14–16]. In this structure, a 1D quasicrystal is described as a sum of periodic functions with incommensurate periods. Both periodic functions alone would lead to a periodic LEED pattern with spacings k_1 and k_2 , while the sum of both produces the peaks for the individual periods plus linear combinations of k_1 and k_2 . In 3D, the reflexes are densely spaced in all three dimensions and do reflect the rotational symmetry of the underlying QC structure [14, 15].

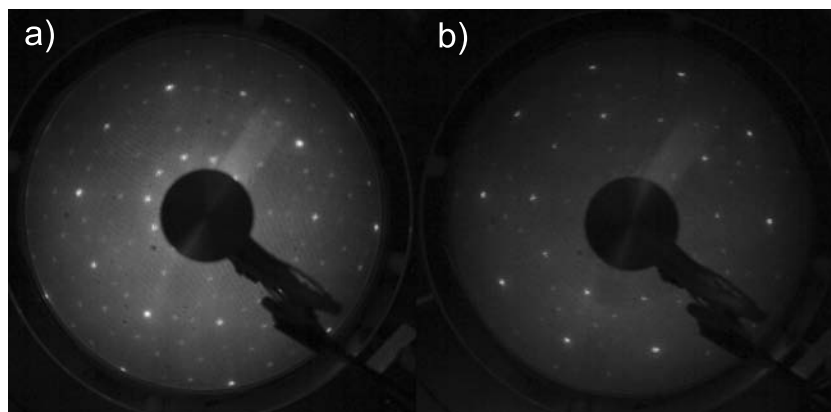


Figure 2.10: A typical LEED pattern of an AlPdMn single crystal with it's normal oriented along the fivefold axis. (a) is recorded at 45eV while (b)is recorded at 75eV kinetic energy.

2.5 Thin Film evaporation

The most common methods for single element deposition in UHV are sublimation and evaporation methods. For a comprehensive overview on the subject of vacuum thin film deposition, the reader might refer to books as for example the *Handbook of thin film technology* by Maissel and Glang [17]. Although commonly referred as a single process, the production of thin films by evaporation comprises three steps. The first step consists of the transition of the evaporand from the condensed phase into the gaseous phase. The condensed phase can either be solid or liquid, depending on material properties. This is followed by the vapor traversing the space between source and substrate and finally the condensation of the vapor upon arrival on the substrate. While the second step is of no concern as long as the background pressure of the chamber is sufficiently low, the transition of the condensed phase to the gaseous phase strongly defines the design of the source used. We will restrict ourselves to the sources which achieve the transition from the condensed to the vapor phase by thermal heating. While for some materials a purely resistive heating of the evaporand is sufficient to achieve a usable deposition rate on the substrate, for others such an approach is not accessible and crucibles must be used. The crucible can be heated either by resistive heating of a filament which heats the crucible either by thermal conduction and radiation or by bombarding the crucible by electrons. E-beam evaporation has clear advantages as it presents a much more versatile method, although at the price of being more complex in design. Both methods were used and will be shortly discussed in the later sections.

2.5.1 Vapor pressure

When a material is heated, the condensed matter is in equilibrium with its surroundings by building up a partial pressure in the vacuum. This partial pressure is generally referred to as the vapor pressure (VP) of a material at a given temperature. While the pressure at the boiling point is by definition the same for all materials, the VP at the melting point differ dramatically. For instance, Al has a VP of roughly 10^{-8} mbar at the melting point while the corresponding VP for Fe is 0.1 mbar. As a rule of thumb, a partial pressure of 10^{-2} mbar just over the liquid/vapor- or liquid/solid-interface is needed to achieve usable evaporation rates and therefore Al must be evaporated in the liquid phase while Fe can be evaporated by sublimation.

The desired VP therefore defines if a material can be evaporated directly as a rod or needs to be evaporated from a crucible as a molten element. The former does offer clear advantages, as it does guarantee the cleanliness of the element as contact of the hot material with other elements can generally be avoided. In the case of crucible evaporation, a detailed study of the phase diagram is necessary. The choice of the crucible material

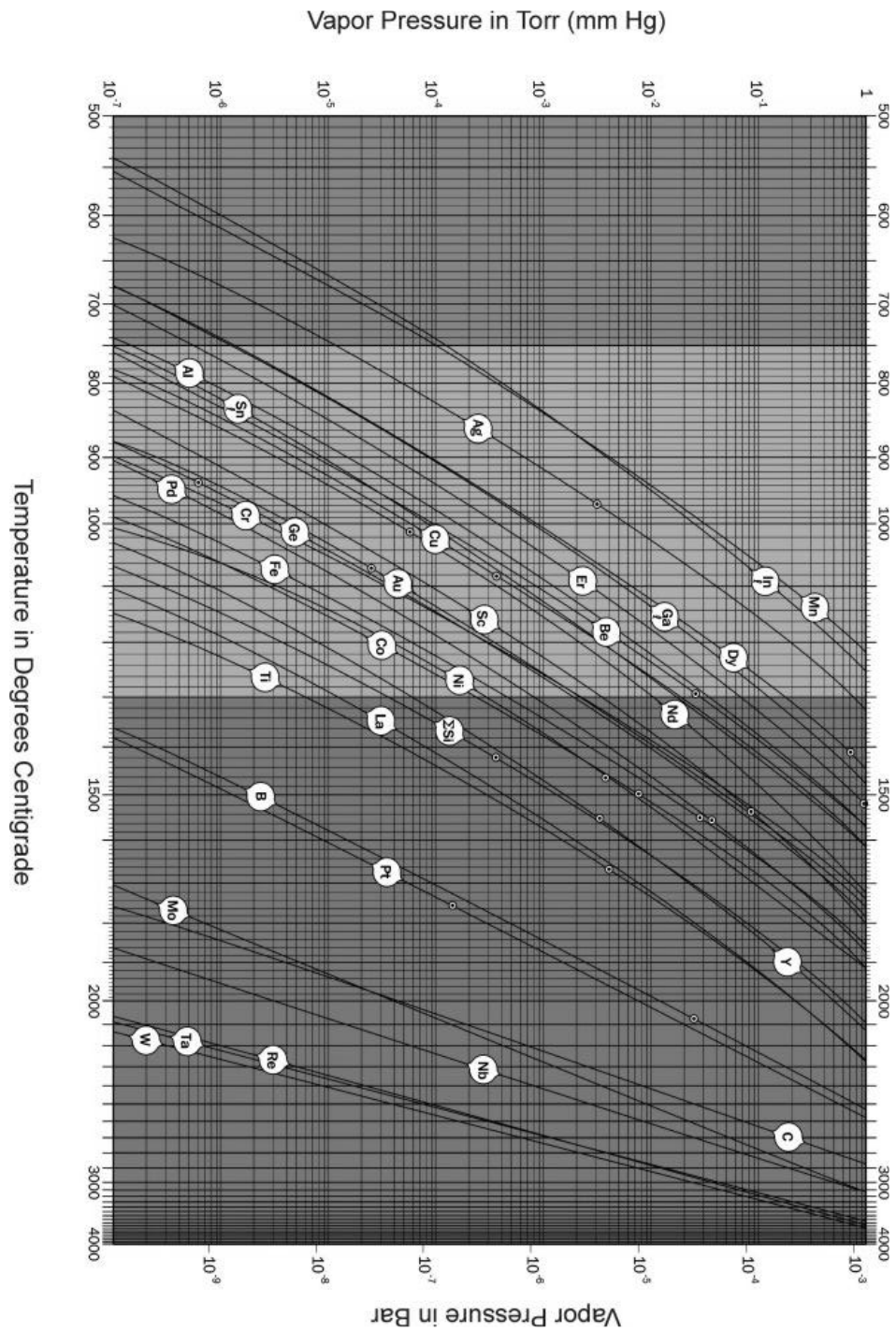


Figure 2.11: Vapor pressure of selected elements in bar vs. temperature in Celsius. The melting point of the respective element is marked by a black dot. Data taken from [18] A complete set of data can be found in [19]

is governed by the need for thermal stability, low outgassing and low reactivity with the evaporant material and low vapor pressure at the desired target temperature. Especially for e-beam evaporation, where conductive crucibles must be used, the materials of choice are quite often W, Mo, Ta or C. But some elements do react with those materials and indirectly heated oxide or nitride crucibles must be used. A detailed overview of crucible materials of choice for different materials can be found in [17].

2.5.2 Al cold lip evaporator

Among the metals of interest in this work, Al proves by far as the hardest for evaporation. The mayor problem with evaporating Al is the fact, that it must be heated to about 1200°C (therefore around 600°C over it's melting point) to achieve the needed partial pressure and evaporation rates. At this temperatures the molten Al tends to creep out the crucible material. To prevent this, one needs to rely on special evaporator designs - the so called COLD LIP designs. For our films, we use a COLD LIP Al Evaporator from Team 77 [20] which incorporates a 2ccm pBN crucible heated on the back and watercooled on the exit lip. By this design, a thermal gradient is created on the crucible itself. The Al on the bottom of the crucible is heated above 1000°C while the top of the crucible is cooled below the melting point for Al, efficiently preventing the Al from flowing out of the crucible. The crucible is heated by radiation from Ta filaments surrounding the crucible.

The flow can be controlled by regulating the heating power to a thermocouple in contact with the crucible, keeping the crucible temperature constant. The Al flow can be calibrated using a QCM at the sample position which can detect changes in resonant frequency as a function of deposited mass. The mass information can be gained by the so called Sauerbrey equation which directly relates shift in resonant frequency and deposited mass.

$$\Delta f = -\frac{1}{C_f} \Delta m \quad (2.14)$$

C_f is called the Sauerbrey constant and is independent of the film properties for rigid films.

2.5.3 E-Beam evaporation

E-Beam evaporation sources conceptually comprise a electron source which produce electrons by thermal heating of a filament. By using thoriated filaments, the filament temperature can be reduced to achieve a given electron emission due to the reduced work function. The emitted electrons are collected by either the evaporand material or a crucible containing the evaporand by applying a positive potential. The heating power is given by:

$$P[W] = I_{Emission}[A] \cdot U_{HV}[V] \quad (2.15)$$

For our works, we used a commercial e-beam evaporator of the type EFM3T from Omicron Nanotechnology GmbH. This evaporator gives the possibility to evaporate three materials simultaneously either from rods or from crucibles. A schematic cross section of the source is presented in Fig. 2.12. A feature of this source is the implemented ion current measurement devices. As can be seen from the cross sectional view, the filament is placed in front of the evaporand material. Therefore, the element vapor must travel through the current of impinging electrons and is partially ionized. Between the two collimation lenses, insulated cylinders detect the current produced by the impinging ions. This current is proportional to the flux leaving the source and can therefore act as flux control. Although the ion-current is generally not a quantitative tool as it depends on geometrical aspects (Filament - Crucible - Detector geometry), on elemental aspects (ionization cross section as a function of electron energy) and on process parameters (emission current and acceleration voltage) it is a handy tool to control the evaporation process when calibrated by quantitative methods (QCM) and the source is operated in constant parameter space. Therefore, for each element and geometry, the ion current can be used to control the real evaporand flux if one calibrates the source at a fixed emission current (fixed electron flux for ionization). In our experience, if one always uses the same emission current and the same ion flux by appropriately varying the high voltage, the real evaporand flux is reproducible by $\pm 5\%$, assuming fixed geometrical conditions. It is worthwhile to mention, that in some systems this setup might induce changes in film growth due to the presence of ions in the evaporant flux. Information about the subject can be found in [21]. This was particularly the case for the Cu films on the quasicrystal surfaces, which is the reason why we used a home made resistive Cu evaporator to deposit the Cu films on the QC.

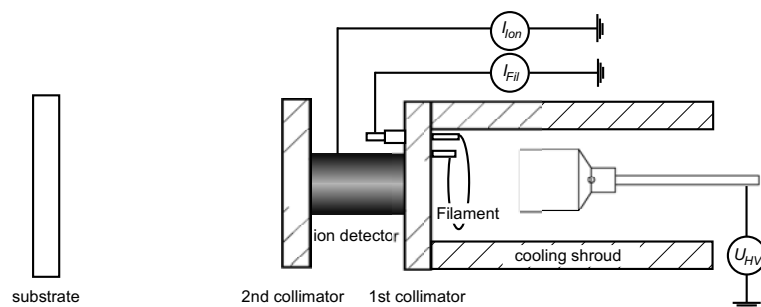


Figure 2.12: Simplified schematic drawing of a TriEFM E-Beam evaporator cell. Sample/evaporator distance not drawn to scale.

References for Chapter 2

- [1] A. Einstein, Noble Prize, "*For his services to Theoretical Physics, and especially for his discovery of the law of the photoelectric effect.*" (1921)
- [2] M.P. Seah, W.A. Dench, Surf. Int. Anal. **1**, 2 (1979)
- [3] K. Siegbahn et al., ESCA: Atomic, Molecular and Solid State Structure Studied by Means of Electron Spectroscopy, Almqvist and Wiksells, Uppsala (1967)
- [4] P. Ruffieux, P. Schwaller, O. Gröning, L. Schlapbach, P. Gröning, Q.C. Herd, D. Funnemann, J. Westermann, Rev. Sci. Instrum. **71**, 3635 (2000)
- [5] S. Hüfner, *Photoelectron Spectroscopy* (Springer Series in Solid State Sciences, **82**, Springer, 1995)
- [6] S.D. Kevan, *Studies in Surface Science and Catalysis Vol. 74: Angle-resolved photoemission*, (Elsevier, Amsterdam, 1992)
- [7] C. Berglund, W.E. Spicer, Phys. Rev. A **136**, 1030 (1964)
- [8] K. Siegbahn, U. Gelius, H. Siegbahn and E. Oslon, Phys. Lett. **32a**, 221 (1970)
- [9] C.S. Fadley and S.Å.L Bergström, Phys. Rev. Lett. **5**, 375 (1971)
- [10] J. Osterwalder, T. Greber, A. Stuck and L.Schlapbach, Phys. Rev. B **44**, 13764 (1993)
- [11] R. Fasel, PhD thesis Nr. 1118, University of Fribourg (1996)
- [12] C.S. Fadley, in *Synchrotron Radiation Reserach: Advances in Surface Science*, R.Z. Bachrach (Edt.), (Plenum, New York, 1989)
- [13] P. Ruffieux, PhD thesis Nr. 1387, University of Fribourg (2002)
- [14] D. Levine, P.J. Steinhardt, Phys. Rev. Lett. **53**, 2477 (1984)
- [15] D. Levine, P.J. Steinhardt, Phys. Rev. B. **34**, 596 (1986)

- [16] C. Janot, *Quasicrystals: A Primer*, (Oxford, Clarendon, 1992)
- [17] L.I. Maissel, R. Glang, *Handbook of Thin Film Technology*, (McGraw-Hill Book Company, New York, 1983)
- [18] www.veeco.com/learning/
- [19] R.E. Honing, RCA Rev., **23**567 (1962)
- [20] Team 77, Einrichtungen Wetzell GmbH, Schimmelbuschstr. 23, 40699 Erkrath(Hochdahl), Germany
- [21] J. Kirschner, H. Engelhard, D. Hartung, Rev. Sci. Instr. **73**, 3853 (2002)

Chapter 3

Introduction Quasicrystals

This chapter is dedicated to quasicrystals (QC) and is intended to introduce some basic features and properties of quasicrystals as well as its terminology. As these materials are special in every aspect, it deserves some special attention. Basic concepts of the structure are addressed to point out the difference to classical crystals with translational symmetry. It treats some aspects of quasicrystals related to surface science. Photoelectron Spectroscopy reference data are presented as a guideline for the scientific chapters of this thesis. The presentation of physical properties are kept at a necessary minimum to motivate the interest of QC's with respect to tribological applications and give an impression on why they are of fundamental interest. We aim at giving the reader not familiar with the topic the necessary 'tools' to better understand the contents of the works presented thereafter.

"A certain man put a pair of rabbits in a place surrounded on all sides by a wall. How many pairs of rabbits can be produced from that pair in a year if it is supposed that every month each pair begets a new pair which from the second month on becomes productive?"

Liber abaci, Leonardo Pisano (Fibonacci), 1202a.c.

3.1 History

The first publication about quasicrystals by Schechtman et al. [1] and followed by Levine et al. [2] caused a major turmoil in material science. They showed a diffraction pattern of the icosahedral point symmetry group which simply fell out of the boundaries of the current classification schemes of what constitutes a crystal. This publication was titled as "Metallic Phase with Long-Range Orientational Order and No Translational Symmetry" and is currently under the top ten cited papers in PRL. They discovered an icosahedral symmetry in the X-ray diffraction pattern of an Al-Mn alloy. Later on, it was confirmed that this structure effectively was due to an independent solid state phase.

3.2 What is different to classical crystals?

To understand the differences of QC's compared to classical crystals, it is important to recall the basic concepts of classical crystals as well as those for QC's. The consequences arising from this descriptions and the limitations coming with it will be described thereafter.

3.2.1 Theoretical description of classical crystals

Classical crystals are theoretically described by means of a unit cell and a set of 3 unique basis vectors. The macroscopical material can then be theoretically assessed by repeating this unit cell at every linear combination of those basis vectors. This concept is referred to as *translational symmetry*. This concept is a fundamental property that lies on the basis of many aspects of theoretical description of classical crystals. It is implemented by using periodic boundary conditions or by abbreviating the local coordinate by a linear combination of the basic translational vectors. Further, they lead us ultimately to the theoretical description of vibrational properties (phonos, thermal properties), electronic properties (Density of states, band structure, free electron model) and diffraction (identification through R-factor analysis of diffraction spectra) to name a few.

3.2.2 Theoretical description of quasicrystals

Upon their discovery, QC's did not fit the description of crystals. They consist of so called "forbidden" 5-, 8-, 10-, or 12-fold rotational symmetry. No translational symmetry can persist in such structures as no space filling arrangement can be created. Actually, theoretical descriptions follow two approaches. The Tiling/Pseudo Unit Cell approach describes QC's in an analogue picture to the Translation/Unit Cell picture of classical crystals. The translation is replaced by a tiling grid, which is build following so-called

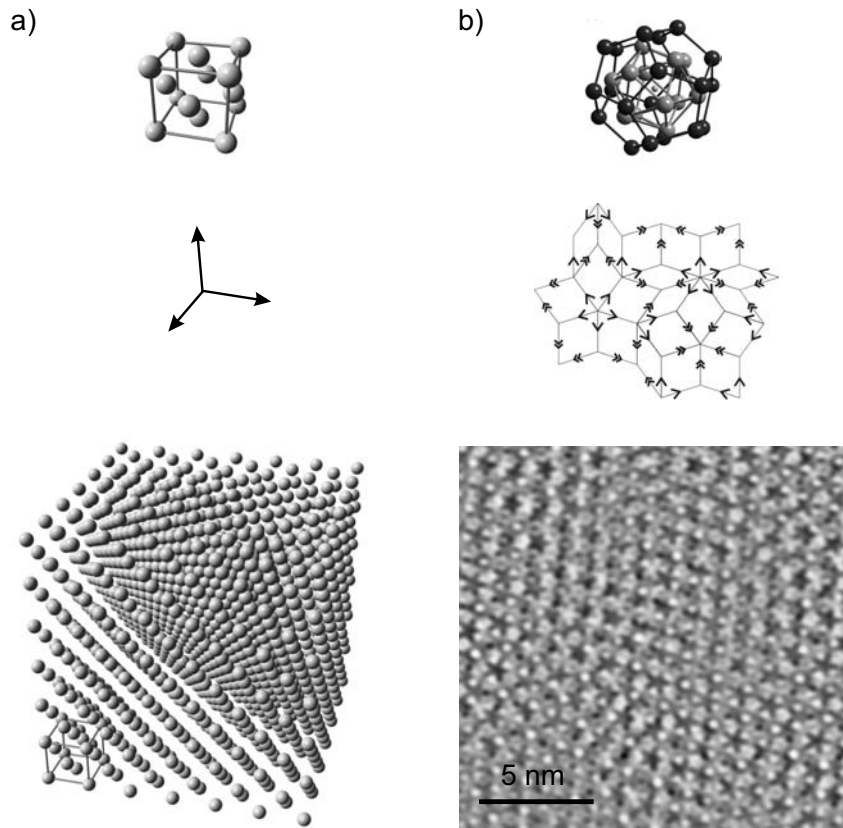


Figure 3.1: (a) Unit cell of a fcc crystal. Together with the set of basic translational vectors, one can create the macroscopical crystal structure. (b) B-cluster are proposed as the so-called quasi unit cell. The individual clusters might share atoms with neighboring clusters. The concept of translation vectors is replaced by the tiling/matching rules. These rules are not strict and are violated at times (phason flip). On the bottom we show a STM measurement with atomic resolution on the terraced, bulk termination of i-AlPdMn 5f. The stars were identified as dissected B-clusters [3].

matching rules. The tiling serves as a grid where the pseudo-unit cells are placed. In contrast to classical crystals, the pseudo-unit cells overlap and share atoms. The second approach describes the QC's identical to classical crystals - only in higher dimensional space. The real structure is a manifestation of this higher dimensional description by projecting it to the lower dimensional 3D space. This concept is usually referred to as *Embedding*, as the 3D real world structure is embedded in a theoretical, higher dimensional frame work. Most theories can be extended to higher dimension and then be suitably applied. The current limitation is the extension of the experimental information to create the higher dimensional model - as the observable structure only represents a sub-ensemble and therefore different higher dimensional models might yield the same 3D structure. The

solution of the atomic structure is a field of intense research. For this purpose, the so-called *approximants* are of prime importance. Approximants are periodic crystals, usually with large unit cells, which are close in composition to the respective QC's and offer strong local similarity to the QC's. The strong structural similarity combined with periodicity offers a means of approximating the QC structure with the mathematical simplicity of translational symmetry - hence the name approximant.

3.3 Tilings

Tilings are the conceptual equivalent to the grid in periodic crystals, although their construction is more complex and defined by so called matching rules which are less rigidly defined. These matching rules govern local configurations which might appear in a tiling and might be regarded as schematically representing the energetics of some atomic decoration of the tiles. Consequently, they impose constraints on the global structure. The study of matching rules provides insight about the plausibility of models based on such tiles where the atomic positions are believed to be determined by short-range interactions only. Their existence lends support to the idea that these local interactions may be sufficient for the physical realization of QC's. This statement is underlined by the fact that QC-phases can be found on rapidly quenched intermetallic alloys.

3.3.1 Penrose Tilings

The mathematical and aesthetical aspects of quasiperiodic tilings attracted attention well before the discovery of QC's [6]. Bruijn has developed important techniques for the construction and analysis of Penrose tilings [7]. Although Penrose tilings are originally 2D tilings, the extension to 3D is for most part straightforward. There exist different tiling models reflecting the rotational symmetries different from decagonal as well as higher dimensional symmetries. For more complete references on this subject one should refer to general text books like [4, 5]. The mathematical techniques have since been extended to other tilings, for instance its icosahedral 3D analogue [4, 8, 9]. One version of the Penrose Tiling is an N=5 rhombic tiling, composed from two shapes of tile conventionally labelled as "skinny" and "fat" as depicted in Fig. 3.2 [6]. The corresponding matching rules for the rhombic Penrose pattern were formally expressed by Bruijn in 1981 [7]. Those Matching rules are as follows:

1. Each edge of any Penrose tiling can be marked by a single or double arrowhead so that each fat and skinny tile is marked exactly the same way (Fig. 3.2).
2. There exist only 8 distinct configurations of arrow-marked tiles surrounding a common vertex (Fig. 3.3).

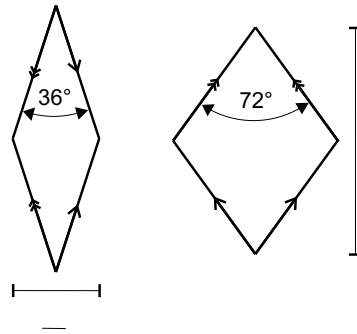


Figure 3.2: Basic rhombi of the Penrose tiling. The basic rhombi are referred to as 'skinny' and 'fat'. While the width of the skinny rhombus is related by $\frac{1}{\tau}$ to its side length, the height of the fat rhombus is τ . (τ =golden ratio)

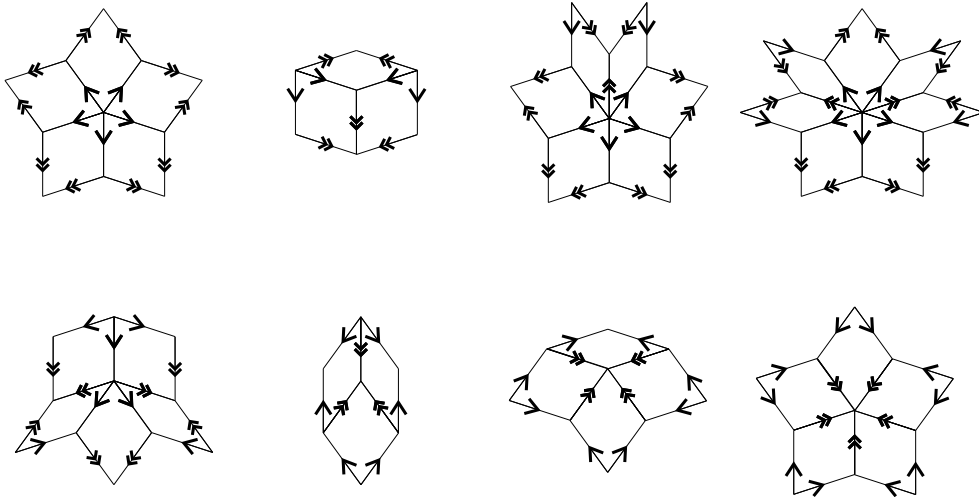


Figure 3.3: The eight allowed vertex configurations with edge-arrow decoration of the tiles.

Although those rules greatly restrict the possible configuration of the basic building blocks, there exist additional constraints. Practically, one starts with a sufficiently large seed cluster ('Large' in this context will be more precisely defined later). The further growth then starts with the random selection of an edge on the surface of the cluster. This respective site can then be classified as follows:

1. Forced Site: The site only allows the placement of one oriented, arrowed skinny respectively fat tile to produce a vertex configuration in agreement with the 8 basic vertex decorations.

2. **Unforced Site:** The addition of an oriented, arrowed skinny or fat tile produces an equally allowed vertex configuration as described by the 8 basic vertex decorations.
3. **Marginal Site:** There exist unforced sites, where - although consistent with the local environment - the addition of a skinny tile is discarded. Figure 3.4 presents the only 3 types of marginal edges. Mark that these marginal edges can become unforced or forced after addition of a new tile.

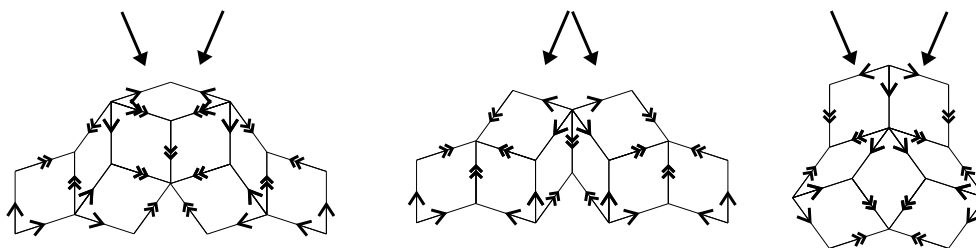


Figure 3.4: Marginal vertex configurations. The edges marked by arrows are considered marginal and are excluded for decoration with a skinny tile.

If a forced edge is selected, the uniquely allowed tile is added with probability $p = 1$. If an unforced edge is selected, nothing is added until it becomes forced. If a marginal edge is selected, a fat tile is added with probability $p < 1$. When a surface offers no forced edges, the surface is called 'dead'. When a dead surface is reached, a fat tile is added to a marginal site. This creates new forced sites where growth can continue rapidly. It can be shown that the addition of a tile to a forced edge never introduces a defect in the tile and that every dead surface contains at least one marginal site [4]. A large enough seed cluster is one containing at least one forced or marginal site.

The matching rules can be violated at times. One prominent example is the so called phason flip, an additional degree of freedom in quasicrystals. The phason flip manifests itself as a local reordering of the tiling, ultimately leading to a violation of the rules. Phasons are more easily understood in higher dimensional space and one is referred to the section 3.4 on Embedding. Figure 3.5 depicts a phason flip in 2D of a Penrose Tile.

3.3.2 Cluster model - the quasi unit-cell

While tiling models can explain some characteristics of Quasicrystals, their connection to physical reality is not straight forward to justify. Especially, the tiling picture should not be confused with the physical position of atoms. The Penrose tiling presented in the section above presents one of the simplest cases with respect to matching rules. In general, the matching rules can not be defined so locally. Matching rules are usually a list

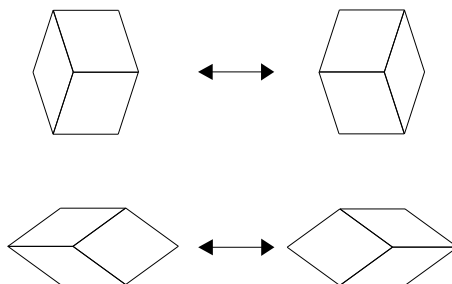


Figure 3.5: A phason flip of a Penrose tile consist of the exchange of the basic rombi. By this movement, no new tiles are created. But the phason flip leads to a local violation of the matching rules.

of allowed and forbidden tile configurations up to a certain radius. Therefore, the physical grounds underlying these matching rules cannot be justified by simple short-range atomic interactions. Why are QC's stable? The tilings do not include energetic arguments in a straight physical way. It comes down to the question what the basic building blocks of QC's are: The equivalent to the unit cell: *The quasi unit-cell*

If one looks at a STM picture (Fig. 3.1) of a QC, the eye catches simple motifs which are omnipresent on the surface. These motifs are sometimes complete, sometimes they *overlap* other motifs. This is most prominent on decagonal QC's oriented along the periodic axis. Those clusters have a size of some nm and govern the whole structure. Obviously, clusters represent an energetically favorable atomic configuration. The structure tries to minimize the energy by building as much clusters as possible. Therefore, in a cluster model, the tilings are decorated by clusters. In contrast to the picture grid/unit cell of classical crystals, the clusters are allowed to overlap to maximize the cluster density. In the region of overlap, the atomic structure must be equivalent - both clusters share those atoms. This sharing of atoms restricts the possibilities and forms the inherent connection to the matching rules. B- and M-clusters do play a great importance in the icosahedral AlPdMn QC alloy. The B-cluster consists of an icosahedron surrounded by a dodecahedron and is presented in Fig. 3.6 along with the M-cluster. Both clusters can be considered as a basic building block of a QC, although the atomic configuration is not necessarily identical in the clusters as it is the case in a normal unit cell.

3.4 Embedding

3.4.1 The Fibonacci sequence

In 1202, Leonardo Pisano, better known for his nickname Fibonacci, published a book called *Liber abaci*. The book was based on the arithmetic and algebra that Fibonacci

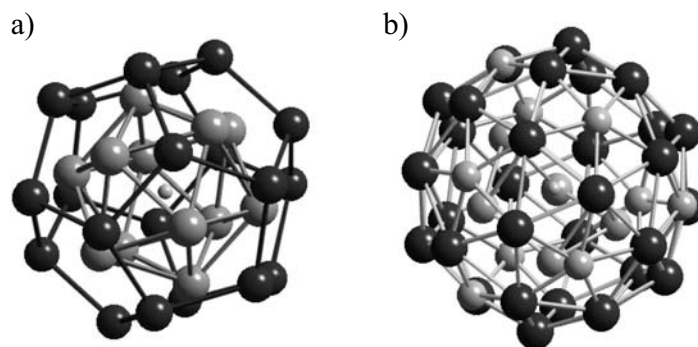


Figure 3.6: (a) B-cluster (similar to Bergman clusters) consisting of 33 atoms are the basic units of *i*-AlPdMn and *i*-AlCuFe structures (b) M-cluster (similar to Mackay clusters) consisting of 50 atoms can be seen as complement to the Bergman clusters [10]

accumulated during his travels. One of the chapters of the book is devoted to the Fibonacci sequence for which he is best remembered today: *"A certain man put a pair of rabbits in a place surrounded on all sides by a wall. How many pairs of rabbits can be produced from that pair in a year if it is supposed that every month each pair begets a new pair which from the second month on becomes productive?"* The resulting sequence is 1, 2, 3, 5, 8, 13, 21, 34, and so forth. This sequence has proven to be extremely fruitful in different areas of mathematics and science. One of the particularities of the sequence is, that the ratio of two consecutive numbers approximates asymptotically the golden ratio as the sequence evolves:

$$\tau = \frac{1 + \sqrt{5}}{2} \quad (3.1)$$

The golden ratio $\tau=1.61803\dots$ is irrational and plays an important role in the framework of quasicrystals. It is also important to notice, that $\cos(36^\circ) = \frac{\tau}{2}$ which further underlines the connection to 5- and 10-fold structures.

3.4.2 Extension to n-Dim

A textbook example for a quasicrystal analogue in one-dimensional space (1D) is the Fibonacci chain, which consists of two segments of different lengths (L-long and S-short). Their ratio L/S is $\tau=1.61803\dots$. The Fibonacci chain can be constructed alternatively to the above sequence, based on L and S as building blocks. Each new iteration is created by replacing S by L and L by LS. The generated sequence is therefore as follows:

S
 L
 LS
 LSL
 LSLLS
 LSLLSLSL
 LSLLSLSLLSLLS
 LSLLSLSLLSLLSLSLLSLSL
 LSLLSLSLLSLLSLSLLSLSLLSLSLLSLSL

Let's consider a 1D sequence of dirac functions with x-axis spacing corresponding to the Fibonacci sequence (two distances corresponding to L and S with a ratio of τ) The corresponding pattern is aperiodic by definition. The FFT pattern of such a function is a series of sharp peaks at correlated distances as depicted in Fig. 3.7. Although, the number of peaks is infinite, only a few present appreciable intensity. The intensity is symmetric around the origin and the spacing of the peaks is aperiodic, fulfilling a τ relationship. This approach has been used by Gierer et al. [11] to explain the SPA-LEED patterns of d-AlNiCo. How is now the Fibonacci chain - the model case of a QC in 1D - related to a

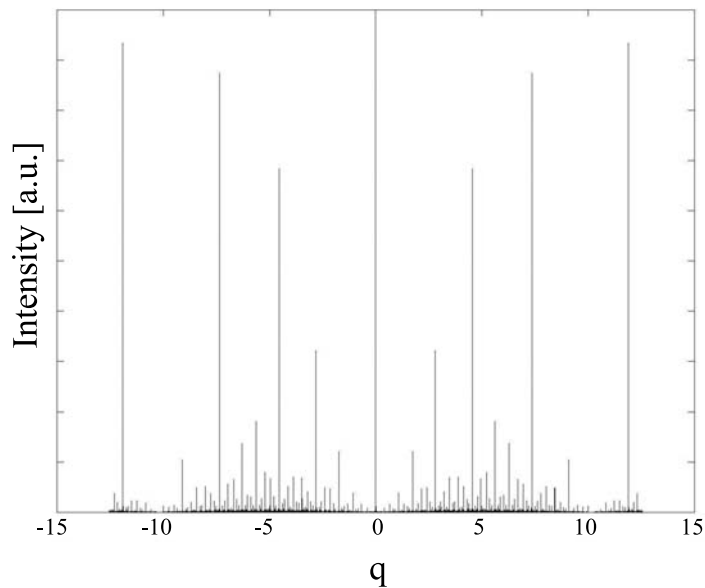


Figure 3.7: Fourier Transformation of a 10'000 component Fibonacci sequence. Only few peaks exist with appreciable intensity and their position is aperiodic. The scale of q is set by the short segment S of the Fibonacci chain, in this case $q=1$. It corresponds to $q = \frac{1}{S}$ [12]

2D periodic system? Let's consider a 2D periodic grid as presented in Fig. 3.8. Cutting through the grid with the condition of an irrational slope with respect to the grid, the line is split in 2 unit lengths by the projection of the 2D grid. The gray area denotes the

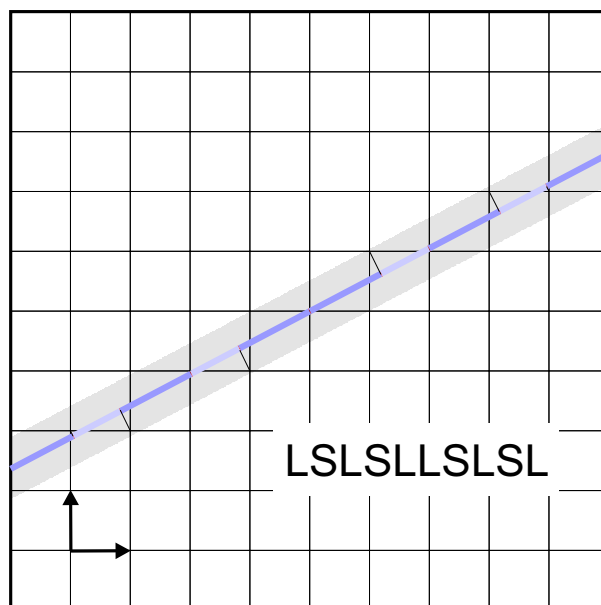


Figure 3.8: Projection of a 2D grid by a projection window (gray zone) in 1D creates an aperiodic sequence of line segments following a Fibonacci sequence, if the angle of the line is irrational. The line is cut in short (S) and long (L) line segments which exhibit no periodic order, although the underlying system is perfectly ordered in a higher dimensional space.

projection window given by the base vector of the unit cell. The two units can be denoted as a short (S) and a long (L) line segment. The sequence of S and L segments is completely aperiodic and is a segment of the Fibonacci chain if the angle of the projection line is chosen irrational. The 1D Fibonacci sequence of line segments can therefore be *embedded* in the 2D space to be represented as a translational symmetric system describable by the rules governing such systems. The same concept can be extended to higher dimensional quasiperiodic analogues. While aperiodic in 3D space, one can show that QC's can be described by using a periodic approach in $6D-n$ ($0 \leq n \leq 2$) dimensional space and the real structure is a suitable projection of the higher dimensional space in 3D. Therefore, the concepts in crystallography remain applicable in principle if one treats QC's in a higher dimensional framework.

3.4.3 Phasons

Quasicrystals have an additional degree of freedom compared to classical crystals. This is a consequence due to the embedding in a higher dimensional space and does not exist in classical crystals. If one slightly shifts the projection window in Fig. 3.8, some spots will enter the projection zone while exactly the same number leave it. This leads to a local reordering of the vertices, i.e. local replacement of S and L segments of the

sequence. The resulting movement of vertices is called *Phason Flip*. Energetically, these configurations are very close as only a small displacement of the projection window gives us this new configurations. While in the higher dimensional space (here 2D), the phason flip is a continuous process, in real space (1D) it appears as a discrete transition. The same arguments hold true for decagonal (2D) and icosahedral (3D) quasicrystals and the extension is straight forward.

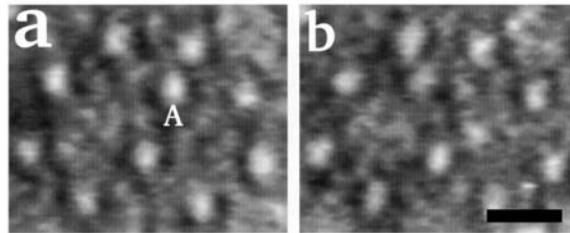


Figure 3.9: Phason flip observed by HRTEM on decagonal Al-Cu-Co at 1123K. The scaling bar corresponds to 2nm. The timescale for the observed flip is 5sec. Data taken from [13].

3.5 Classification of QC Systems

There are different types of quasicrystal systems. One can classify them with respect to structure or composition. By far not all quasicrystal systems do form thermodynamically stable phases. Quasicrystal systems can be produced by quenching of melts as a metastable phase. But today, many stable QC systems are known, although the metastable phase is more abundant.

3.5.1 Classification by structure

- Quasiperiodic in 2D (Periodic \perp to the quasiperiodic layers)
 - octagonal quasicrystals with local 8-fold symmetry
 - decagonal quasicrystals with local 10-fold symmetry
 - dodecagonal quasicrystals with local 12-fold symmetry

- **Quasiperiodic in 3D** (No periodic direction)
 - icosahedral quasicrystals (axes:12x5-fold, 20x3-fold, 30x2-fold)

3.5.2 Classification by composition (selection)

octagonal	decagonal	dodecagonal	icosahedral
V-Ni-Si	Al-TM ₁	Cr-Ni	Al-Mn
Cr-Ni-Si	Al-Ni-Co *	V-Ni	Al-Mn-Si
Mn-Si	Al-Cu-Mn	V-Ni-Si	Al-Li-Cu *
Mn-Fe-Si	Al-Cu-Fe		Al-Pd-Mn *
	Al-Cu-Fe		Al-Cu-Fe
	Al-Cu-Ni		Al-Cu-Fe
	Al-Cu-Co *		Al-Mg-Zn
	Al-Cu-Co-Si *		Zn-Mg-RE
	Al-Pd-Mn *		Ti-TM ₂
	V-Ni-Si		V-Ni-Si
	Cr-Ni		Pd-U-Si

Table 3.1: Selection of systems forming quasicrystal phases.

TM₁=Ir,Pd,Pt,Os,Ru,Rh,Mn,Fe,Co,Ni,Cr

RE=La,Ce,Nd,Sm,Gd,Dy,Ho,Y

TM₂=Fe,Mn,Co,Ni

* stable phases exist. Data from [14].

3.6 Physical Properties

A great deal of the attraction of QC's comes from the fact, that although intermetallic alloys of metals, their properties differ significantly from the parental elements. It is these unusual properties that makes them thrilling from a fundamental point of view as well as interesting from an application related perspective. In Table 3.2 a selected number of physical properties of AlPdMn and AlCuFe are compared to values for benchmark materials. AlPdMn is readily available in large single grain high quality samples and AlCuFe is interesting for application due to it's inexpensive components. Quasicrystals behave mechanically rather like ceramics: They are brittle (low fracture toughness) and hard materials (high Vickers Hardness). The low coefficient of friction together with the high hardness makes them interesting for low friction/low wear coatings, although no commercial product has reached the market place yet. Quasicrystals exhibit a rather low surface energy. It is much lower than the value for clean metals and lower than the value

for alumina and does compare rather favorably to Teflon. It has been speculated, that this is connected to the low coefficient of friction and oxidation resistance of quasicrystals. [15, 16] Surprisingly, high quality quasicrystals are very poor electrical conductors: They are even worse than the amorphous counterparts. Also, they show a very low thermal conductivity. This can be connected to the high localization of the electrons and the absence of translational symmetry.

property	value	material
hardness (H_v)	6000-10000	diamond [17]
	750-1200	silica [17, 18]
	800-1000	i-Al-Cu-Fe [15, 19]
	700-800	i-Al-Pd-Mn [20]
	70-200	low carbon steel [17, 18]
	40-105	copper [17, 18]
	25-45	aluminium [17, 18]
coefficient of friction (unlubricated vs diamond pin)	0.42	copper [21]
	0.37	aluminium alloy [21]
	0.32	low-carbon steel [21]
	0.05-0.2	i-Al-Cu-Fe [21, 22]
fracture toughness [MPa m ^{1/2}]	4	alumina [23]
	1.5	silica [24]
	1	i-Al-Cu-Fe [15, 19]
	0.3	i-Al-Pd-Mn [20]
Young's modulus 10 ⁶ psi	31	stainless steel [25]
	29	i-Al-Pd-Mn [20]
	19	copper [25]
	10	Aluminium [25]
	9	i-Al-Cu-Fe [15]
thermal conductivity [W m ⁻¹ K ⁻¹]	390	copper [25]
	170	aluminium [15]
	50	low-carbon steel [25]
	2	i-Al-Cu-Fe [15]
surface energy [mJ/m ²]	2480	iron(clean) [26]
	1830	copper (clean) [26]
	50	alumina [22]
	24-25	i-Al-Pd-Mn (air-oxidized) [22]
	17-18	PTFE (Teflon) [22]

Table 3.2: Selected Values of Physical and Mechanical Properties of Icosahedral Alloys, compared with relevant benchmark Materials at room temperature. Table compiled by [27].

3.7 Photoemission from QC's : AlPdMn

3.7.1 X-ray Photoelectron Spectroscopy

XPS spectra of the pure elements and the QC are presented in Fig. 3.10. Furthermore, all surfaces were subjected to oxidation experiments. Characteristic for the QC phase in XPS is a peak shift of the Pd 3d level to higher binding energies and a change in peak shape of the Mn 2p level. Oxidation of the QC leads to an oxide component only in Al. The passivating characteristics of the QC are a consequence of the Al-rich termination of QC's [28, 29] and the formation of an Al-oxide layer upon oxidation. The peak shift in Pd is not unique to the QC phase: Also AlPd shows a peak shift of 1.8eV to higher Binding energies [30]. Therefore, only this feature cannot be taken as a fingerprint for QC-phase formation.

System	Core Level	E_B [eV]
Bulk Al	Al 2s	117.4
Bulk Pd	Pd 3d _{5/2}	334.8
Bulk Mn	Mn 2p _{3/2}	638.2
i-AlPdMn	Al 2s	117.4
i-AlPdMn	Pd 3d _{5/2}	336.5
i-AlPdMn	Mn 2p _{3/2}	638.1

Table 3.3: XPS Reference Data for bulk Al, Pd and Mn and of an i-Al₇₀Pd₂₀Mn₁₀ QC after standard surface preparation.

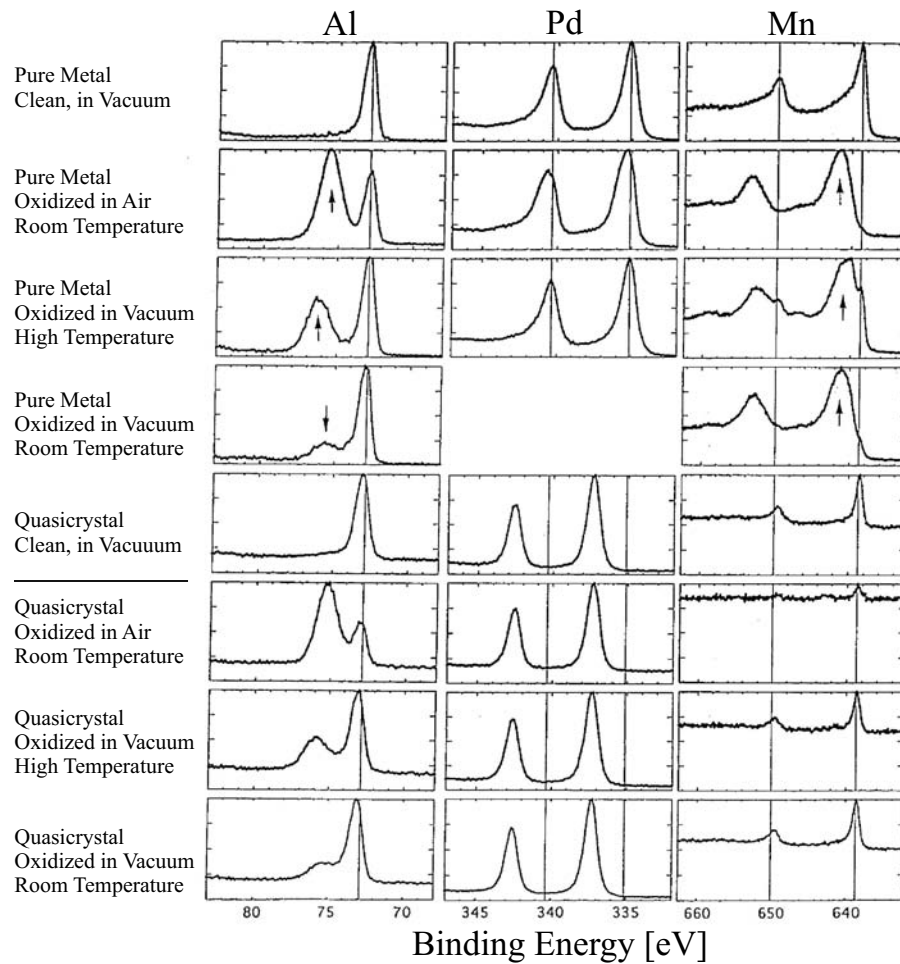


Figure 3.10: XPS Data for the Pd 3d, Al 2p and Mn 2p core levels of the individual elements and in the i-QC phase as clean surfaces and subjected to different oxidations. A characteristic feature of the QC phase is a peak shift of the Pd 3d level to higher binding energies and a change in the peak shape of the Mn 2p levels. The Pd does not oxidize, neither in the pure metal nor in the QC. Al and Mn do oxidize as pure elements under all oxidizing conditions while in the QC, only the Al oxidized and builds up a passivating Al-oxide layer. This is the basis for the passivation behavior of the QC. Data taken from [31]

3.7.2 Ultraviolet Photoemission Spectroscopy

UPS Valenceband spectra are presented in Fig. 3.11. Three valenceband spectra of 5f i-AlPdMn surface terminations are compared to each other. The cubic termination of a sputtered and unannealed surface shows a Fermi-Dirac Fermi edge and therefore shows a metallic behavior. The two quasicrystalline surfaces show a reduced density of states at the Fermi level which is generally referred to as *pseudo gap*. The pseudo gap is a universal but not sufficient criteria for quasicrystallinity [32]. The opening of the pseudo gap at E_f is related to the interaction of the Pseudo Brillouin Zone with the Fermi Surface and satisfies a Hume-Rothery-type relation, as will be described in the section 3.8.

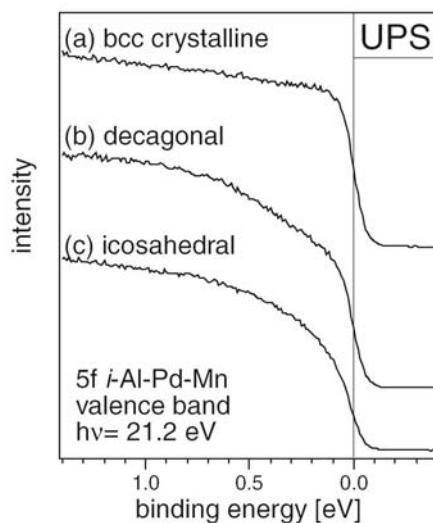


Figure 3.11: UPS Valenceband spectra measured with HeI radiation on 5f i-AlPdMn QC. a) bcc crystalline surface after sputtering b) Mn rich decagonal quasicrystalline overlayer c) bulk-terminated AlPdMn QC surface. While the crystalline overlayer shows a Fermi-Dirac Fermi edge, the QC phases show the so called "pseudo gap", a characteristic reduction of the DOS at the Fermi level for QC's [33].

3.7.3 X-ray Photoelectron Diffraction

XPD has proven a valuable tool to determine the state of the surface of Quasicrystals, especially when undergoing different sample treatments. XPD probes the nearest neighbor real space structure around a photoelectron emitter. The method is element specific by the choice of a specific core level of an atom in the structure under investigation. In first order, XPD is emitter selective but not strongly scatterer selective. In other words, by choosing a core level one selects the atoms of type A sitting in their specific positions. The degree of scattering of the photoelectron wave on the surrounding atom depends on the

atomic type of the scatterer, but the main features reflected by the Forward Focussing (FF) maxima are primarily related to the geometrical arrangement of the emitter and scatter. Therefore, the symmetry elements on the patterns is primarily dominated by the atomic positions and not by the type of atoms if the chosen emitters reside in equivalent positions. The measurements of Fig. 3.12 represent the stereographic projections of the

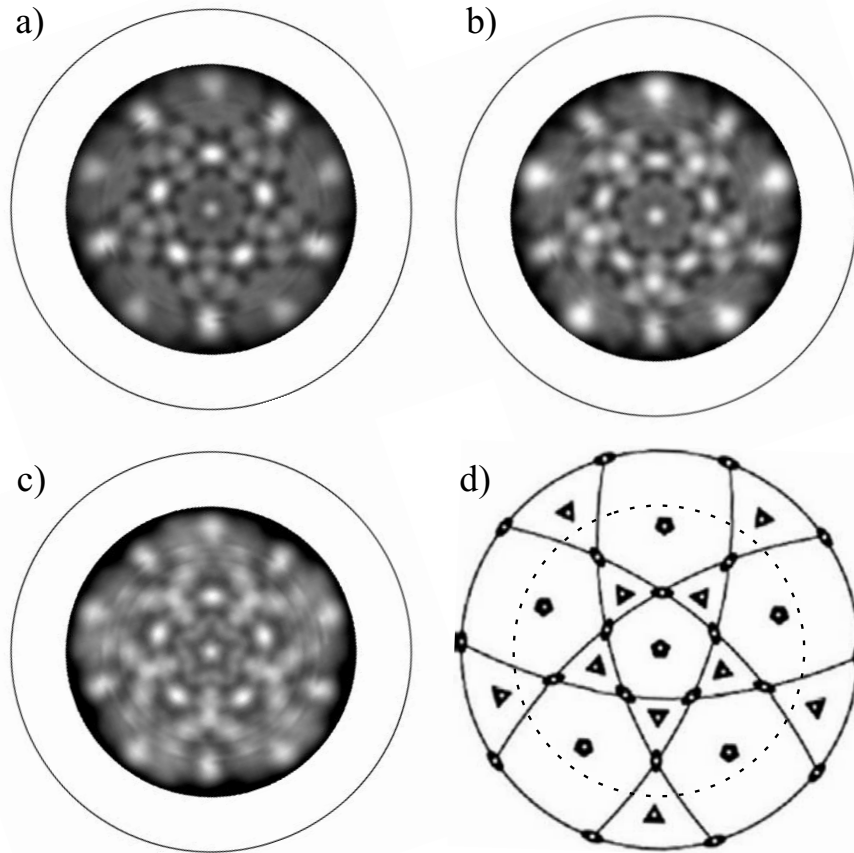


Figure 3.12: XPD patterns measured with Al $K\alpha$ radiation on i-AlPdMn 5f core levels. a) Al 2s at $E_{kin}=1369.4\text{eV}$ b) Pd $3d_{5/2}$ at $E_{kin}=1150\text{eV}$ and c) Mn $2p_{3/2}$ at $E_{kin}=848.2\text{eV}$ d) represents the main icosahedral symmetry elements of the surface plane perpendicular to a 5f axis, namely 2f (ellipses), 3f (triangles) and 5f (pentagons). The outer circle denotes an azimuthal angle of 90° and the dotted line denotes the maximum $\theta=70^\circ$ measured.

measured photoelectron intensity as a function of azimuthal and polar angles in stereographic projection, measured on icosahedral AlPdMn oriented along its 5fold axis. The

respective FF-features can be related to the quasi unit cell structure of the underlying quasicrystal. In Fig. 3.13 a Bergman cluster is represented from different perspectives. Depending on the choice of axis, the nearest neighbor surrounding is in a 5f, 3f or 2f configuration giving rise to the observed symmetry elements around the FF-maxima in XPD. This illustrates the capability of XPD to probe the real space nearest neighbor structure around a emitter. For a comprehensive overview on this topic, the reader is referred to the review paper [34].

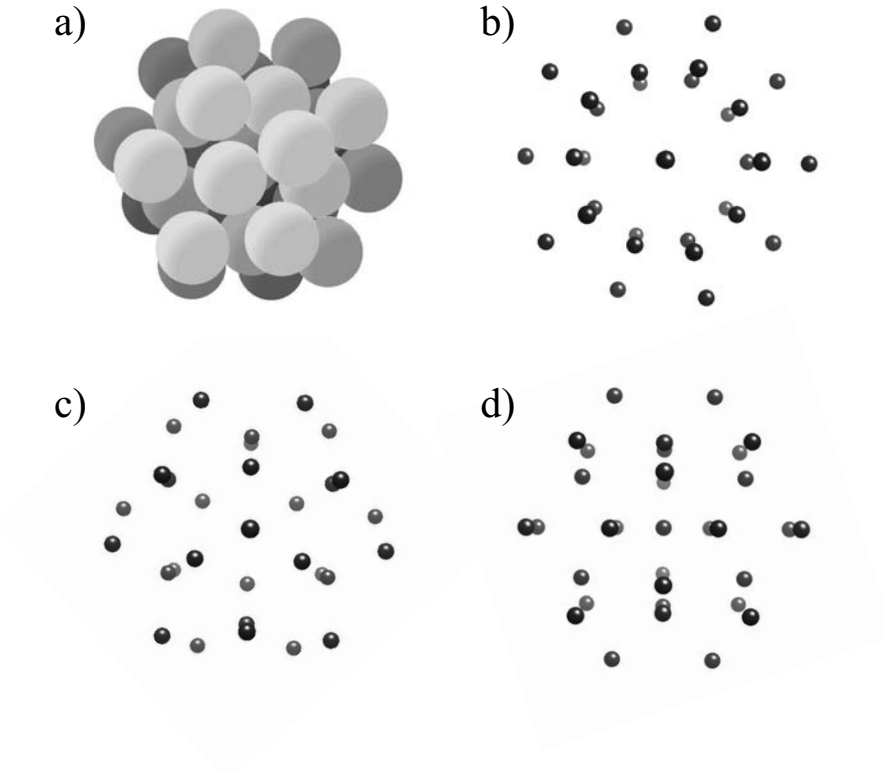


Figure 3.13: Bergman cluster seen from different perspectives a) Bergman cluster b) along a 5f direction c) along a 3f direction d) along a 2f direction. The geometrical atomic arrangement can be directly related to the observed XPD patterns.

3.8 QC's are electronically stabilized

It is experimentally observed, that stable quasicrystals and their approximants all lie on or close a line of constant $e/a=1.86$. e/a is defined as follows:

$$e/a = \sum_i N_i \cdot C_i \quad (3.2)$$

where N_i is the contribution of element i to the conduction band and C_i is the atomic fraction of element i (Reference [35] and references therein). This was further generalized to a constant Valence Electron Concentration (VEC) per unit volume. While e/a may lose its validity for instance in the Cu-rich end of AlCu approximant alloys, the constant VEC per unit volume remains valid [36]. It has been noted by Dong, that '*approximants are those Hume-Rothery crystalline phases that possess approximately the same valence electron concentration as that of the corresponding quasicrystal*' [37]. This empirical rule is the expression of the fact that quasicrystals are electronically stabilized Hume-Rothery alloys [38, 39]. In Hume-Rothery alloys the Fermi Surface touches the Pseudo Brillouin

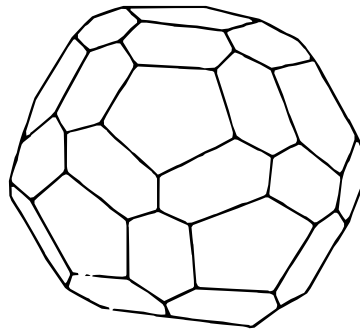


Figure 3.14: Pseudo Brillouin Zone of icosahedral AlCuFe. Note that the Brillouin zone is almost spherical in shape. Data taken from [36].

Zone, i.e. the valence band is filled up to the edge of the Brillouin Zone (BZ) and the BZ has approximately a spherical shape. This is fulfilled for quasicrystals. Figure 3.14 represents the Pseudo-BZ of AlCuFe. According to solid state physics theory (see general solid state physics text books), the intersection of bands with the BZ leads to the formation of a gap.

In the case where the BZ and Fermi Surface are approximately spherical in shape and k_f is very close to the size of the Pseudo-BZ, the atomic structure can be adjusted to lower the total energy of the electrons. Such systems are called *electronically stabilized*. This condition is fulfilled with QC's and their approximants - which explains the structural stability of the structure which might intuitively seem unfavorable.

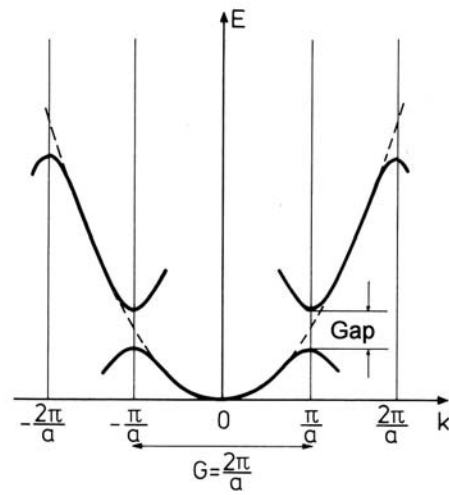


Figure 3.15: Band structure model of a 1D free electron. The intersection of the free electron parabola with the Brillouin Zone leads to the formation of a gap.

References for Chapter 3

- [1] D. Schechtman, I. Blech, D. Gratias, J.W. Cahn, Phys.Rev. Lett. **53**, 1951 (1984)
- [2] D. Levine, P.J. Steinhardt, Phys. Rev. Lett. **53**, 2477 (1984)
- [3] J. Ledieu, R. McGrath, J. Phys. Condens. Matter, **15**, S3113 (2003)
- [4] D.P. DiVincenzo, P.J. Steinhardt (Edts.), *Quasicrystals: The State of the Art*, pp 225-250, (World Scientific, Singapore, 1999)
- [5] B. Grunbaum, G.C. Shepard; *Tilings and Patterns* (San Francisco, Freeman, 1987)
- [6] R. Penrose, Bull. Inst. Math. Appl., **10**, 266 (1974)
- [7] N.G. de Bruijn, K. Nederl. Akad. Wetensch. Proc. Ser. A, **84**, 1 (1981); *ibid.* **84**, 39 (1981); *ibid.* **84**, 53 (1981)
- [8] D.Levine, P.J. Steinhardt, Phys.Rev.Lett. **34**, 596 (1986)
- [9] A.Katz Commun. Math Phys. **118**, 263 (1988)
- [10] D. Gratias, M. Quiquandon, A. Katz, in *Quasicrystals, Current Topics*, E. Belin-Ferré, C. Berger, M. Quiquandon, A. Sadoc (Edts.), (World Scientific, New York, 2000)
- [11] M. Gierer, A. Mikkelsen, M. Gräeber, P. Gille, W. Moritz, Surf. Sci. Lett., **463**, L654 (2000)
- [12] R.D. Diehl, J. Ledieu, N. Ferralis, A.W. Szmodis, R. McGrath, J. Phys. Condens. Matter, **15**, R63 (2003)
- [13] K. Edagawa, K. Suzuki, S. Takeuchi, Phys. Rev. Lett. **85**, 1674 (2000)
- [14] S. Weber, <http://jcrystal.com/steffenweber/qc.html>
- [15] J.M. Dubois, P. Weinland, P. CNRS, Nany, France, Coating Materials for Metal Alloys and Metals and Method, Eur. Patent EP 0356287 A1 and U.S. Patent 5,204,191, April 20, 1993

- [16] N. Rivier, in *Proceedings of the Conference, New Horizons in Quasicrystals: Research and Applications*, pp 188-199, A.I. Goldman, D.J. Sordelet, P.A. Thiel, J.M. Dubois (Edts.), (World Scientific, Singapore, 1997)
- [17] I.M. Hutchings, *Tribology: Friction and wear of engineering materials* (CRC, Boca Raton, FL, 1992)
- [18] R.H. Perry, C.H. Chilton (Edts.), *Chemical Engineers' Handbook* (McGraw-Hill Book, New York, 1973)
- [19] U. Köster, W. Liu, H. Liebertz, M. Michel, *J. Non-Cryst. Solids*, **153-154**, 446 (1993)
- [20] Y. Yokoyama, A. Inoue, T. Masumoto, *Mater. Trans. JIM* **34**, 135 (1993)
- [21] S.S. Kang, J.M. Dubois, J. von Stebut, *J. Mater. Res.* **8**, 2471 (1993)
- [22] J.M. Dubois, *Proceedings of the Conference New Horizons in Quasicrystals: Research and Applications*, pp 208-215, (World Scientific, Singapore, 1997)
- [23] D. Kovar, M. Ready, *J. Am Ceram. Soc.* **77**, 1928 (1994)
- [24] J. Lyons, T. Starr, *J. Am Ceram. Soc.* **77**, 1673 (1994)
- [25] H.E. Boyer, T.L. Gall, *Metals Handbook: Desk Edition*, (American Society for Metals, Metals Park, Ohio, 1984)
- [26] F.R. deBoer, R. Boom, W.C.M. Mattens, A.R. Meidema, A.K. Niessen, *Coehsion in Metals*, (North-Holland, Amsterdam, 1988)
- [27] C.J. Jenks, P.A. Thiel, *Langmuir*, **14**, 1392 (1998)
- [28] D. Popović, D. Naumović, M. Bovet, C. Koitzsch, L. Schlapbach, P. Aebi, *Surf. Sci.* **492**, 294 (2001) and references therein
- [29] M. Gierer, M.A. Van Hove, A. I. Goldman, U. Shen, S.-L. Chang, P.J. Penhero, C.J. Jenks, J.W. Andereg, C.-M. Zhang, P.A. Thiel, *Phys. Rev. B*, **57**(13), 7628 (1998)
- [30] N.R. Shivaparan, V. Shutthanandan, V. Krasemann, R.J. Smith, *Surf. Sci.* **373**, 221 (1997)
- [31] S.-L. Chang, J.W. Andereg, P.A. Thiel, *J. Noncryst. Solids* **195**, 95 (1996)
- [32] T. Fujiwara, T. Yokokawa, *Phys. Rev. Lett.* **66**(3), 333 (1991)
- [33] D. Naumović, P. Aebi, L. Schlapbach, C. Beeli, K. Kunze, T.A. Lograsso, D.W. Delaney, *Phys. Rev. Lett.* **97**, 195506 (2001)

-
- [34] D. Naumović, Prog. Surf. Sci. **75**, 205 (2004)
 - [35] C. Dong, A. Perrot, J.-M. Dubois, E. Belin, Mat. Sci. Forum **150-151**, 403 (1994)
 - [36] C. Dong, Phil. Mag. A, **73**(6), 1519 (1996)
 - [37] C. Dong, Scripta metall. Mater. **33**, 33 (1995)
 - [38] A.P. Tasi, A. Inoue, T. Masumoto, Sci. Rep. of the Res. Inst. Tôhoku Univ. **36**, 99 (1999)
 - [39] E. Belin, Z. Dankházim A, Sadoc, J. M. Dubois, J. Phys.: Cond. Matter **6**, 8771 (1994)

Part II

Oxidation and Reduction of Ag by Plasma treatment

Chapter 4

H₂ plasma treatment of silver contacts: impact on wirebonding performance

M. Biemann, P. Ruffieux, P. Schwaller[†], P. Sudan, L. Schlapbach[†] and P. Gröning

Physics Department, University of Fribourg, P erolles, CH-1700 Fribourg, Switzerland

[†] *Materials Technology Department Empa Thun, Feuerwerkerstrasse 39, CH-3602 Thun*

published in J. Electron. Mat. **(31)**12, 1316 (2002)

The ultrasonic wirebonding performance on Ag bond pads is limited by the presence of oxides and organic contaminants. These contaminations act as lubricants during wirebonding. They reduce the interfacial friction and decrease the heat dissipation between the two contacting materials leading to bad bond quality. Plasma processes have proven to be a valuable tool for eliminating such contaminations and boosting wirebonding performance. We present investigations of the effects of H₂ plasma on oxidized silver films by Photoelectron Spectroscopy and Quartz Crystal Microbalance measurements. The H₂ plasma treatment of Ag bond pads is not a classical surface cleaning process. It is a bulk process and induces a reduction of silver oxide and recrystallization. The high mass transport due to large changes in density during reduction leads to the formation of (111) terminated regions at the surface. This densely packed termination can account for the apparent passivating effect of H₂ plasmas on Ag bond pads, which allows for long term storage in ambient atmosphere without deteriorating bonding performance.

4.1 Introduction

Wirebonding is a standard process used in the semiconductor industry to connect the chip die to external leads. Thermosonic tailless ball bonding - more commonly referred simply as ball bonding - uses an ultrasonic piezo horn that excites a micrometer sized gold ball pressed on the bond pad. The resulting local pressure at the regions in contact is in the GPa range and therefore plastic. A schematic drawing of the contact region is depicted in Fig. 4.1. The heat produced by the friction under the lateral movement of the piezo actuator leads to a rise in local temperature in the asperities in contact. If the dissipated energy at the interface is high enough, pronounced interdiffusion leads to welding of the gold ball contact region with the bond pad material. The evolution of the contact region morphology with time was experimentally investigated by Carrass et al. [1] Under non-UHV conditions, metals are covered by a thin (several nm), organic contamination layer. Such contamination can reduce friction and act as a boundary lubricant [2] and therefore limit the frictional heating at the interface, leading to severely reduced bonding quality. Oxides on the surface can also reduce the frictional heating process or limit the interdiffusion of the elements in contact. This might lead to delamination and therefore higher cost. Kong et al. have investigated the thermodynamics of sliding interfaces in high pressure contacts [3].

The accepted limit for bond failure is below 1 ppm. Further improvements demand a better understanding of the tribological interface to improve process parameters and reduce costs. Therefore, for improved bondability characteristics, a method for removing the contaminants without damaging the delicate electronic devices is needed. Plasmas can be used for surface cleaning / conditioning, but do also offer a much wider variety of industrial applications [4]. In a plasma, the process gases are excited by an external energy source. The adsorption of energy leads to the formation of atomic, excited and ionized species of the process gas as well as electrons and radiation [5,6]. Therefore, by such a process, reactive species can be created without the need for chemical reactions. Furthermore, as the operating pressure of a plasma is usually in the 1mbar to 10⁻⁴mbar regime, the amount of material used for a particular process is very low. Therefore, plasma processes are economically advantageous and ecologically uncritical compared to chemical etching and cleaning procedures that are generally based on hazardous chemicals. Such chemical procedures find their application in semi-conductor industry for chip manufacturing, but plasma processes start to establish themselves in this business for the above mentioned reasons. One application for plasmas is the removal of contaminations from bond pads. Different classes of bond pad materials with respect to contamination can be distinguished:

a.) Materials that do not form an oxide layer (Au, Pt). On those materials, organic contaminations determine the bonding performance.

b.) Materials, forming a stable oxide layer (Al, Si). The properties of the oxide layer limits the bonding process.

c.) Materials that form an incoherent or unstable oxide layer (Ag, Cu, Pd). Materials of this category show bonding characteristics influenced by oxides as well as organic contaminations [7]. Silver is an important material for electronic contacts because it offers the highest thermal and electrical conductivity in the relevant temperature range for semiconductor chips. Standard pull force tests showed that silver bond pads undergoing a Ar/H plasma treatment show distinctly improved bondability performance over untreated samples [7]. This phenomena was studied using a modified ultrasonic wirebonder. A schematic of the setup as well as a characteristic measurement curve is presented in Fig. 4.2. Instead of using a gold ball for the bonding process, a Ni/Au thermocouple is used in the bondability analyzer. This approach gives direct access to the bond ball temperature during the process. The temperature of the bond ball can be directly related to frictional behavior of the two interfaces in contact [8,9]. An alternative design presented by Mayer et al. [10] uses a normal gold ball and the frictional heating is measured by a specially designed bond pad chip. This allows the use of an unmodified ultrasonic wirebonding head, but offers significantly lower sensitivity. The improved bonding properties of the plasma treated Ag samples were identified to be due to removal of contaminants from the silver surface. Plasma treated bond pads offer the possibility to store the surfaces under ambient conditions for days without deteriorating the bondability performance [11]. Up to now, this phenomena was observed but not understood. It was thought that this effect

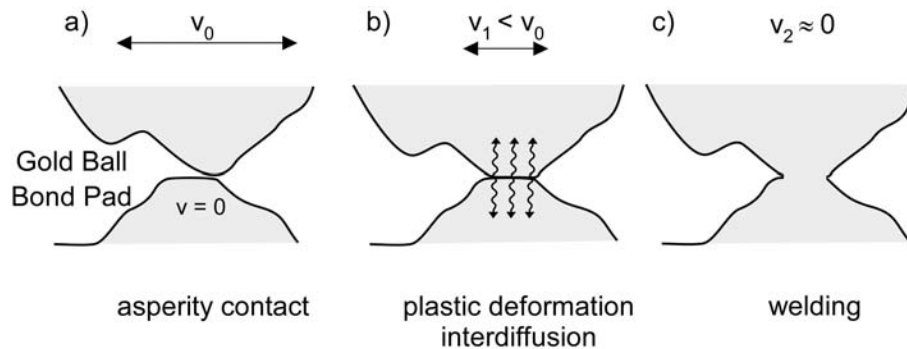


Figure 4.1: (a) Schematic drawing of the contact region in ultrasonic wirebonding a) The bond ball and the bond pad are approached, leading to asperity contact which plastically deform under the high contact pressure. The gold ball moves with a velocity v_0 over the bond pad. b) the lateral movement of the piezo horn induces a frictional heating at the interface. Local welding leads to a irregular stick slip behavior where occasionally formed welding spots form and break. Therefore the average velocity $v_1 < v_0$. c) if the induced heat was sufficient, enough welds have formed to support the lateral force of the piezo horn. A stable bond is formed.

is due to passivation of the Ag surface. It is therefore of interest to study the behavior of the silver oxide system undergoing a H₂ plasma treatment. Studies were made on evaporated Ag as well as Ag single crystals to understand the structural behavior of the silver oxide system undergoing a H₂ plasma treatment. The measurements on the Ag film were performed on in situ evaporated Ag on a quartz crystal microbalance (QCM), giving us insight about the dynamical behavior of the silver/oxide system during the plasma process.

4.2 Experimental

4.2.1 Equipment

All experiments were performed in a modified Omicron photoelectron spectrometer equipped with an Electron Cyclotron Resonance (ECR) plasma source. The base pressure of the system is $5 \cdot 10^{-11}$ mbar. Untreated and plasma-treated Ag single crystal surfaces were investigated by Low Energy Electron Diffraction (LEED), X-ray Photoelectron Spectroscopy (XPS, Mg K Source), Angular Resolved Ultraviolet Photoelectron Spectroscopy (ARUPS, He I source), and X-ray Photoelectron Diffraction (XPD). XPS gives access to chemical composition and bonding state at the surface. XPD and LEED give mainly structural information of the surface. ARUPS gives access to the valence band of the surface and is very sensitive to surface structure and orientation. For all plasma treatments discussed here, the gas pressure during the treatment was in the order of 10^{-2} mbar. The average ion energy under this conditions is in the order of 1 eV for H ions and in the

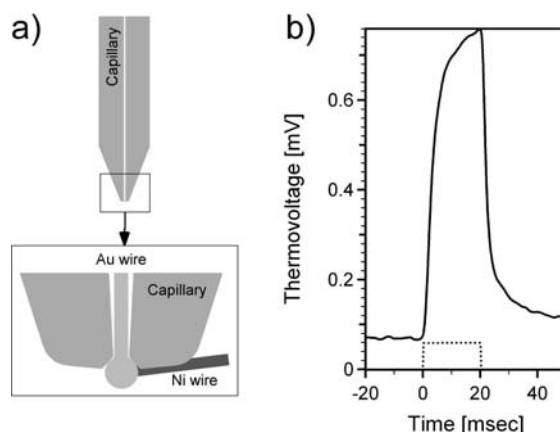


Figure 4.2: (a) Schematic setup of the bondability analyzer head. The Au/Ni thermocouple bond ball is formed by an electrical discharge. b) Typical measurement of the thermovoltage during a bonding process. The dotted line depicts the excitation of the piezo horn

order of 4eV for O ions as measured by analysis of the ion energy distribution with an electrostatic ion energy analyzer [12]. The kinetic energies are below the threshold for sputtering processes. The main function of the plasma is to circumvent the dissociative step of the gas molecules at the surface, providing a high flux of atomic and ionic gas species to the surface.

4.2.2 Sample Preparation

The experiments were performed on Ag(110), Ag(111) single crystal surfaces and on a Ag film evaporated in situ on a QCM. Experiments up to film thickness of 1 μm showed that the process is not thickness limited as long as the treatment time is adjusted accordingly. The results presented here for the QCM were measured on a 40nm Ag film. Before undergoing plasma treatments, the single crystal surface was cleaned by Ar^+ sputtering and annealing cycles. No C or O contaminations could be observed with XPS and sharp LEED and XPD pattern could be observed, reflecting a clean sample with long range order. The Ag film was evaporated in situ on a new QCM crystal to eliminate sources of contamination. The silver oxide was formed using an O_2 plasma. By the plasma process, one can form a thick ($>\mu\text{m}$), homogeneous oxide layer in situ under UHV conditions, avoiding any source of organic contamination [13]. All samples were oxidized in a O_2 plasma for 60min prior to the reduction step. The samples were reduced by exposure to a H_2 plasma. While the single crystal surfaces were analyzed by XPS, XPD, ARUPS and LEED as clean, oxidized and reduced samples, the Ag film in situ evaporated on the QCM was studied by the shift in resonance frequency of the quartz crystal during the treatment. The mass uptake is directly related to the resonance frequency through the Sauerbrey equation for rigid films:

$$\Delta f = -\frac{1}{C_f} \Delta m \quad (4.1)$$

C_f is called the Sauerbrey constant and is independent of the film properties. The frequency shift along with the atomic masses served as a basis to calculate the O/Ag ratio of the Ag film.

4.3 Results and Discussion

4.3.1 Oxidation

4.3.1.1 QCM measurements

The oxidation of the evaporated Ag film was monitored during the O_2 plasma treatment and is presented in Fig. 4.3. After 60min of oxidation, the O/Ag ratio was 1.3, thus

showing that the oxide formed is AgO with an excess in oxygen. The oxygen content slightly relaxed after switching off the plasma and stabilized at O/Ag = 1.2. XPS and ARUPS spectra on the oxidation were presented elsewhere [14]. Evaluation of the O/Ag ratio from the peak integral taking in account the analyzer transmission [15] and cross sections of the respective elements are in agreement with the observations with the QCM and show the formation of AgO.

4.3.1.2 Photoelectron spectroscopy measurements

XPS spectra were measured on the single crystal surfaces. The Ag 3d spectra are presented in Fig. 4.4. The oxidation of the surface leads to a negative peak shift in binding energy of the Ag 3d level. The observed peak shift corresponds to the expected values for silver oxides [16–21].

4.3.2 H₂ plasma treatments

4.3.2.1 QCM measurements

The effects of the H₂ plasma on the formerly oxidized Ag film by QCM is depicted in Fig. 4.5. The arrow denotes the time when the plasma was switched on. The H₂ plasma treatment results in a complete reduction of the oxidized Ag film. The convergence of the O/Ag ratio to zero indicates that the observed reduction is a bulk phenomena. In the

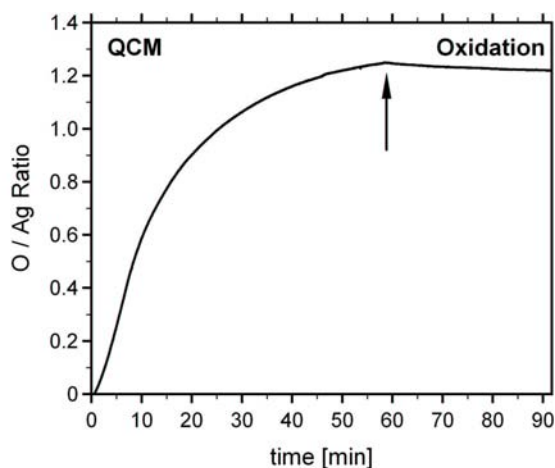


Figure 4.3: O/Ag ratio as calculated from the change in resonance frequency of a QCM crystal evaporated in situ with 40nm Ag and subjected to O₂ plasma treatment. The arrow denotes the time when the plasma was switched off. The O/Ag ratio stabilizes around 1.2 indicating a oxide AgO with excess oxygen. The reduction of the oxygen content after plasma switch-off is most likely due to desorption of surface oxygen.

first phase of the reduction a linear decrease in the O/Ag ratio can be observed. Such a behavior is to be expected if the reduction is limited by the available flux of H atoms and ions on the surface and not by diffusion processes. The linear decrease changes into an exponential decay as a function of time at a O/Ag ratio of about 0.5 as indicated by the

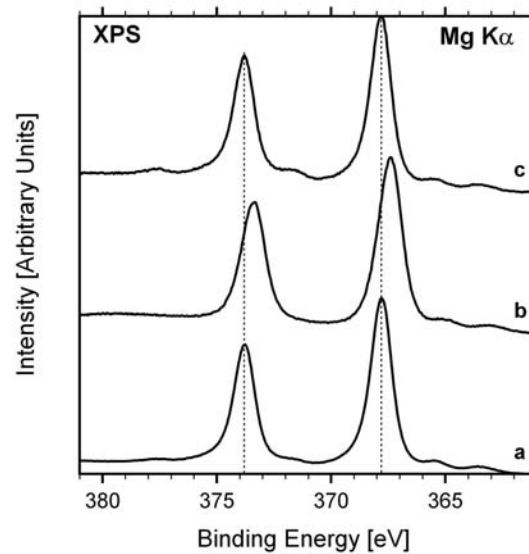


Figure 4.4: Ag 3d spectra as measured by XPS on Ag(111) with Mg K radiation. a.) clean Ag sample b.) after oxidation in an O₂ plasma, the peak shift corresponds to the expected binding energy shift for silver oxides c.) silver peak after reduction in an H₂ plasma. The peaks are shifted back to their initial position.

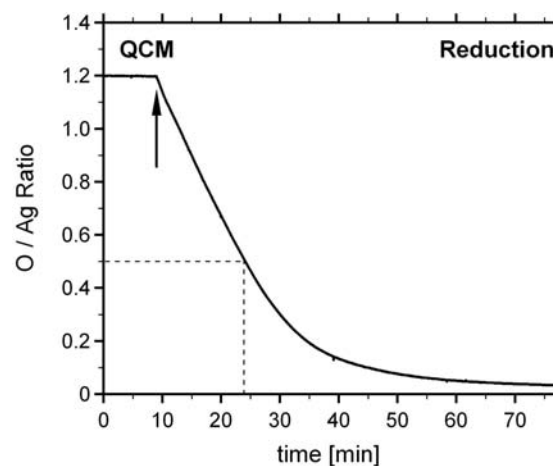


Figure 4.5: : O/Ag ratio of a formerly oxidized 40nm Ag film on a QCM crystal during H₂ plasma treatment. The arrow indicates the switching on of the H₂ plasma.

dashed line in Fig. 4.5. The incoming flux of reducing species is no longer the limiting factor. The diffusion of O from the bulk in a layer where the reduction takes place limits the reduction rate of the oxide layer. As the frequency shift does not drop below the initial frequency shift for the clean Ag film, we can safely exclude sputtering as a means for eliminating the oxide layer. Bohdansky et al. have presented a model which describes the sputtering yield as a function of energy [22]. In view of the low kinetic energy of the H₂ plasma ions, sputtering is not expected. Already little sputtering of Ag would be easily detectable in the QCM signal because even severe hydrogen uptake would not compensate for little Ag losses due to the high difference in atomic mass between the two elements. The investigated reaction is therefore a bulk reduction of the oxide and not only limited to a surface or near surface layer.

4.3.2.2 Photoelectron spectroscopy measurements

The XPS spectra in Fig. 4 shows that the Ag 3d level shifts back to its initial position during the reduction in an H₂ plasma. The valence band spectra as measured by ARUPS presented in Fig. 6 show a) the Ag(110) spectra in measured along the surface normal, b)-d) the Ag(111) spectra along the surface normal, along the [110] direction and along the [100] direction respectively and e) the Ag(110) valence band after undergoing several oxidation and reduction cycles. From the spectra a) and b) it is clear that ARUPS depends strongly on the surface termination under investigation. It represents therefore a good tool for the study of phenomena depending strongly on crystallographic orientation. The spectra e) exhibits characteristic features of the (111) surface orientation and can well be fitted using a superposition of the spectra a)-d). Therefore we conclude, that after oxidation and reduction cycles on Ag(110) there exist regions at the surface with a (111) termination in coexistence with (110) terminated regions. The (111) surface is the most dense surface orientation while the (110) plane is the most open of the low index surface planes. During the reduction, the Ag atoms are highly mobile due to the increase in density from the oxide to the metal. While some regions form a (110) surface due to still present local information about the original crystal structure, other regions start to form a (111) termination because it is energetically favorable to form a densely packed atom layer. The oxidation of a material in contact with oxygen is determined by the sticking coefficient of the gas molecule and the dissociation rate at the surface. It is well known that the sticking coefficient of O on Ag surfaces is very low with the (111) termination exhibiting the lowest (10^{-6}) and the (110) termination exhibiting the highest (10^{-3}) sticking coefficient. Furthermore, oxygen diffusion through (111) planes is only activated at elevated temperatures ($T > 923\text{K}$) [23]. The passivation effect of hydrogen plasma treatment on Ag can therefore be understood being due to the formation of regions with (111) termination at the surface. This regions are less prone to reoxidation because of the

much reduced sticking probability of oxygen. Further, adsorbed oxygen can only diffuse through grain boundaries, defects and the remaining (110) terminated surface regions. The (111) facets themselves do not allow for oxygen diffusion at room temperature. Also, as the amount of area with (111) termination increases, the amount of (110) termination decreases. The oxidation increases the layer thickness by a factor of about 2 due to the differences in density between the metal and the oxide [13]. During reduction, the decrease in volume induces a large mass transport and the surface has a tendency to reorganize in the lowest energy surface orientation, which leads to the observed effect. (110) features could not be observed in similar experiments on the (111) surface as this orientation is already energetically favorable.

4.4 Conclusions

In this work, we presented the reduction of silver oxide by H_2 plasma treatment. In any case, the oxide film could be reduced, even up to complete bulk oxidation treatments. Our

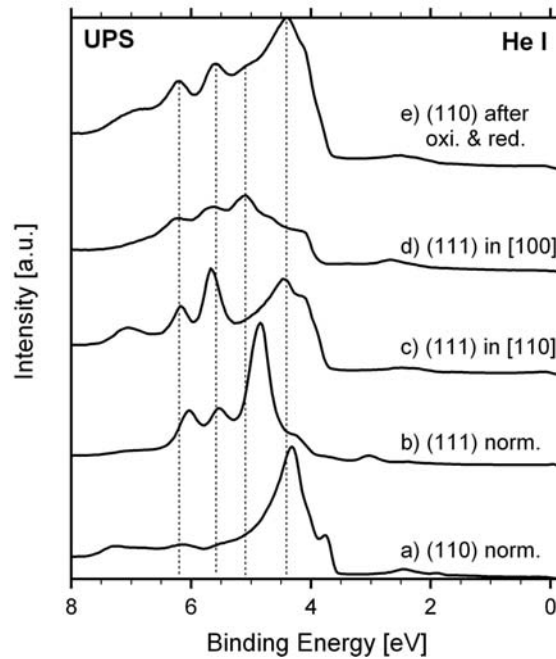


Figure 4.6: ARUPS valence band spectra. a) clean Ag(110) along the surface normal b) clean Ag(111) along the surface normal c) clean Ag(111) in the (110) direction d) clean Ag(111) in the (100) direction e) Ag(110) valence band after several oxidation / reduction cycles in O_2 and H_2 plasmas. The valence band spectra shows features characteristic for the (111) orientation. The spectra e) can well be fitted by a superposition of the spectra a)-d).

investigations by dynamic measurements with a QCM prove that the reduction mechanism is a bulk reduction. After the H₂ plasma treatment, the surface is free of any contaminations and bulk Ag oxides are eliminated. The absence of contaminations is favorable in the tribological contact of the bond ball and the sample surface. Reproducible and good bonding conditions are therefore created by such a treatment. For Ag(110), a formation of (111) terminated regions could be observed for multiple oxidation/reduction cycles. The formation of (110) regions on Ag(111) could not be observed. It is known that the (111) plane of silver shows a pronounced lower sticking coefficient to O₂ compared to (110) and limits the bulk diffusion of oxygen to diffusion at defects and grain boundaries. The claimed passivation effect of the Ar/H₂ plasma cleaning method on Ag can be understood by the tendency of the highly mobile Ag atoms to form (111) terminated regions during the reduction process. It inhibits the reoxidation of the surface and delays the building up of the critical 3nm contamination layer above which contact pressure does not suffice to guarantee a metal-metal contact.

4.5 Acknowledgements

Skilful technical assistance was provided by R. Schmid, E. Mooser, O. Raetzo, Ch. Neurer and F. Bourqui. This work was financially supported by the Swiss National Science Foundation.

References for Chapter 4

- [1] A. Carrass, V.P. Jaecklin, DVS **173**,135 (1991)
- [2] B. Persson, *Sliding Friction, Second Edition*, (Springer, Berlin, 2000)
- [3] H.S. Kong, M.F. Ashby, MRS Bulletin **16(10)**,41 (1991)
- [4] *Handbook of Thin Film Materials Vol1: Deposition and processing of thin films*, (Academic Press, San Diego, 2002)
- [5] A. Grill, *Cold Plasma in Materials Fabrication*, (IEEE Press, New York, 1993)
- [6] B. Chapman, *Glow Discharge Processes*, (Wiley and Sons, New York, 1980)
- [7] A. Schneuwly, P. Gröning, L. Schlapbach, V.P. Jaecklin, J. of Electron. Mat. **27**, 990 (1998)
- [8] A. Schneuwly, P. Gröning, L. Schlapbach, G. Müller, J. of Electron. Mat. **27**, 1254 (1998)
- [9] P. Schwaller, P. Gröning, A. Schneuwly, P. Boschung, E. Müller, M. Blanc, L. Schlapbach, Ultrasonics **38**, 212 (2002)
- [10] M. Mayer, O. Paul, D. Bolliger, H. Baltes, Proc. ECTC 463-468 (1999)
- [11] Balzers Instruments, PO 1000, FL-9496 Balzers, Lichtenstein, Product Documentation of LFC 150
- [12] J.E. Klemberg-Spicher, O.M. Küttel, L. Martinu, M.R. Wertheimer, Thin Solid Films **193/194**, 965 (1990)
- [13] E. Farhat, A. Donnadiou, J. Robin, Thin Solid Films **29**, 319 (1975)
- [14] M. Biemann, P. Schwaller, P. Ruffieux, O. Gröning, L. Schlapbach, P. Gröning, Phys. Rev. B **65**, 235431 (2002)
- [15] P. Ruffieux, P. Schwaller, O. Gröning, L. Schlapbach, P. Gröning, Q.C. Herd, D. Funnemann, J. Westermann, Rev. Sci. Instrum. **71**, 3635 (2000)

- [16] G. Schön, *Acta Chemica Scandinavica* **27**, 2623 (1973)
- [17] J.S. Hammond, S.W. Gaarestroom, N. Winograd, *Anal. Chem.* **47**, 2193 (1975)
- [18] R.C Ross, R. Sherman, R.A. Bunger, *Solar Energy Materials* **19**, 55 (1989)
- [19] M. Boker, *Surf. Sci. Lett.* **155**, L276 (1985)
- [20] L. H. Tjeng, M.B.J. Meinders, J. van Elp, J. Ghijsen, G.A. Sawatzky, R.L. Johnson, *Phys. Rev. B.* **41**, 3190 (1990)
- [21] G. B. Hoflund, Z. F. Hazos, G.N. Salaita, *Phys. Rev. B.* **62**, 11126 (2000)
- [22] J. Bohdansky, J. Roth, H.L. Bay, *J. Appl. Phys.* **51(5)**, 2861 (1980)
- [23] A.J. Nagy, G. Mestl, R. Schlögl, *J. of Catal.* **188**, 58 (1999)

Chapter 5

AgO investigated by Photoelectron Spectroscopy: Evidence for mixed valence

M. Biemann, P. Schwaller[†], P. Ruffieux, O. Gröning[†], L. Schlapbach and P. Gröning

Physics Department, University of Fribourg, P erolles, CH-1700 Fribourg, Switzerland

[†] *Materials Technology Department Empa Thun, Feuerwerkerstrasse 39, CH-3602 Thun*

published in Phys. Rev. B **65**, 235431 (2002)

We present Photoelectron Spectroscopy investigations of in-situ prepared AgO. The sample was prepared by room temperature oxidation of Ag in an Electron Cyclotron Resonance O₂ plasma. In contrast to other measurements based on ex-situ prepared AgO powder samples, our investigations show a distinct double peak structure of the O 1s signal with a remarkable chemical shift of 2.9eV between the two O 1s components. These two components can not be motivated from a crystallographic point of view as the oxygen sites are all equivalent in the unit cell. We interpret this double peak structure as a characteristic feature of AgO and discuss it in terms of mixed valences.

5.1 Introduction

Silver oxides have been extensively studied in the past due to their high importance in numerous technical applications. For example, the interaction of silver surfaces with

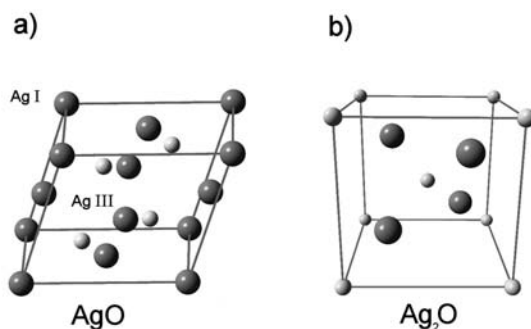


Figure 5.1: Unit cells of the AgO and Ag₂O crystal structure. [13]

oxygen plays a key role for the silver-catalyzed epoxidation of ethylene [1] and the partial oxidation of methanol to formaldehyde [2]. Silver partially oxidizes the reactants instead of producing pure combustion products. Therefore a detailed knowledge of silver oxide surfaces is important for the understanding of catalytical phenomena. Photoelectron Spectroscopy (PES) has proven to be an important tool to study silver oxide surfaces. There exists a wide variety of PES data for the two silver oxides AgO and Ag₂O, dating back as far as to the early days of PES [3–9]. In the literature, also theoretical work on the topic can be found [10–12]. AgO has a monoclinic structure (Fig. 5.1a) containing two inequivalent silver sites. Ag I is twofold coordinated by oxygen while Ag III is fourfold coordinated by O atoms. All oxygen sites are equivalent. AgO is an n-type semiconductor [15]. Ag₂O (Fig. 5.1b) is cubic with 6 atoms per unit cell. The oxygen atoms form a bcc lattice and are tetrahedrally coordinated by Ag atoms. The bonding in Ag₂O is primarily ionic with Ag⁺ and O²⁻ valences [11] making Ag₂O an insulator with an electronic gap of 1eV [7] as observed by UPS. Much work has been devoted to the investigation of silver oxides, however the identification of the oxygen species from PES spectra remains controversial. To some extent this is due to the fact that many groups base their measurements on powder samples transferred to Ultra High Vacuum (UHV) conditions [3, 8, 9]. Contaminations due to the contact with ambient atmosphere lead to additional oxygen species, complicating the interpretation considerably. Furthermore, AgO is an unstable oxide: it starts to decompose over 100°C into Ag₂O which itself decomposes above 300°C [9]. For Ag₂O, Tjeng et al. [7] presented an in-situ preparation method based on a free radical oxygen source. From their work it is obvious that the elimination of contributions from surface contaminations facilitates the interpretation of the spectra. Farhat et al. [14–16] produced AgO by O₂ plasma treatment of Ag films evaporated on Quartz Crystal Microbalance (QCM) crystals, but no measurements of the oxide with PES were performed. The role of the plasma is primarily to bypass the dissociative adsorption step. It has been shown by Outlaw et al. [17] that oxygen diffusion

into the bulk can be increased by more than an order of magnitude if the gas is dissociated in a plasma. In this paper we will, to our knowledge for the first time, present PES data of in-situ prepared AgO by room temperature oxidation in an Electron Cyclotron Resonance (ECR) O₂ plasma. The measurements reveal a distinct double peak structure in the O 1s signal, which we relate to a mixed valency on the oxygen sites.

5.2 Experimental

All experiments were performed in a modified Omicron photoelectron spectrometer equipped with an EA 125 HR electron analyzer and an Electron Cyclotron Resonance (ECR) plasma chamber with 2.45GHz microwave source. The base pressure of the system is $5 \cdot 10^{-11}$ mbar. Untreated Ag single crystal surfaces and plasma-treated surfaces were investigated by Low Energy Electron Diffraction (LEED), X-ray Photoelectron Spectroscopy (XPS) and Ultraviolet Photoelectron Spectroscopy (UPS). As photon sources we used non-monochromatized Mg K α X-rays (1253.6eV), monochromatized Al K α X-rays (1486.6eV) and He I radiation (21.2eV) from a gas discharge lamp. The spectrometer is calibrated to a Au4f_{7/2} binding energy (BE) of 83.8eV. AgO was produced by an ECR O₂ plasma. Prior to oxidation, Ag single crystal surfaces were sputtered with 1.5keV Ar⁺ ions and annealed at ~ 800 K until a sharp LEED pattern was obtained and no C or O contaminations could be observed by XPS. The oxidation step was performed applying an O₂ ECR plasma during 30min. The gas pressure during the treatment was $3 \cdot 10^{-2}$ mbar and the sample was set to ground potential. The major difference between oxidation under gas flow at elevated temperatures and a ECR plasma treatment is the presence of atomic, excited and ionized atomic species in the plasma. Further, the bulk sample is at RT, but the kinetic energy of the ions striking the surface leads to a local heating of the surface [22,23]. The operation pressure of ECR plasmas is 10^{-4} - 10^{-1} mbar. In this pressure range, the electrons and heavy species in the plasma are not in thermodynamical equilibrium, even on a scale in the order of the Debye length λ_D (~ 0.1 mm). In such low pressure plasmas the electron temperature T_e is in the range of eV while the temperatures of the heavy species (ions, neutrals) are all in the order of kT (~ 25 meV). Therefore such plasmas are generally referred to as cold plasmas [18]. Though the ion temperature T_{Ions} is room temperature (RT), a sample inserted into a cold plasma will be struck by ions with a kinetic energy of a few eV. This is due to the fact that a plasma is always positively charged. The excess ions caused by the higher recombination rate of the highly mobile electrons at the container walls compared to the heavy ions ($\langle v_e \rangle \gg \langle v_{Ions} \rangle \leftrightarrow T_e \gg T_{Ions}$) gives rise to the so called plasma potential. This plasma potential defines the kinetic energy with which the ions strike the surface [19] and depends on the type of plasma as well as the geometry of the setup. Such variations in design can lead to a distinctly different

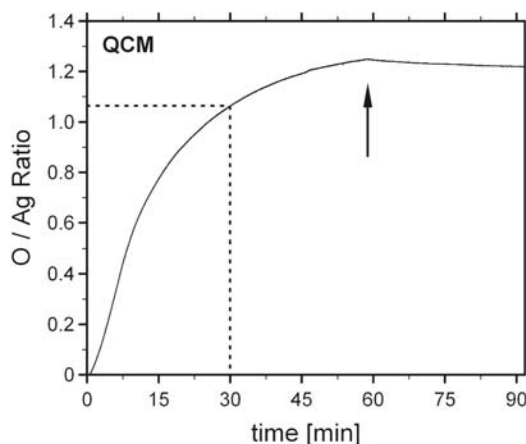


Figure 5.2: O/Ag Ratio during oxidation of a 50nm Ag film evaporated on a QCM crystal with gold electrodes. The O/Ag ratio is about 1.05 after 30min, underlining the conclusion of AgO formation. The arrow indicates the point where the plasma was switched off.

composition of the plasma [18, 19]. For our setup, the ion current density is 25 nA/mm^2 and the average O ion energy is about 4eV for the given parameters as measured by an electrostatic ion energy analyzer [20].

5.3 Results and Discussion

5.3.1 QCM

A 50nm Ag film evaporated in situ on a QCM crystal was exposed to the O_2 plasma under identical conditions as the Ag single crystals. The mass uptake during oxidation can be calculated from the dynamically measured change in resonance frequency of the vibrating microbalance crystal. The resulting O /Ag ratio is presented in Fig. 5.2. After 30min of oxidation, the O / Ag ratio is 1.05 and therefore an oxidation time of 30min on the single crystal surfaces was applied. Under the used conditions, AgO layers with well over $1\mu\text{m}$ thickness can be prepared. During the plasma treatment, the film changed its color from silver to golden/brownish followed by a dark grey appearance. The brownish color is generally associated with Ag_2O , while the dark grey color is associated with AgO [21]. The same phenomena in color change could also be observed on the single crystal surfaces.

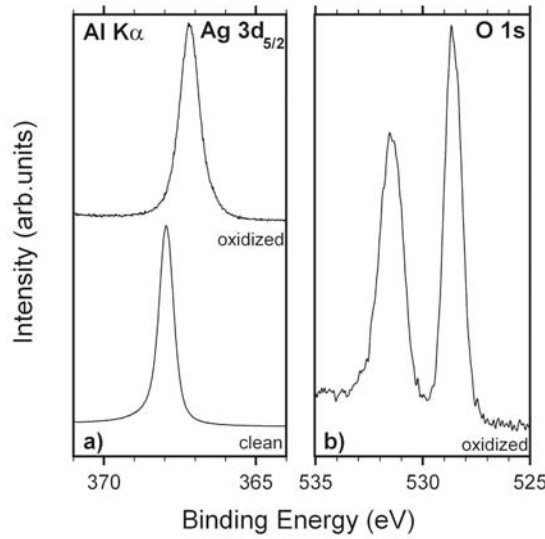


Figure 5.3: Ag $3d_{5/2}$ and O $1s$ signals of clean and oxidized Ag(110) by ECR plasma as measured by XPS with monochromatized Al $K\alpha$ radiation. a) Ag $3d_{5/2}$ signal: the oxidized surface shows a peak shift of -0.8eV from 368.0eV to 367.2eV and a broadening of 0.2eV to 0.76eV compared to the sputtered and annealed sample. b) O $1s$ signal: The double peak structure comprises a lower BE component at 528.6eV with a FWHM of 0.9eV and a higher BE component of equal intensity at 531.5eV with a FWHM of 1.3eV .

5.3.2 XPS

Experiments presented in the following were performed on Ag(110), the most open surface of the low index silver planes. Measurements on the (111) surface revealed identical results in XPS and are therefore not presented. The Ag $3d_{5/2}$ spectra for the clean and the oxidized sample measured with monochromatized Al $K\alpha$, are shown in Fig. 5.3a. The corresponding peak positions and peak widths are resumed in Table 5.3.2. Fig. 5.3b shows the O $1s$ spectra after oxidation, exhibiting two distinct components. The lower BE component is centered at 528.6eV with a FWHM of 0.9eV . The higher BE component is centered at 531.5eV with a FWHM of 1.3eV . This second peak was not observed by Tjeng et al. [7] on Ag_2O . Their spectra exhibit a single O $1s$ signal, at a BE of 528.9eV . For shorter plasma exposure times, where we assume that predominantly Ag_2O is present, we observe the same O $1s$ signal as Tjeng et al. [7] denoted in Table 5.3.2. But with ongoing oxidation, the lower BE component shifts further down to 528.6eV and the initially small but present higher BE component grows in intensity until the peak integral of both components are equal. Quantitative analysis of the Ag and O peak intensities taking into account cross sections [24] and analyzer transmission [25] yields an O/Ag ratio of 1.0 ± 0.1 which perfectly matches the comparative measurement of the evaporated Ag film on the QCM presented above. Grazing angle measurements show little

difference in the intensity between the two components as compared to normal emission after complete oxidation. The investigated AgO surface is therefore at least homogeneous within the analysis depth of XPS ($\sim 5\text{nm}$). We understand the double peak O 1s structure with a chemical shift of 2.9eV as a characteristic feature of AgO. The oxidation reaction

compound	electron level	BE [eV]	FWHM [eV]
Ag	Ag 3d _{5/2}	368.0	0.57
AgO	Ag 3d _{5/2}	367.2	0.76
	O 1s	528.6	0.9
Ag ₂ O*	O 1s	531.5	1.3
	Ag 3d _{5/2}	367.6	
	O 1s	528.9	1.2

Table 5.1: Binding energies and peak widths of Ag 3d_{5/2} and O 1s signals as measured with monochromatized Al K α . Values denoted by * are taken from Tjeng et al. [7] and were measured with non-monochromatized Al K α .

by ECR plasma treatment differs from the reaction caused by a free radical source as used by Tjeng et al. [7] due to the presence of ions in the ECR plasma. Therefore, the presence of the ions is a necessity for producing AgO. We would like to stress that no traces of C were measured, excluding therefore contributions to the oxygen signal from CO species. An identical chemical shift between two O 1s components as in our measurements was observed by Boronin et al. [27]. In their work, they interpret the higher BE component to be due to adsorption of excited oxygen species from the plasma on the Ag₂O surface. They understand this peak as an adsorbate species because it vanishes by dosing the surface with 10⁸L of ethylene at 125°C. However, Tanaka et al. [26] have shown by TDS experiments that dosing of AgO with ethylene leads to a bulk reduction of AgO to Ag₂O. Furthermore, over 100°C AgO starts to decompose into Ag₂O. Therefore, the loss of the higher BE component might as well be due to a reduction of a bulk oxide species different from Ag₂O. As revealed by grazing angle measurements, we can safely exclude in our case that the higher binding energy component is due to adsorbed oxygen at the surface. We further exclude that the higher BE O 1s component is due to a mixture of atomic subsurface oxygen and hydroxyl groups as suggested by Weaver et al. [9] and Hoflund et al. [8]. For early stages of the oxidation the lower BE component dominates the spectra. If the higher BE O 1s component arises from hydroxyl groups, one would expect that this peak dominates the spectra in an initial phase as the hydrogen content is highest after ignition of the plasma due to desorption of the chamber walls and gas system. Subsurface contributions should be built up before oxygen diffuses into the bulk and would therefore lead to a dominant higher BE component for lower plasma exposure times. This is in contradiction to our observations. As mentioned above, the oxygen sites in AgO are

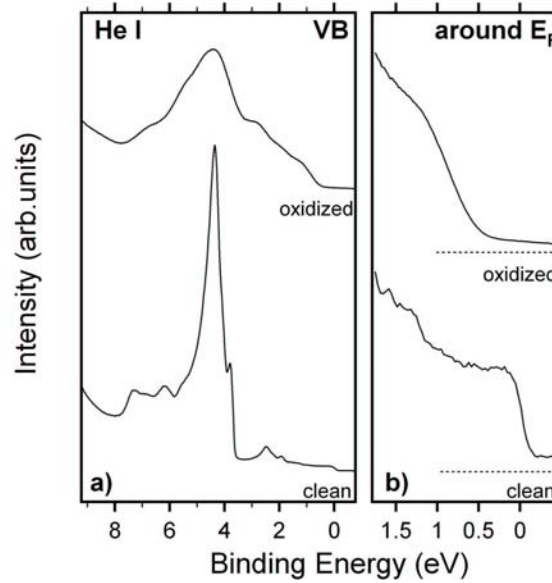


Figure 5.4: Valence band spectra measured with HeI radiation at normal emission. a) clean and oxidized Ag(110) surface b) shows the Fermi edges for the corresponding measurements. The top of the valenceband of the oxidized sample is located 0.52eV below the fermi level.

structurally equivalent and therefore the two peaks can not be explained from different local structures. In a theoretical work on AgO of Park et al. [10] it is suggested, that a large number of holes exist on the oxygen sites. They suggest that silver is present as Ag^+ and Ag^{2+} valences rather than as Ag^+ and Ag^{3+} and consequently, there must exist an considerable amount of oxygen with -1 valency. In a charge transfer model, a negative peak shift in BE for the element with higher electronegativity is expected. For most oxides, the oxygen BE shows a negative peak shift compared to the BE of the free molecule. The shift scales with the valency of the oxygen. In Ag_2O the oxygen atom is present as O^{2-} . As seen in the measurements of Tjeng et al. [7] an atom in this configuration shows a BE around 529eV. As the lower BE O 1s component of our measurements lies close to 529eV, we understand this peak to reflect essentially a -2 valency. The higher BE O 1s component at 531.5eV shows a remarkably smaller shift and a distinct broadening compared to the free molecule and therefore the charge transfer respectively the valency must be different. For O^- , such a behavior is expected. The increased peak width indicates a significantly shorter life time of the particular state. Mixed valences can be understood as the fluctuation of the valence state of an atom, i.e. where a valence electron hops between neighboring atoms. Separate binding energy peaks are therefore possible for atoms with different oxidation states in structurally equivalent sites [28]. Kohn et al. [29] have theoretically shown, that the observation of the phenomena is not related to the characteristic time of the photoemission process. They showed that a double peak

structure can be observed for $U \gg V$ where U is the interaction energy of the electrons on the same nucleus and V is a coupling energy describing the transition between the two electronic configurations. Detailed theoretical discussion of the phenomena can be found in the given reference. We understand the presented results as the manifestation of a -1/-2 valency fluctuation on the structurally equivalent O sites. As the electrostatic screening of the other electrons in Ag is considerably higher, the manifestation of the mixed valency as resolvable peaks on the localized 4d levels of Ag can not be expected with the present setup. It rather manifests itself as a broadening of the signal which can not be resolved from the broadening due to signal components which arise from different local structures around the inequivalent Ag sites.

5.3.3 UPS

Fig. 5.4 shows the UPS spectra measured in normal emission (i.e. at the Γ -point) for clean Ag(110) and after 30min of oxidation. (Note, that the produced oxide is not a single crystal.) Figure 5.4b shows the region around E_F . For Ag_2O an electronic gap of 1eV was found by Tjeng et al. [7]. We find a gap of 1.09eV for an intermediate oxidation step while for long oxidations a gap of 0.52eV was found. We define the gap as the intersection of a linear fit in the background region before the gap and in the edge of the occupied states to E_F . The closing of the gap with ongoing oxidation corroborates the assumption of oxygen acting as a dopant, as suggested in the model by Park et al. [10].

5.3.4 Stability

The question of stability of AgO surfaces was addressed by exposing them for prolonged periods to UHV conditions, to ambient atmosphere and to X-ray radiation. These experiments were motivated to understand the behavior of the produced surface exposed to conditions comparable to AgO powder samples transferred to UHV conditions. After 20 h in UHV at RT, the surface did not show any variations in composition and therefore can be considered stable in UHV for our measurements. The results after contact to ambient atmosphere are presented in Fig. 5.5a (XPS) and Fig. 5.5b (UPS). The higher BE O 1s component is strongly reduced while C contaminations lead to multiple O 1s components around 529.5eV like the ones seen by Hoflund et al. [8] indicated by a broad, gray shaded peak in Fig. 5.5a. Along with the reduction of the higher BE O 1s signal, also a shift of the lower BE signal to higher BE is observed. The respective UPS spectra shown in the Fig. 5.5b reveal an opening of the gap by 0.2eV to 0.72eV. Such a behavior is expected for the surface decomposition of AgO into Ag_2O , the more stable and insulating oxide due to contact with air. These findings lead us to the assumption that AgO powder samples exposed to air already decompose at the surface before any measurement can be

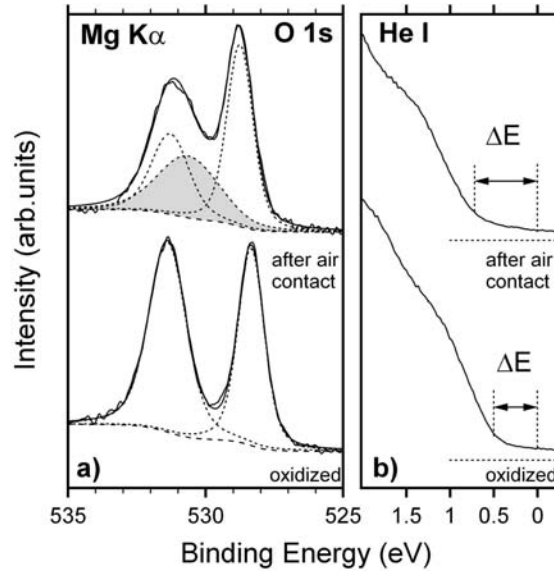


Figure 5.5: O 1s signal of a oxidized $1\mu\text{m}$ Ag film on Au. a) O 1s XPS spectra after oxidation and exposure to ambient atmosphere for 17 h. b) respective UPS spectra around E_F . The gray shaded area indicates contributions from carbon contaminations. The gap in the UPS spectra increases from 0.5eV to 0.72eV after the contact with air.

performed. Therefore, even if the bulk sample is still AgO in nature, the near surface region within the analysis depth of PES is altered in a way that the gained data are not characteristic for the system. Also, the always present carbon contaminations in powder samples lead to additional O 1s contributions, making interpretation of the results a very difficult and ambiguous task. Ar^+ sputtering does not recover the original AgO surface as the sputtering process itself leads to decomposition of AgO. We observed a degeneration of the oxide under long therm X-ray exposure. The higher BE signal decreased about 10% compared to the lower binding energy component after 7h of X Ray exposure. As such a behavior can be observed also with the monochromatic source it is clearly not only related to IR radiation of the X Ray source. The elimination of the higher BE peak indicates a decomposition to the more stable Ag_2O . As our measurements do not demand such extensive radiation exposure, the presented results are not affected by stability issues. Nevertheless, one needs to be aware that PES measurements on AgO can be affected by radiation exposure and demand an in situ preparation of the oxide.

5.4 Discussion and Summary

In this work, we presented PES data of in-situ prepared AgO by ECR plasma treatment at room temperature. To our knowledge, there are no comparable measurements in literature

based on in-situ prepared AgO. The PES spectra exhibit a double peak structure with an BE difference of 2.9eV. We interpret this double peak structure as a characteristic feature of AgO due to a mixed valence state of the structurally equivalent oxygen atoms. Park et al. [10] suggested that Ag atoms are present in a Ag^+ and Ag^{2+} valency rather than Ag^+ and Ag^{3+} as a consequence of e^- holes on the oxygen sites. Therefore, there exist oxygen sites which do exhibit -1 and -2 valences and our measurements do represent this two component.

5.5 Acknowledgements

Skillful technical assistance was provided by R. Schmid, E. Mooser, O. Raetzo, Ch. Neururer, and F. Bourqui. This work was supported by the Swiss National Science Foundation.

References for Chapter 5

- [1] R.A. Van Santen, H.P.C.E. Kuipers, *Adv. Catal.* **35**, 265 (1987)
- [2] A. J. Nagy, G. Mestl, R. Schlögl, *Journal of Catalysis* **188**, 58 (1999)
- [3] G. Schön, *Acta Chemica Scandinavica* **27**, 2623 (1973)
- [4] J. S. Hammond, S. W. Gaareestroom, N. Winograd, *Anal. Chem.* **47**, 2193 (1975)
- [5] R. C. Ross, R. Sherman, R. A. Bunger, *Solar Energy Materials* **19**, 55, (1989)
- [6] M. Bowker, *Surf. Sci. Lett.* **155**, L276 (1985)
- [7] L. H. Tjeng, M. B. J. Meinders, J. van Elp, J. Ghijsen, G. A. Sawatzky, R. L. Johnson, *Phys. Rev. B* **41**, 3190 (1990)
- [8] G. B. Hoflund, Z. F. Hazos, G. N. Salaita, *Phys. Rev. B.* **62**, 11126 (2000)
- [9] J. F. Weaver, G. B. Hoflund, *J. Phys. Chem.* **98**, 8519 (1994)
- [10] K.T. Park, D.L. Novikov, V.A. Gubanov, A.J. Freeman, *Phys. Rev. B* **49**, 4425 (1994)
- [11] A. Deb, A.K. Chatterjee, *J. Phys.* **10**, 11719 (1998)
- [12] M. T. Czyżyk, R. A. de Groot, G. Dalba, P. Fornasini, A. Kisiel, F. Rocca, E. Burattini, *Phys. Rev. B* **39**, 9831 (1989)
- [13] P. Villars, L.D. Calvert, *Pearson's Handbook of Crystallographic Data for Intermetallic Phases Vol.1*, (American Society for Metals ,Metals Park, 1985)
- [14] E. Farhat, S. Robin-Kandare, *Thin Solid Films*, **23**, 315 (1974)
- [15] E. Farhat, A. Donnadiou, J. Robin, *Thin Solid Films* **29**,319 (1975)
- [16] E. Farhat, A. Donnadiou, J. Robin, *Thin Solid Films* **30**, 83, (1975)

- [17] R.A. Outlaw, D. Wu, M.R. Davidson, G.B. Hofflund, *J. Vac. Sci. Technol. A* **10**(4), 1497 (1992)
- [18] A. Grill, *Cold Plasma in Materials Fabrication*, (IEEE Press, New York, 1993)
- [19] B. Chapman, *Glow Discharge Processes*, (Wiley and Sons, New York, 1980)
- [20] J.E. Klemberg-Spicher, O.M. Küttel, L. Martinu, M.R. Wertheimer, *Thin Solid Films* **193/194**, 965 (1990)
- [21] N.N. Greenwood, A. Earnshaw, *Chemistry of the Elements*, (2nd edition, Butterworth, UK, 1997)
- [22] J. Bohdansky, J. Roth, H.L. Bay, *J. Appl. Phys.* **51**, 2861 (1980)
- [23] G. Carter, D.G. Armour, *Thin Solid Films*, **80**, 13 (1981)
- [24] J.J. Yeh, I. Lindau, *At. Data Nucl. Data Tables* **32** (1985)
- [25] P. Ruffieux, P. Schwaller, O. Gröning, L. Schlapbach, P. Gröning, Q.C. Herd, D. Funnemann, J. Westermann, *Rev. Sci. Instrum.* **71**, 3635 (2000)
- [26] S. Tanaka, T. Yamashina, *J. of Catalysis* **40**, 140 (1975)
- [27] A.I. Boronin, S.V. Koscheev, K.T. Murzakhmetov, V.I. Avdeev, G.M. Zhidomirov, *Appl. Surf. Sci.* **165**, 9 (2000)
- [28] W.L. Jolly in C.R. Brundle, A.D. Baker, *Electron Spectroscopy: Theory, Techniques and Applications Vol.1*, (Academic Press, London, 1977)
- [29] W. Kohn, T.K. Ledd, *Phylos. Mag.* **45**, 313 (1982)

Part III

Growth of Cu thin films on i-AlPdMn 5f single crystals

Chapter 6

Evidence for strained cubic structure in 1D quasiperiodic buckling of Cu thin films on icosahedral AlPdMn

M. Biemann^{*†}, O. Gröning[†], P. Ruffieux[†], J. Ledieu[‡], R. Fasel[†], R. Widmer[†], D. Naumović^{*} and P.A. Gröning[†]

^{}Physics Department, University of Fribourg, Pérolles, CH-1700 Fribourg, Switzerland*

[†]Empa Materials Science and Technology, Überlandstrasse 129, 8600 Dübendorf, Switzerland

[‡]University of Liverpool, Surface Science Research Center, Oxford Street, Liverpool, L69 3BX, Liverpool UK

to be submitted

In this work, we present a comprehensive investigation on the growth of Cu on the fivefold surface on a icosahedral Al₇₀Pd₂₀Mn₁₀ single crystal up to 5ML thickness. The Cu films develop a 1D Fibonacci superstructure with $L=7.3\text{\AA}$ and $S=4.5\text{\AA}$ above 3ML as first reported by Ledieu et al. by Low Energy Electron Diffraction and Scanning Tunneling Microscope measurements. In their work, the local atomic arrangement still remained unresolved. We investigate the nearest neighbor configuration by X-Ray Photoelectron Diffraction to address this question and discuss the origin of the corresponding Low Energy Electron Diffraction patterns by simple model calculations. We find, that the Low Energy Electron Diffraction patterns reflect the aperiodic super structure as observed by Scanning Tunneling Microscopy and that the underlying atoms are not in periodic arrangement on a larger scale. Nevertheless, the

local structure defined by the nearest neighbor configuration is well defined below 3ML and in agreement with a fcc(110) structure, present in 5 domains rotated by 72° but is lost when the super structure starts to appear at 4ML and above. Along with the loss in local structure and development of large scale order, a decrease in film/substrate interaction is manifested by a change in the chemical shift of the Cu and Pd core levels measured by X-ray Photoelectron Spectroscopy. The observed behavior can be understood based on a strain relief driven mechanism as an underlying mechanism for the formation of this superstructure.

6.1 Introduction

Quasicrystals (QC) were first reported in 1984 by Schechtman et al. in AlMn binary alloys [1]. From the discovery of Schechtman to nowadays a whole variety of systems have been found to produce quasicrystalline phases. These systems are binary or ternary alloys, frequently - but not exclusively - rich in Al. Only few of these alloys do form stable phases allowing to grow macroscopic, single grain crystals on the millimeter scale. Among these alloys, icosahedral (i) AlPdMn is the most prominent member, being aperiodic in all three dimensions [2]. The discovery of QC's caused a major turmoil in the crystallographic community as the observed 5-, 8-, 10- and 12-fold symmetries are not compatible with the concept of translation symmetry which is at the heart of traditional crystallographic classification schemes. At the time, QC's simply fell outside the boundaries of these schemes. Since then, the definition of a crystal has been recast in a less restrictive framework based on diffraction properties to embrace periodic and aperiodic crystals. The origin of sharp diffraction peaks observed for QC's has been resolved, realizing that Bragg diffraction does not require long-range periodic order, it only necessitates long-range positional order, i.e. the origin of diffraction peaks are directions of high atomic density in constructive phase coherence [3]. New theoretical concepts regarding the structure and origin of diffraction patterns for these systems have been developed. They are based on tilings of clusters and submanifolds of higher dimensional regular lattices to generate aperiodic quasicrystalline structures. Although the connection of atomic structure and resulting diffraction patterns have been resolved and are reasonably well understood, the interplay between aperiodic atomic and electronic structure in quasicrystals is still far from the understanding of their classical periodic counterparts. The classic description of the valence electronic structure is fundamentally linked to the translational symmetry of ordinary crystals, which results in the concept of Bloch states. One of the consequences of the Bloch picture is that the wavevector attributed to a valence electron state is only defined modulo a reciprocal lattice vector. This is a direct consequence of the relation between momentum conservation and translation symmetry. How these concepts can be adopted to aperiodic systems is not yet fully understood, although significant progress has been made [4]. Indications of an exceptional relation between the aperiodic atomic arrangement and the valence electronic structure can be found in several macroscopic physical properties of QC's. They possess for instance an unusually low conductivity, which shows a semiconductor type temperature dependence (positive temperature coefficient) and which decreases with increasing structural perfection. This behavior markedly differs from ordinary alloys with similar composition and from the constituent elements [2, 5–8]. The major hindrance to fully enlighten the role of the aperiodic atomic structure on the electronic properties lies in the fact that the influence of the atomic arrangement and the complex chemical structure are difficult to disentangle. In this view it would be highly desirable to have a pure

element, preferably a simple metal, in a quasicrystalline form. But up to this point, no single element system is known to form a QC phase. Using the surface of a single crystal QC as template for the growth of metal thin films, aiming at transferring the aperiodicity of the QC substrate to the film, would be an obvious first approach to achieve the goal of fabricating simple metal aperiodic structures. Such thin film ‘QC’s’ could then be subjected to surface sensitive techniques for the characterisation of the electronic properties like Angle Resolved Photoelectron Emission Spectroscopy (ARPES)

The adsorption of Cu and Al on AlPdMn single crystals have been extensively studied by J. Ledieu et al. with Scanning Tunneling Microscopy (STM) and Low Energy Electron Diffraction (LEED) [9–11]. The growth was found to be layer by layer up to 8ML of Cu. In their work, a clear transfer of aperiodicity from the substrate to the Cu film can be observed above 3ML of Cu. This is manifested by a row-like superstructure with interrow distances of $L=7.3\text{\AA}$ and $S=4.5\text{\AA}$ in a Fibonacci sequence. These rows are present in 10 orientations n times 36° rotated. However, the driving forces behind this Fibonacci superstructure and the underlying atomic arrangement of the Cu film is not yet resolved. In this work, we will present measurements of thin Cu films (0.5-5ML) on an $\text{Al}_{70}\text{Pd}_{20}\text{Mn}_{10}$ single crystal with the surface oriented perpendicular to its fivefold axis. It is the aim of this study to gain insight in the local arrangement of the Cu atoms in these films. We address this question by X-ray Photoelectron Diffraction (XPD) in the low coverage regime (below 5ML). This method is element specific and probes the real space nearest neighbor (NN) configuration of the atoms under investigation [12]. It is therefore ideally suited to give complementary information on existing STM data [9] Furthermore, we will discuss the information which can be gained from the individual methods, namely STM, LEED and XPD and we will motivate that they are in fact complementary as already pointed out by Petukhov et al. [13].

6.2 Experimental

All experiments were performed in a modified photoelectron spectrometer equipped with an EA 125 HR electron analyzer and a room temperature UHV AFM/STM from Omicron Nanotechnology GmbH. The base pressure of the system is $5 \cdot 10^{-11}$ mbar. Structural information is gained by LEED, XPD and STM. For X-ray Photoelectron Spectroscopy (XPS) and XPD, we used non-monochromatized Al $K\alpha$ (1486.6eV) and Mg $K\alpha$ X-rays (1253.6eV) radiation. The spectrometer is calibrated to a Au $4f_{7/2}$ binding energy (BE) of 83.8eV. We used an $\text{Al}_{70}\text{Pd}_{20}\text{Mn}_{10}$ single crystals, grown by the Czochralsky technique at the IMF in Jülich [14]. The sample was cut to exhibit the 5 fold surface plane and mechanically polished. The single crystal was prepared by repetitive cycles using Ar ion sputtering cycles (30min, 1.5keV ion energy) followed by annealing (650°C for 2h). The

sample cleanliness and structural quality was checked by XPS and XPD measurements (absence of O Auger in XPS, characteristic XPD pattern [15]) as well as the LEED pattern (low signal to noise, presence of spots in the energy range from 10eV to 380eV). STM shows a terraced structure with an average terrace width of about 100nm and terrace lengths generally well exceeding this value (Fig. 6.1). The thin films were evaporated

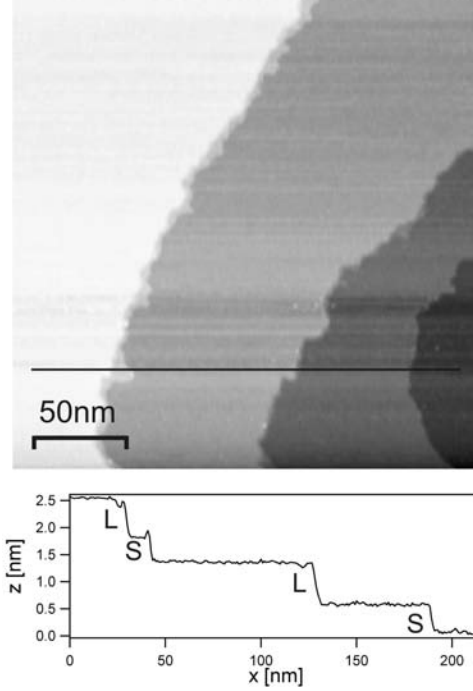


Figure 6.1: a) 250nm x 250nm section of a the QC substrate after preparation. The sample exhibits a flat, terraced surface structure with terraces generally well exceeding 100nm.

in situ with a resistively heated Cu (purity 99.999%) evaporator while the sample was held at room temperature (RT) during evaporation. Film thickness was calibrated using a Quartz Crystal Monitor (QCM). The evaporation rate was set to 1 Å/min (0.55ML/min using the interlayer distance of fcc Cu). The base pressure of the chamber was always below 10^{-9} mbar during preparation and in the low 10^{-10} mbar regime during analysis.

6.3 Results and Discussion

We have monitored the early growth stages of the Cu film on the AlPdMn surface by measuring the evolution of the core level photoemission lines of Al 2s, Pd 3d, Mn 2p and Cu 2p as a function of the Cu thickness. With increasing Cu film thickness the photoemission signals from the substrate are attenuated as a function of the inelastic mean free path of the photoelectron, which is dependent in first approximation on the

kinetic energy E_{kin} of the electron only [16]. In order to minimize the influence of the mean free path on the determination of element concentration ratios we measure the core levels in question at kinetic energies as close as possible which also reduces the error from the analyzer transmission function. We achieve this by measuring the Al 2s and Cu 3s with Mg $K\alpha$ radiation while the other peaks were measured with Al $K\alpha$. By this, E_{kin} for Al 2s and Pd $3d_{5/2}$ are almost identical and they suffer equal relative losses due to inelastic scattering, i.e. we achieve identical probing depth. The peak integral of the Al 2s, Pd

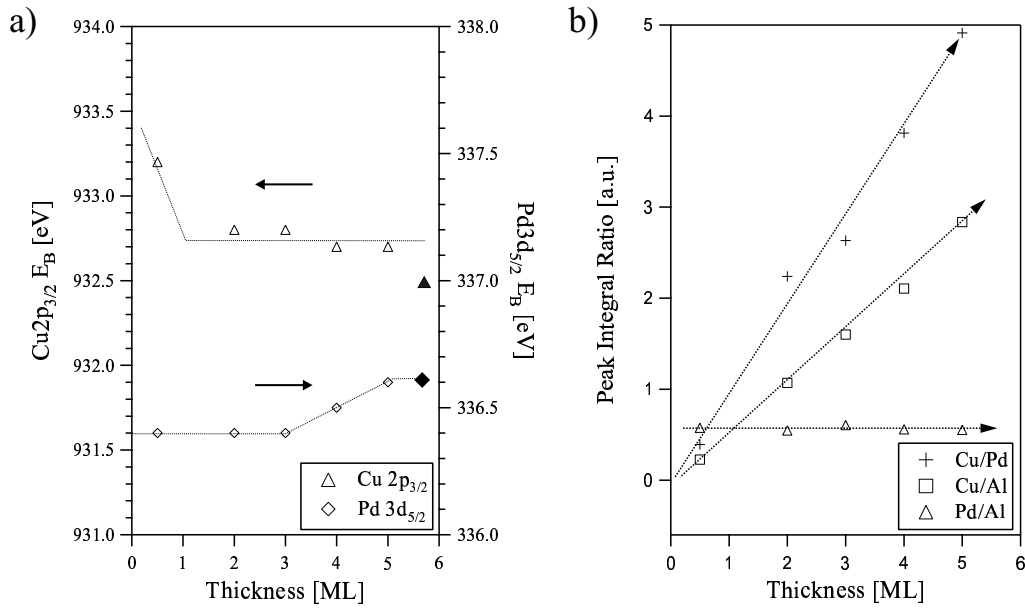


Figure 6.2: a.) Peak position of the Cu $2p_{3/2}$ and Pd $3d_{5/2}$ core levels as a function of Cu thickness. The full symbols are the values for Pd in the bare QC substrate and for Cu on a Cu(111) single crystal. b.) Evolution of peak integral ratios for Al 2s, Pd $3d_{5/2}$ and Cu $2p_{3/2}$ for 0.5-5ML.

$3d_{5/2}$, Cu 3s and Cu $2p_{3/2}$ core levels were determined by peak fitting routines. Figure 6.2a shows the dependency of Cu core level binding energy E_B as a function of the Cu thickness. It drops from 933.2 eV at 0.5 ML to $932.7\text{eV} \pm 0.1\text{eV}$ at thicknesses of 2 ML and above. This indicates the formation of a Cu wetting layer on the QC substrate. The Al 2s core level is unaffected by the Cu interaction and lies at $E_B = 117.4\text{eV} \pm 0.1\text{eV}$ (not shown). Note that in bulk AlCu alloys the same behavior is observed [17]. The Pd peak position shifts to lower E_B below 3 ML of Cu and evolves to the bulk value of Pd in the clean QC substrate above 3 ML. These findings suggest a change in the chemical environment of Cu and Pd at the respective thicknesses mentioned. In Fig. 6.2b we display the Pd/Al-, Cu/Pd- and Cu/Al-peak integral ratios after correction for elemental cross section and analyzer transmission [18]. As we can see from these measurements, the Cu/Pd- and

Cu/Al-ratio increase linearly while the Pd/Al-ratio stays constant. The constant Pd/Al-ratio proves that none of the bulk elements diffuses preferentially in the Cu film and are identically attenuated by the Cu overlayer. The linear behavior of the Cu/Al ratio in this thickness regime is in agreement with a Stransky-Krastanov growth model and in agreement with observations in STM where the individual layers are not entirely filled before the next layer starts to grow. Upon the sequence of Cu film thicknesses the LEED pattern displays a pronounced series of changes. Figure 6.3 shows the two LEED patterns in inverted gray scale for the clean AIPdMn surface and the 4ML Cu film on AIPdMn. By increasing the primary electron energy, the LEED spots converge towards the surface normal direction during the whole series of Cu thicknesses and therefore no faceting is taking place [19, 20]. Up to 3ML, the substrate LEED pattern gradually vanishes, until a thickness of 3ML where no sharp LEED spots from the substrate can be observed any more. At this coverage only diffuse spots at the k_{\square} position in a 10f configuration can be observed. The spots at k_{\diamond} and k_{\triangle} represent features with phase coherence at a longer distance and start to reappear from 3ML upwards. Prominent features on the QC substrate LEED pattern and the Cu film LEED pattern have been marked for convenience and are summarized in table 6.1. An essential observation is the fact, that the LEED patterns of the Cu films do develop reflexes at the same positions as in the QC-substrate. This fact rises the question in as much the quasicrystalline structure of the substrate is transferred to the copper film.

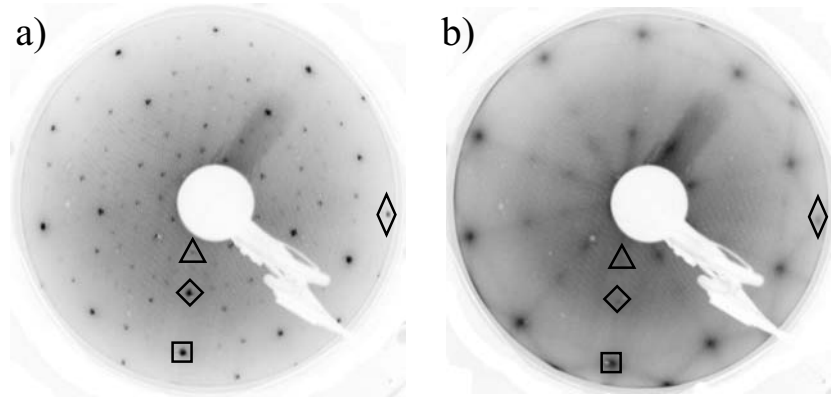


Figure 6.3: LEED patterns recorded at 60eV a) clean i-AIPdMn surface, certain k-values have been marked as a guide to the eye b) LEED pattern of 4ML Cu evaporated on i-AIPdMn at RT

The topographic structure of the Cu film at 5ML is investigated by STM and a typical image is presented in Fig. 6.4. The copper film on AIPdMn develops a topographic 1D super structure in form of row-like stripes which are preferentially aligned along the long side of the islands. Two distinct spacings, L and S can be defined, where the ratio of the $S=4.5\text{\AA}$ and $L=7.3\text{\AA}$ segments are related by the golden ratio $\tau = \frac{1+\sqrt{5}}{2} \approx 1.61\dots$. The

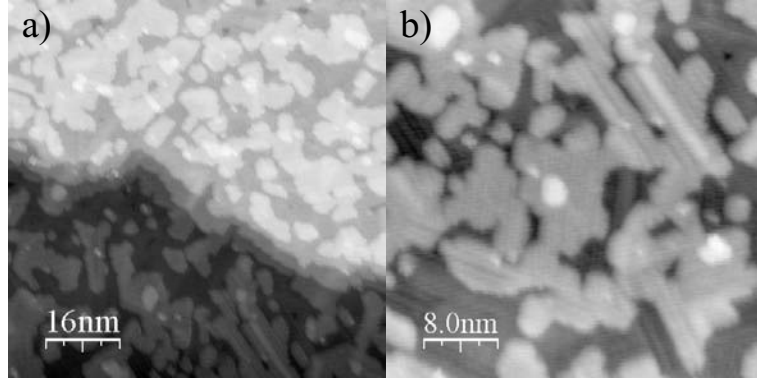


Figure 6.4: a) 100nm x 100nm section of a 5ML Cu Film on i-AlPdMn 5f evaporated at RT, measured by STM. b) 40nm x 40nm section, clearly showing the Fibonacci pattern on the surface as described by Ledieu et al. [9]

interstripe spacings are a segment of a term of the Fibonacci sequence. The height corrugation of these stripes is 0.25\AA . A comparison between the LEED and Fourier transformed

k [\AA^{-1}]	LEED	STM FFT	Calculation
k_{\diamond}	3.2 ± 0.1		
k_{\square}	2.7 ± 0.1	2.7	2.65
k_{\circ}	1.7 ± 0.1	1.7	1.63
k_{\triangle}	1.1 ± 0.1	1.06	1.02

Table 6.1: k-values from LEED patterns compared to the values obtained of a 40nm x 40nm STM image of the QC terrace and a calculated pattern of the Fibonacci structure as described later in the text.

STM image of the clean substrate further underlines the correlation between the Cu film and the QC substrate. The FFT from an STM measurement on the bare QC shows spots at the same wavevectors as in LEED (Table 6.1). Our measurements are in agreement with the findings presented by Ledieu et al. and this demonstrates the equivalence of the experimental conditions. For a complete description of the film morphology observed by STM the reader is referred to [9].

The reappearance of LEED spots above 3ML Cu on AlPdMn with signatures of an aperiodic structure (10f symmetry and τ -relationship) rises the question: What is the origin of the LEED Spots? Do we have the situation of a truly aperiodic Cu film on the QC substrate? In fact, one can suppose many structures which can produce an LEED pattern with quasiperiodic k-vector relationship (in this context referred to as Fibonacci LEED pattern). Let us shortly summarize their origin to aid the interpretation. LEED spots originate from the Bragg-reflection of the electrons at high symmetry planes of

the substrate, more specific of high symmetry rows of the substrate surface. In classical crystals the relation to the real space structure is straight forward via the construction of the reciprocal space. This direct relation still holds for the aperiodic case however the reciprocal space construction is not straight forward as in the case of a periodic crystal. In the case of Cu on AlPdMn we need to expect that we have 5 domain orientations of the Cu film due to the symmetry of the substrate. This leaves us with the general situation that we have domains with a specific internal structure and these domains are then distributed and oriented on the substrate according to the substrate surface structure. In this sense we define three parameter to depict this situation in a general context:

1. The distance relationship between domains being either periodic or quasiperiodic (global order)
2. The atomic structure within the domain being periodic or quasiperiodic (local order)
3. The domain size being larger or smaller than a critical size d_{crit} to develop LEED spots.

The parameter d_{crit} is the minimal needed lateral domain extension to create visible constructive phase coherence in LEED assuming no long range correlation among the different domains. The possible diffraction spot patterns and the underlying structure are summarized in Table 6.2.

case	local order	global order	diffraction spot pattern
1	periodic, $>d_{crit}$	periodic	periodic
2	periodic, $<d_{crit}$	periodic	periodic
3	periodic, $>d_{crit}$	quasiperiodic	periodic+Fibonacci
4	periodic, $<d_{crit}$	quasiperiodic	Fibonacci
5	quasiperiodic	periodic	periodic+Fibonacci
6	quasiperiodic	quasiperiodic	Fibonacci

Table 6.2: Possible diffraction spot patterns based on the the type and lateral extension of local ordering and the global translational relationship among those domains. We speak of periodic global ordering if a periodic translation rule between the domains can be defined while we denote quasiperiodic global ordering as a distance between domains related to the Fibonacci sequence. Therefore, the term global order as we use it does not make any restrictions on the local order. A periodic diffraction spot has a even numbered ratio between the k-values while a Fibonacci pattern shows a ratio related to the golden mean τ

The cases 1, 2, 3 and 5 are either self explanatory or do not apply in the presented case. The cases 4 and 6 deserve closer inspection for which we performed simple model

calculations. We start by distributing a sequence stripes with gaussian height profiles spaced according to a LS-sequence with $L=7.3\text{\AA}$ and $S=4.5\text{\AA}$, representing a Fibonacci superstructure in the direction normal to the stripes. The interrow spacing is chosen according to the observations in STM measurements. The resulting pattern is $5f$ rotated and superimposed to generate a quasiperiodic 2D structure. The FFT of this simulated real space structure represents a simple simulation of the reciprocal space structure probed by LEED. The corresponding maximas do very well match the k -values measured in the LEED patterns of our Cu films and therefore we conclude that the LEED spots reflect the quasiperiodic superstructure in the Cu film.

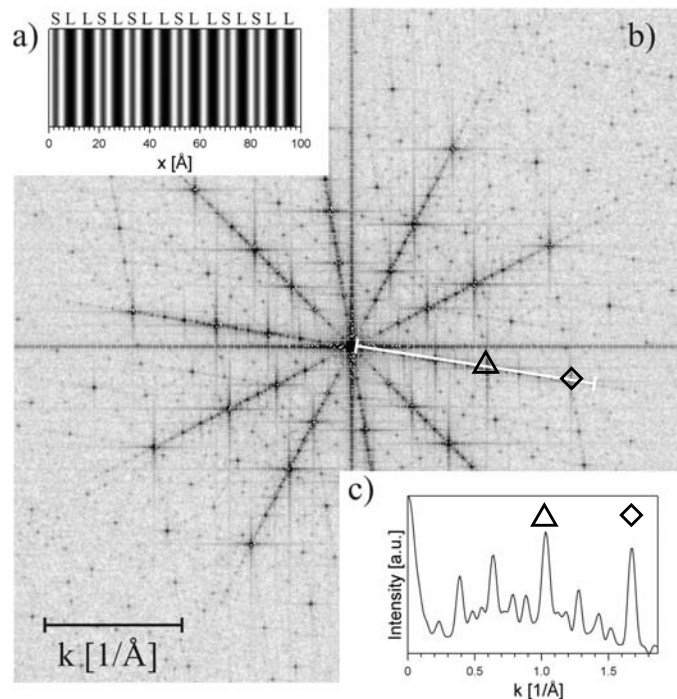


Figure 6.5: Simulation of LEED pattern by FFT a) The real space structure consists of stripes with gaussian line shape. The interline distance is taken according to a Fibonacci sequence with $S=4.5\text{\AA}$ and $L=7.3\text{\AA}$. The pattern is superimposed by a $5f$ rotation to represent the superposition of the individual diffraction patterns. b) calculated FFT pattern reflects the reciprocal space c) Line cut as marked in b) by a line.

To simulate the effect of localized periodicity (case 4), let's assume that the origin of the z -corrugation is a strain relief mechanism. The underlying periodic arrangement of atoms releases strain with a z -relaxation at distances according to L and S and consequently the inplane positions are relaxed as to keep the unit cell volume approximately constant. Therefore, a local periodicity on the length scale of L and S exists. This can be considered as an aperiodic generalization of the model proposed by Ocko et al. [21]

for the thickness induced buckling of Cu on Au(001). This was modelled by distributing periodically one (S) and two (L) gaussian height profiles between the S and L maxima to define a local periodicity as depicted in Fig. 6.6. Globally, the individual stripes (representing atomic scattering planes) between the L and S segments will remain in aperiodic phase relationship to each other. The effect of the addition of this locally defined periodicity manifest itself by an increased spectral weight at higher k-values in Fig. 6.5, i.e. around the k-values given by the local periodicity. But there is no overall periodic phase coherence and consequently no periodic spacing of the intensity maximas. The cases 4 and 6 are therefore not necessarily distinguishable and LEED can not rule out periodicity on the local scale in this system.

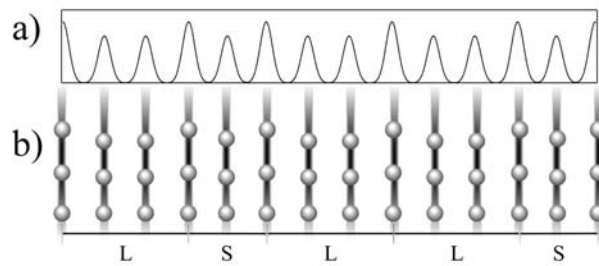


Figure 6.6: The eventual presence of short range periodicity is modelled by distributing equidistantly 1 respectively 2 gaussian height profiles between the quasiperiodic L and S z-relaxations. a) 1D Gauss model b) atomic scattering planes modelled. The individual rows are not related by a translation due to the quasiperiodic L/S spacing.

In order to gain complementary information to clarify the Cu structure, XPD is well suited. The main reason for this is that it can probe element specific the real space atomic nearest-neighbor configuration with the high surface sensitivity as in XPS. By measuring the XPS core level peak intensity as a function of azimuthal and polar emission direction from the sample, a map of the spherical emission intensity for all emission lines and elements of interest from a sample can be generated. At high kinetic energies (typically above 500eV), these emission maps are dominated by the so called Forward Focussing effect, which describes the effect of highest emission probability in the nearest or next-nearest neighbor directions. In our case, we measured the spherical emission intensity maps from 0° - 70° polar angle with respect to the surface normal and 0° - 360° azimuthal angle with a total of 3458 points. The data is represented by stereographic projection of the emission intensity mapped to azimuthal and polar angle in the hemisphere normal to the surface. Therefore, high intensity in these maps directly represents the local geometrical arrangement around an emitter in real space. For the clean QC surface, reference XPD patterns were collected on the core levels of Pd $3d_{5/2}$, Mn $2p_{3/2}$ and Al $2s$. The XPD measurements of the Cu films were performed on the Cu $2p_{3/2}$ core level. In Fig. 6.7 the

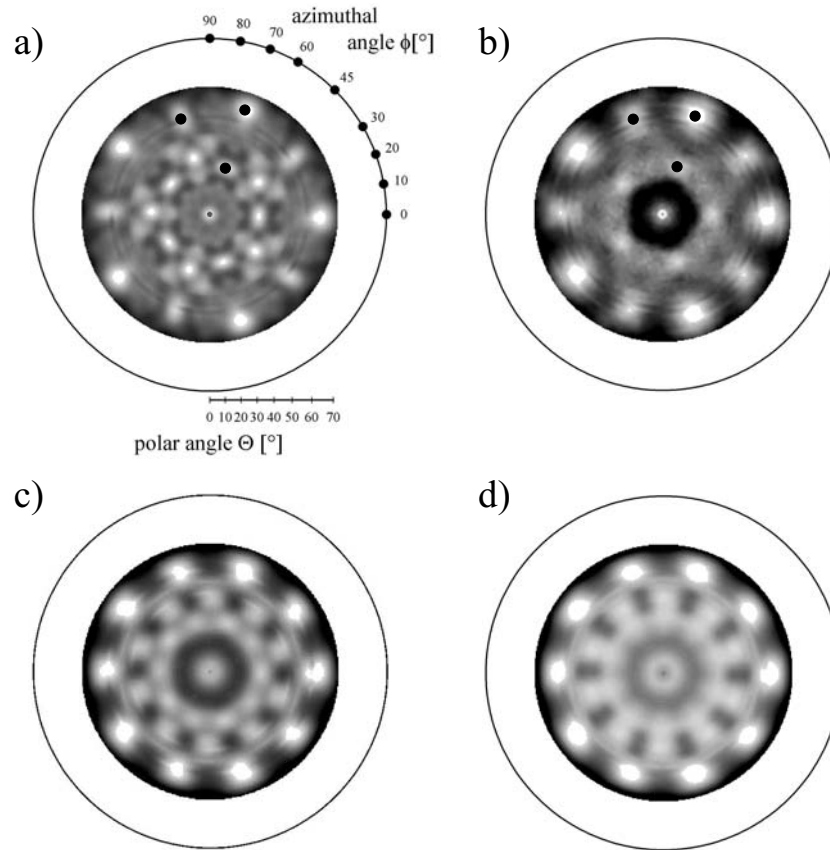


Figure 6.7: XPD patterns measured with Al $K\alpha$ radiation ($E_{kin}=1483.6\text{eV}$) for a) Pd $3d_{5/2}$ reference pattern of the QC substrate at $E_{kin}=1150\text{eV}$ b) 0.5ML Cu, pattern of Cu $2p_{3/2}$ core level at $E_{kin}=553.4\text{eV}$ c) 3ML Cu d) 4ML Cu

XPD patterns of the Cu $2p_{3/2}$ Level for 0.5ML, 3ML and 4ML Cu deposited are presented along with the Pd $3d_{5/2}$ pattern of the clean QC serving as a reference. At 0.5ML, weak forward focussing (FF) for small polar angles can be observed while strong FF is present for grazing angles. The pattern is clearly 5fold and the FF directions show strong similarity with the Pd pattern and is identically oriented as denoted by the black dots. FF features at the observed small angles imply at least 3 z-levels of atoms in the z-direction. It is reported that the island height in the submonolayer regime is around 1.9\AA by Ledieu et al. [9] and Cu preferentially fills pentagonal depressions present on the terraces at early stages of Cu film growth [10]. These depressions are in fact dissected Bergman clusters. Possible explanations for our XPD measurements are either some islands already present on top of the wetting Cu layer along with Cu sitting in these depressions or by some substitution or diffusion of Cu below the top QC layer. The strong chemical shift of the Cu $2p_{3/2}$ level with respect to bulk Cu in the submonolayer regime points to a strong

interaction of the Cu with the top QC layer. The pattern evolves gradually from a 5f to a 10f pattern up to a thickness of 3ML, from where on the Cu XPD patterns remain 10-fold. The corresponding Pd pattern (not shown) is not affected by the overlayer, and therefore, diffusion of Pd in the Cu layer is unlikely. This is further sustained by the fact that the Pd 3d core level E_B remains constant up to 3ML. However, it is worth noticing that the Pd core level is shifted to a lower E_B compared to the value of the clean QC surface indicating a chemical interaction between the Cu and Pd at the interface. The XPD pattern, while still 10f in nature, changes from 4ML upwards. In this range, the long range structure is established as seen by the reappearance of the LEED pattern and also in the stripe structure that starts to appear in STM. The change of the XPD pattern indicates that the local order is gradually lost as the FF-features at small emission angles are smeared out. This points to the reduction of the near atom order going along with a broader distribution of the near neighbor directions responsible for the smearing out in the XPD pattern. A transition of the copper film structure for Cu thickness above 3ML is also seen in the evolution of the Pd 3d_{5/2} core level E_B to the bulk value for Pd in a bare QC. This suggests a lowering of the chemical interaction of Cu with the QC substrate. To interpret the XPD patterns, it is important to understand, what local structures can produce a 5f or 10f pattern. A 5f pattern can develop either by a true pentagonal structure or by the superposition of patterns from 5 domains, rotated by 72° to each other and no rotational symmetry in the surface plane [15]. A 10f pattern can be produced by a true decagonal structure or the superposition of 5 domains, rotated by 72° to each other with 2 fold symmetry. The (110) surface of cubic structures does fulfill this condition, but goes even further. The inplane atomic positions share a $1:\sqrt{2}$ distance relationship normal to each other which is also reflected in the FF-directions in XPD. Upon 5 fold rotation individual FF-direction superimpose to form rings at characteristic polar angles (30°, 45°, 60°) with 10 maximas separated by a polar angle of 36°. Each of this rings is rotated by 18° with respect to the next. This is true for instance on bcc and fcc cut to expose the (110) surface. As an example, the XPD patterns of d-AlNiCo or the sputtered bcc-like (110) 5-domain termination of the former differ only by minor intensity variations on the polar angles [22]. A strong fingerprint on the nature of the local structure arises from the 4ML Cu film subjected to gentle heating. The corresponding XPD and LEED measurements for the heated 4ML film are summarized in Fig. 6.8. The sample was heated within 5min from RT to 250°C while observing the evolution of the LEED pattern. A gradual change in the LEED pattern was observed. This change results in a LEED pattern consistent with a fcc (110) surface with $4\text{Å} \times 2.82\text{Å} \pm 10\%$ surface mesh present in 5 domains, rotated by 72°C with respect to each other. The model matches in the whole energy range (40eV-100eV) probed. The corresponding XPD pattern changed from smeared out FF directions in the center (Fig. 6.7d) to well defined

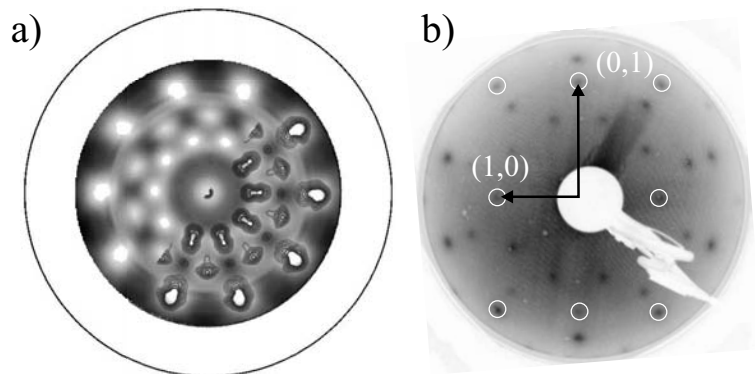


Figure 6.8: a) XPD pattern of the Cu $2p_{3/2}$ core level. In the lower left corner a contour Plot of an Cu(110) pattern subjected to 5f rotation averaging is superimposed to represent a Cu(110) structure present in 5 domains rotated by 72° . b) LEED pattern recorded at 60eV of the annealed Cu film. The circles mark the positions of spots expected for a fcc (110) surface termination. The basic reciprocal surface mesh vectors are denoted by arrows.

FF directions which closely resembles the observed XPD pattern of the unheated 3ML Cu film (Fig. 6.7c). A comparison to a measurement on bulk Cu(110) subjected to 5-fold rotation shows good agreement. The contour plot in the lower left corner of Fig. 6.8a was constructed by a experimental XPD pattern of Cu(110) subjected to 5f rotation to reflect a fcc surface with 5 domains (110) rotated by 72° . Therefore resuming: The results on LEED and XPD after gentle heating are in agreement with fcc domains rotated by 72° with respect to each other exposing the (110) surface. While the film showed no clear NN-structure (XPD) and quasiperiodic long range order (LEED) prior to heating, a clear NN-structure (XPD) and periodic long range order (LEED) has emerged by injecting energy into the system. We observed the same type of behavior as for the gently heated film when using a Omicron/Focus EFM3T triple E-Beam evaporator as a source. In these experiments, the quasiperiodic LEED pattern did not develop upon the Cu film growth. We directly observe LEED and XPD patterns that agree with a cubic structure. The reason for this behavior can be found in the working principle of the evaporator. This type of evaporator produces a non negligible degree of ions (around 2%) in the evaporand flux by design [23]. This ions impinge on the surface with kinetic energies in the range of 400eV-1000eV. Adding energy to the system, either by ions or by mild heating, obviously eliminates the quasiperiodic superstructure which can therefore be considered a rather unstable structure. Little energy is needed to establish a transition to the cubic structure on all length scales. Taking into account these observations, the similarity of the XPD patterns of 3ML as deposited and 4ML after heating is striking. These findings point to essentially identical local geometrical arrangement of the Cu atoms before the quasiperiodic superstructure emerges. The FF directions are identical and only minor intensity

variations at low polar angles are observed. Assuming identical underlying NN-structure, this can be explained by the higher thickness of the 4ML film prior to heating, leading to a more pronounced FF at small polar angles as more layers are involved in FF.

Due to this findings, we can propose a near neighbor structure for the unheated film which is essentially cubic, but only on the very local scale at a thickness around 3ML before the superstructure emerges. The appearance of the superstructure leads to a loss in average local order due to z-relaxation lying on the base of the observed quasiperiodic superstructure. Such relaxations are a fingerprint of an underlying strain driven mechanism.

6.4 Summary

In the present work, we investigated the growth of Cu thin films on a i-AlPdMn 5f single crystal surface in the low coverage regime by LEED, STM, XPS and XPD. We address the currently open question of the local atomic structure of the Cu film. At the early stages of the film growth, i.e. in the sub-monolayer regime, the Cu 2p_{3/2} XPD pattern shows a pentagonal symmetry with distinct inner structure. This is a strong indication that some degree of diffusion or substitution of Cu in the QC surface region takes place. Pentagonal depressions in the QC surface have been formerly proposed as adsorption sites for Cu in the initial stages of film growth [10]. According to our XPD data this is a possible explanation. Upon increasing the Cu film thickness up to 3ML the Cu XPD evolves to a 10f pattern which is in agreement with fcc(110) Cu present in 5 domains rotated by 72°. As the XPD evolves to the 10f pattern, LEED is disappearing indicating the loss of long range order, while near range order still is present. Abrupt changes take place in the transition from 3ML to 4ML: The spots in the Cu XPD pattern become broader and the inner pattern structure is smeared out, indicating a decrease in the local ordering of the Cu film. On the other hand, the LEED reappears showing a quasiperiodic k-spacing. As reported before [9], the STM shows the appearance of a 1D stripe super structure with a fibonacci sequence in the spacings between the stripes. The reappearance of the LEED can be explained by quasiperiodic phase coherence in the superstructure observed.

We propose that the film is well ordered on the scale of the photoelectron mean free path up to 3ML and not ordered on a long-range scale, while long range order is established along with a reduction in local order above 4ML. At the structural transition thickness between 3ML and 4ML, the Pd core level shifts back by 0.2eV to it's bulk value in the bare QC, suggesting a reorganization of Cu atoms in the whole film due to a change from strong substrate/film interaction to strong interaction of the Cu atoms among themselves. A possible mechanism explaining these observations can be found in a strain release of the Cu film between 3ML and 4ML thickness. Cu is known to undergo strain driven effects

in the investigated thickness regime below 10ML. It can undergo fcc-bct phase transitions due to substrate/film interaction [24] which are abrupt and depending on thickness (from 3ML to 4ML at RT). On various materials, buckled superstructures have been observed to release build up inplane strain [21, 25]. The appearance of the stripe pattern of Cu on Au(100) is also abrupt in the transition of 10ML to 11ML and goes along with a reorganization of the whole underlying film. A quasiperiodic strain relief pattern in the observed length scales of L and S can explain the loss in average NN-structure, as L and S are in the order of 2-3 near neighbors. Also, the LEED pattern can be explained by such an effect as the developed stripes are essentially z-relaxations spaced according to a Fibonacci rule in the necessary quasiperiodic phase coherence. The presented results do underline the need for a comprehensive approach, as no method by itself can solve the problem entirely. Only by taking into account different complementary methods it is possible to draw a complete picture.

6.5 Acknowledgements

Skillful technical assistance was provided by the mechanical and electronic work shop of the University of Fribourg and Empa. We would like to thank M. Feuerbacher [14] for providing us with high quality QC's. Furthermore, special thanks to J. Ledieu for intense and fruitfully discussion. This work was supported by the European Community through the SMART Quasicrystals Project No. G5RD-CT-2001-00584 whose financial support is greatly appreciated.

References for Chapter 6

- [1] D. Schechtman et al., Phys. Rev. Lett. **53**, 1951 (1984)
- [2] D.P. DiVincenzo, P.J. Steinhardt (Edts.), *Quasicrystals: The State of the Art*, (World Scientific, Singapore, 1999)
- [3] A.I. Goldman, R.F. Kelton, Rev. Mod. Phys. **65**(1), 213 (1993)
- [4] E. Rotenberg, W. Theis, K. Horn, Prog. Surf. Sci. **75**, 237 (2004)
- [5] C. Janot, *Quasicrystals: A Primer*, (Oxford, Clarendon, 1992)
- [6] Z.M. Stadnik (Edt.), *Physical Properties of Quasicrystals*, (Springer Verlag, Berlin, 2000)
- [7] A.I. Goldman, D.J. Sordelet, P.A. Thiel, J.-M. Dubois (Edts.), *New Horizons in Quasicrystals - Research and Applications*, (World Scientific, Singapore, 1997)
- [8] Ö. Rapp, Chapter 5 in Ref. [6]
- [9] J. Ledieu, J.-T. Hoefft, D.E. Reid, J. Smerdon, R.D. Diehl, T.A. Lograsso, A.R. Ross, R. McGrath, Phys. Rev. Lett. **92**, 135507 (2004)
- [10] J. Ledieu, R. McGrath, J. Phys. Condens. Matter, **15**, S3113 (2003)
- [11] J. Ledieu, R. McGrath, R.D. Diehl, T.A. Lograsso, D.W. Delaney, Z. Papadopolos, G. Kasner, Surf. Sci., **492**, L729 (2001)
- [12] C.S. Fadley in *Synchrotron Radiation Research: Advances in Surface Science* R.Z. Bachrach (Edt.), Vol. 1, 421-518, (Plenum, New York, 1990)
- [13] M. Petukhov, G.A. Rizzi, M. Sambì, G. Granozzi, Appl. Surf. Sci. **212-213**, 264 (2003) and references therein
- [14] Dr. Michael Feuerbacher, Institut fuer Mikrostrukturforschung Forschungszentrum Juelich GmbH D-52425 Juelich, Germany, EMail: m.feuerbacher@fz-juelich.de

- [15] D. Naumović, *Prog. Surf. Sci.* **75**, 205 (2004)
- [16] D. Briggs, M.P. Seah, *Practical Surface Analysis: Auger and X-Ray Photoelectron Spectroscopy*, Vol. 1, Second Edition, (John Wiley & Sons Ltd., New York, 1996)
- [17] J.C. Fuggle, E. Kallne, L.M. Watson, D.J. Fabian, *Phys. Rev. B* **16**, 750 (1977)
- [18] P. Ruffieux, P. Schwaller, O. Gröning, L. Schlapbach, P. Gröning, Q.C. Herd, D. Funnemann, J. Westermann, *Rev. Sci. Instrum.* **71**, 3635 (2000)
- [19] V. Fournée, A.R. Ross, T.A. Lograsso, P.A. Thiel, *Mat. Sci. Soc. Symp. Proc.* **805**, LL8.3.1 (2004)
- [20] R. Lüschnner, M. Erbudak, Y. Weisskopf, *Surf. Sci.* **569**, 163 (2004)
- [21] B.M. Ocko, I.K. Robinson, M. Weinert, R.J. Randler, D.M. Kolb, **83**, 780 (1999)
- [22] M. Shimoda, J.Q. Guo, T.J. Sato, A.-P. Tsai, *Surf. Sci.*, (**454-456**, 11 (2000)
- [23] J.Kirschner, H. Engelhard, D. Hartung, *Rev. Sci Instr.* **73**(11), 3853 (2002)
- [24] E. Hahn, E. Kampshoff, N. Wälchli, K. Kern, **74** 1803 (1995)
- [25] R.J. Randler, D.M. Kolb, B.M. Ocko, I.K. Robinson, **447**, 187 (2000)

Chapter 7

Formation of Al_4Cu_9 on the 5 fold surface of icosahedral AlPdMn

M. Biemann^{*†}, P. Ruffieux[†], O. Gröning[†], R. Fasel[†], R. Widmer[†], A. Barranco^{*†} and P.A. Gröning[†]

**Physics Department, University of Fribourg, Pérolles, CH-1700 Fribourg, Switzerland*

† Empa Materials Science and Technology, Überlandstrasse 129, 8600 Dübendorf, Switzerland

to be submitted

In this work, we present the formation of Al_4Cu_9 upon heating of a thermally evaporated 7.8nm Cu film on the fivefold surface of a icosahedral $\text{Al}_{70}\text{Pd}_{20}\text{Mn}_{10}$ single crystal. The analysis was performed using Low Energy Electron Diffraction, X-ray Photoelectron Diffraction and X-ray Photoelectron Spectroscopy. The alloy formed at the surface has a $\text{Al}_{4.3}\text{Cu}_{8.7}$ stoichiometry. It is well ordered and is present in 5 domain which are rotated by 72° with respect to each other and expose the (110) surface. The surface mesh is evaluated as $12.3\text{\AA} \times 8.7\text{\AA}$, which is in agreement with the $\sqrt{2} \times 1$ surface mesh of a cubic unit cell with $a=8.7\text{\AA}$ cut along its (110) plane. The local structure agrees with an average B2(CsCl) structure, a common feature of approximant phases. This findings are in accordance with an Al_4Cu_9 alloy which has already been identified as a quasicrystal approximant.

7.1 Introduction

Quasicrystals have since their discovery in 1984 by Schechtman [1] attracted great interest because of the unique structural, electronic and surface properties. This combination of properties have made them especially interesting not only from a fundamental point of view [2]. Low friction, high wear resistance, low surface energy and apparent resistance to oxidation has led to the fact that great potential is attributed to them from an application perspective as non-stick and tribological coating. While a tremendous amount of work has been devoted on the surface properties of these materials [3–6], it's benefits are only used in very specialized applications [7]. One of the major hindrances is inherently due to the low surface energy of these materials: It leads to a dewetting of the coating to the substrate material. In view of applications, it is clear that not only the surface of these materials is of mayor importance, also the interface to a potential substrate deserves attention, especially for brazing and alloy formation - two important topics for coatings. From a fundamental point of view, the growth of an approximant overlayer on a QC is interesting. Approximants are crystals with translational symmetry and very large unit cell, but locally have a very similar structure to Quasicrystals (QC) [8]. Their valence electron concentration follows the same empirical rule as QC's. They are considered as periodic model systems to QC's [9]. In this work, we focus on the alloy formation of a Cu thin film with a i-AlPdMn QC whose surface is oriented normal to it's 5 fold (5f) axis upon short annealing. The compositional stoichiometry is estimated using X-ray Photoelectron Spectroscopy (XPS). The Nearest-Neighbour (NN) geometry of the film is probed by X-ray Photoelectron Diffraction (XPD) [10,11] while Low Energy Electron Diffraction (LEED) gives us quantitative data about the inplane surface mesh values. These two methods have already proven to be valuable and complementary in assessing this type of problems [12].

7.2 Experimental

All experiments were performed in a modified Omicron photoelectron spectrometer equipped with an EA 125 HR electron analyzer. The base pressure of the system is $5 \cdot 10^{-11}$ mbar. For XPS and XPD, we used non-monochromatized Al K α (1486.6eV) radiation. The spectrometer is calibrated to a Au 4f_{7/2} binding energy (BE) of 83.8eV and was operated in Constant Analyzer Energy (CAE) mode with 80eV pass energy for overview spectra and 20eV for detail spectra. By XPS, we probe the composition and chemical nature in a near-surface region of 3Λ (Λ = electron mean free path) which is in the range of 2-5nm. Structural information of the surface is gained by LEED, which probes 50\AA lateral and around 5\AA normal to the surface [13]. LEED can give quantitative numbers of the sur-

face mesh present. XPD yields information about the NN geometrical arrangement of a sample in the analysis depth of XPS. This is achieved by the so called Forward Focussing (FF) effect, the preferential photoelectron emission along NN directions around a photoelectron emitter [10]. It is usual practice to plot the photoelectron emission intensity in stereographic projection as a function of polar and azimuthal angles. This technique - in contrast to LEED - reflects the real space structure around a certain emitter type. We used an AlPdMn single crystals, grown by the Czochralsky technique at the IMF in Jülich [14]. The sample was cut to exhibit the 5 fold surface and mechanically polished. The single crystal was prepared by repetitive cycles using Ar ion sputtering cycles (30min, 1.5keV ion energy) followed by annealing (640°C for 2h, pyrometer emissivity set to $\epsilon = 0.35$, Model Marathon MA2B). The sample cleanliness and structural quality was checked by XPS (absence of O Auger in XPS) as well as the LEED pattern. After the final sputter/annealing cycle the LEED spots in the energy range of 10eV-380eV can be observed. STM shows a terraced structure with an average width of about 100nm and terrace lengths generally well exceeding this value before evaporation of the Cu film. The thin films were evaporated *in situ* with a resistively heated Cu evaporator while the

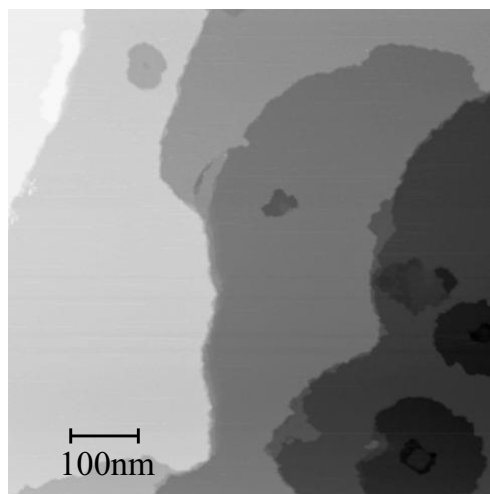


Figure 7.1: Typical 500nm x 500nm STM picture of the clean QC surface. The terraces are flat and the step heights are related by τ as expected for the surface plane normal to the 5f axis.

sample was held at room temperature (RT) during evaporation. Film thickness was calibrated using a Quartz Crystal Monitor. The thickness of the Cu film was chosen as to completely eliminate contributions of the substrate in the analysis depth of XPS before and after heating. The evaporation rate used was 1Å per min. 7.8nm of Cu have been deposited before heating the sample. The base pressure of the chamber was always below 10^{-9} mbar during preparation and in the low 10^{-10} mbar regime during analysis. The film

was heated after evaporation to 350°C while observing the evolution of the LEED pattern until the new pattern developed. The heating time is mainly dominated by the thermal inertia of the sample holder and the time at the annealing temperature is in the range of 1min. A comprehensive study of the unheated Cu films on i-AlPdMn5f are presented elsewhere [15, 16].

7.3 Results and Discussion

7.3.1 XPS Measurements

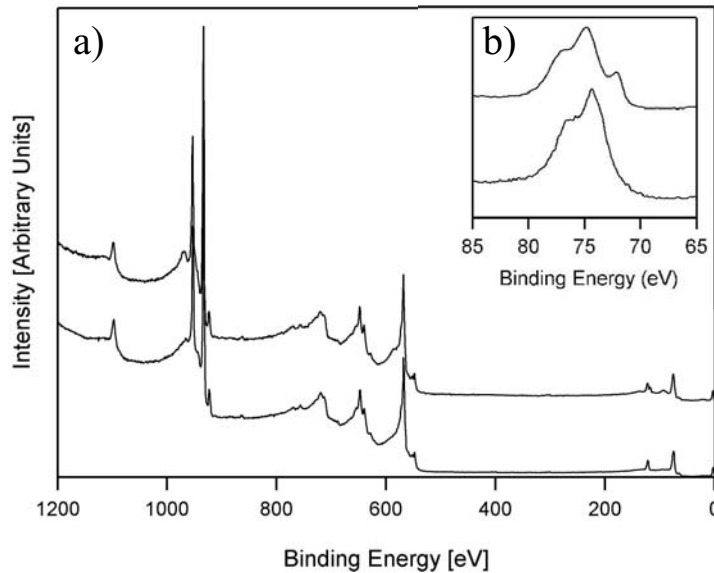


Figure 7.2: XPS spectra a) Overview before and after annealing b) Detail spectra of the Cu 3p and Al3p region. The lower spectra denote the measurements on the sample prior heating while the upper spectra represent data taken on the heated sample.

Before heating, the XPS spectra only shows Cu signals as depicted in Fig. 7.2. After heating the sample, Cu and Al signals can be observed. It is important to note, that no signal of Pd, namely the Pd 3d and Pd Auger levels - the strongest components of the clean QC spectrum - can be observed. Therefore, we can conclude, that the Al signals are due to diffusion of Al from the QC into the Cu layer. Figure 7.3 shows the detail spectra of Cu 3s and Al 2s after heating of the sample. The individual peak parameters are summarized in Table 7.1. A peak shift of the Cu $2p_{3/2}$ of 0.7eV to higher E_B can be observed upon heating. This indicates an electron transfer from Cu to the more electronegative Al as a result of alloy formation. Similar peak shifts have also been observed in other AlCu-alloys [17]. Also a slight broadening of the Cu $2p_{3/2}$ core level is observed. From this

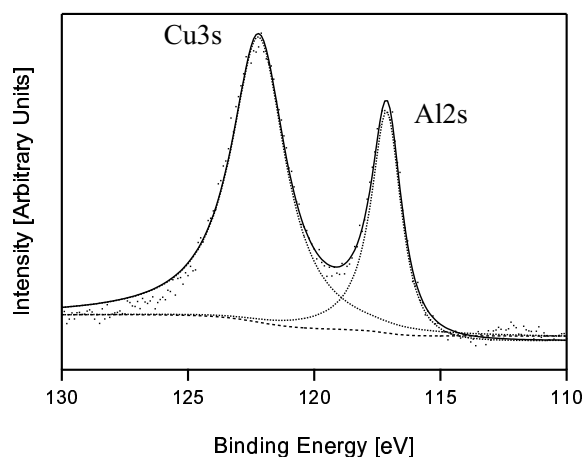


Figure 7.3: XPS detail spectra of the Cu 3s and Al 2s core levels after heating of the film.

core level	E_B [eV]	FWHM[eV]
Cu $2p_{3/2}$ *	932.4	1.25
Cu $2p_{3/2}$	933.1	1.43
Cu 3s	122.2	2.7
Al 2s	117.1	1.54
Al 2p	72.1	1.31

Table 7.1: Peak Parameters as evaluated from the XPS measurements. The value marked by * is evaluated from the unheated film and complies the metallic Cu bulk value.

evaluation we get an Al/Cu ratio of $0.49 \pm 10\%$. In the AlCu phase diagram, the Al_4Cu_9 alloy is within experimental error [19]. The experimental error was estimated based on the anisotropy of photoelectron emission from single crystal surfaces - the principle on which XPD is based on.

7.3.2 XPD Analysis

We investigate the local structure of the film by XPD and compare the measurements with Single Scattering Cluster (SSC) Calculations based on an appropriate structural model. In SSC, the diffraction of photoelectrons is calculated by assuming that the scattering of excited waves on the surrounding atoms of an emitter are independent processes. While this is a simplification to reality, as multiple scattering of the individual waves is neglected, it reproduces the FF directions very well [10, 20, 21]. The corresponding XPD pattern of the heated Cu film on i-AlPdMn 5f are presented in Fig. 7.4 along with the SSC patterns in stereographic projection of the intensity as a function of azimuthal and polar angle

(up to $\theta=70^\circ$). We measured at the Cu 3s and Al 2p positions because the high kinetic energy favors the FF effect. The patterns are 10fold in nature. The measurements on the Cu 3s and Al 2p core levels do agree very well with SSC Calculations based on a (110) termination of the Al_4Cu_9 surface structure present in 5 domains, rotated by 72° with respect to each other as presented in Fig. 7.4. Analysis of the Al_4Cu_9 pattern in

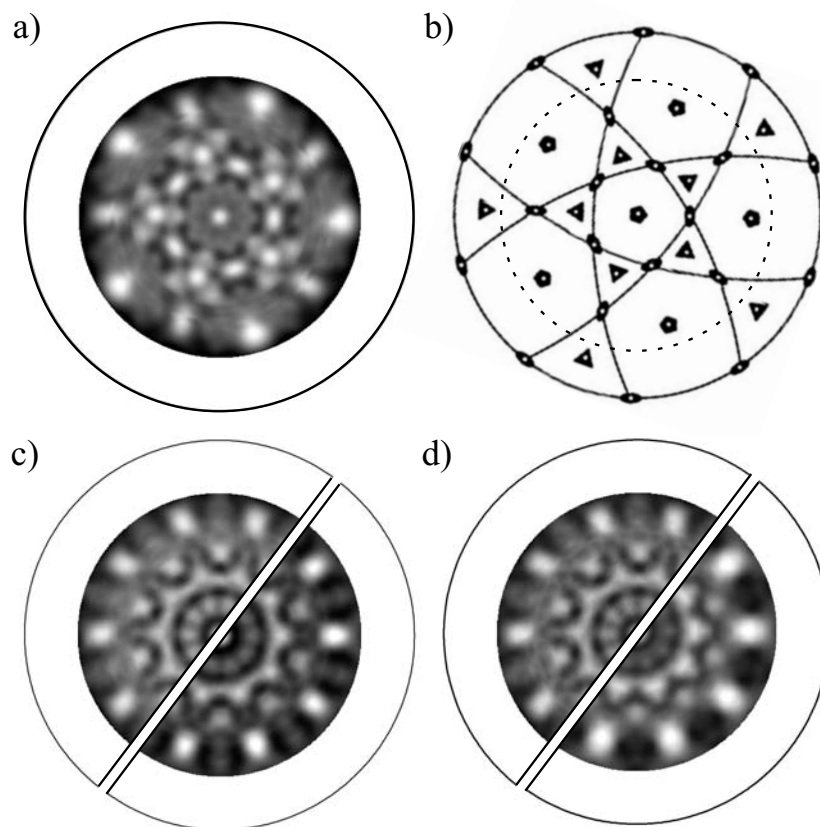


Figure 7.4: XPD pattern in stereographic projection a) Pd $3d_{5/2}$ core level of the clean QC before evaporation b) Stereographic projection of the icosahedral symmetry elements with 2f (ellipse), 3f (triangle) and 5f (pentagonal) symmetry axes. The dotted line represents the measurement window c) Cu 3s core level and the d) Al 2p core level. The lower half of c) and d) are overlaid with a SSC simulation of (110) terminated Al_4Cu_9 subjected to 5f superposition for the Cu and Al emitters respectively.

comparison with the QC pattern based on a structural model and the FF-Features allows us to restrict the possible orientations of the unit cell with respect to the substrate. By such an analysis, we find that the inplane pentagonal features of the Al_4Cu_9 (110) plane are either equally oriented or rotated by 36° with respect to the pentagonal features of the QC.

7.3.3 LEED Analysis

The LEED pattern on the alloy is 10f in nature and shows a multitude of spots at low energy, indicating a large surface mesh. Measurements at two energies probed are depicted in Fig. 7.5. Assuming an underlying cubic structure, the 10f nature of the spot pattern points to a surface mesh with $\sqrt{2} \times 1$ relation of the surface unit mesh vectors, present in 5 orientations related by a 72° rotation. Indeed, the surface mesh agrees with a $12.3\text{\AA} \times 8.7\text{\AA}$ ($\pm 10\%$) surface mesh structure present in 5 domains rotated by 72° with respect to each other. This surface mesh is in agreement with the cubic Al_4Cu_9 structure (lattice constant 8.7\AA), exposing the (110) surface. Based on this structure, the weighted reciprocal space (reciprocal space taking into account the structure factor) has been calculated [22] and presented as an overlay to the pattern b). The spectral weight is represented by the size of the spots. It is important to note, that along the (1,0) direction, only the (3,0) spot has appreciable intensity. The pattern perfectly match, although the spectral weight of the (2,1) spot is slightly overestimated. Al_4Cu_9 is a cP54 structure with space group $P\bar{4}3m$ [19]

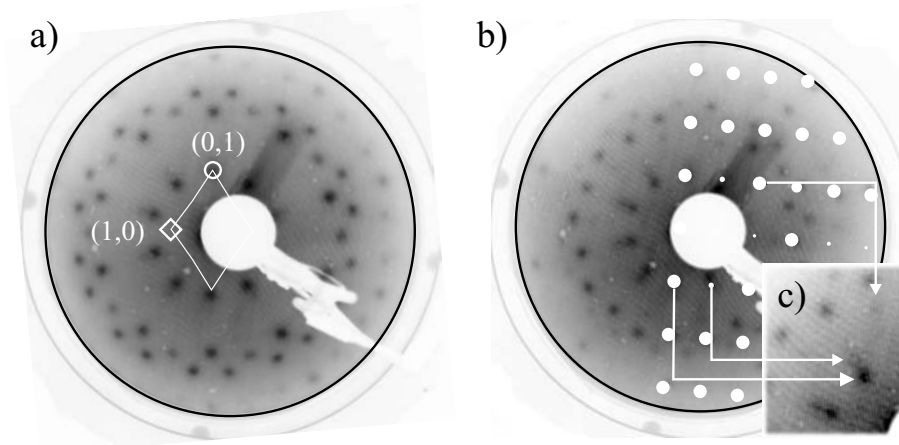


Figure 7.5: LEED patterns of the heated Cu film. The pattern can be explained by a 5 domain structure, rotated by 72° with surface mesh of $12.3\text{\AA} \times 8.7\text{\AA}$. a) taken at 35eV. \circ mark the (0,1) spot while \diamond marks the (1,0) spot, note that the later is absent due to the structure factor b) taken at 45eV. Superimposed is the reciprocal surface mesh. The (1,0) spots are absent. c) Blow up of the low index spots, the (0,1), (1,1) and (2,1) spots are marked by arrows

and basis $a=8.7\text{\AA}$. This structure can be represented by a $3 \times 3 \times 3$ CsCl superstructure with 2 unoccupied sites and has been identified by Dong et al. as a QC approximant [23]. In his paper, the structure is extensively discussed. The unit mesh consists of 6 layers along the z-axis with sequence FPpfp'P'F ((f,F)=flat layers, (p,P,p',P')=puckered layers). f and p are related to F and P by a n-type mirror operation lying at the middle of P and p with $\frac{1}{2}[110]$ translation. P' and p' are related to P and p by mirrors lying on F and

f respectively. The structure is presented in Fig. 7.6. For indepth information about the layer structure, the reader is referred to [23]. These symmetries lead to the observed behavior of the structure factor in the LEED pattern. The strongest spots in the LEED measurements at 60eV (not shown) lie at $k=2.91\text{\AA}^{-1}\pm 10\%$ which is in agreement with the value of the most intense spot $Q_{intense}=3.062\text{\AA}^{-1}$ for the Hume-Rothery type alloy Al_4Cu_9 [23, 24]. Finally, it is important to note at this point, that the LEED pattern cannot stem from a decagonal surface, as the LEED spots do not share a τ -relationship in k .

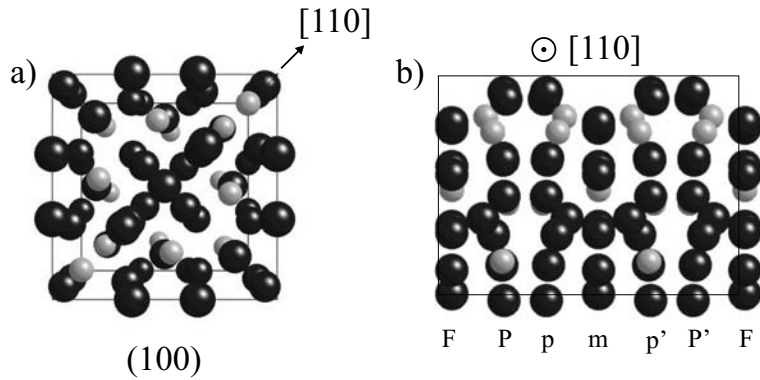


Figure 7.6: a) unit cell of Al_4Cu_9 containing 52 atoms b) structure projected along the $[110]$ direction. Dark spheres represent Cu and light spheres Al atoms.

7.4 Summary

We have investigated Cu films deposited on i-AlPdMn 5f QC's after heating to 350°C . The composition of XPS is in agreement with Al_4Cu_9 within experimental error. LEED and XPD both show that the surface is oriented in a (110) orientation and is present in 5 domains, rotated by 72° to each other. The XPD patterns can be well reproduced by SSC Calculations based on the Al_4Cu_9 structure and the LEED data does match the expected pattern as well as intensities of Al_4Cu_9 . Along the $(1,0)$ axis, only the $(3,0)$ spots have appreciable intensity. This finding is well reproduced and can be related to the symmetry of the surface of Al_4Cu_9 in the (110) surface plane. It has been noted by Dong [23] that the layer stacked along the (110) direction do have a stacking sequence and periodicity that resemble those of the d-AlMn QC phase along it's $10f$ axis. The basic pentagons formed around the vacancy sites are aligned into pentagonal columns along the same direction. XPD confirms the same orientational relationship of the pentagonal features in the formed Al_4Cu_9 film and the substrate. We therefore think that the formation of Al_4Cu_9 on the i-AlPdMn 5f is promoted by the fact that they are structurally closely

related. It has been observed in heated Al/Cu multilayer films that in the presence of excess Cu, the formation of Al_4Cu_9 is favored [25]. As the Al stems from the top layers of the Al-terminated AlPdMn QC [26], this is plausible to take place in the presented case .

7.5 Acknowledgements

Skillful technical assistance was provided by the mechanical workshops of the University of Fribourg and Empa. We would like to thank M. Feuerbacher [14] for providing us with high quality QC's. Furthermore, special thanks to J. Ledieu for intense and fruitfully discussion. This work was supported by the European Community through the SMART Quasicrystals Project No. G5RD-CT-2001-00584 whose financial support is greatly appreciated.

References for Chapter 7

- [1] D. Schechtman et al., Phys. Rev. Lett. **53**, 1951 (1984)
- [2] C.J. Jenks, P.A. Thiel, Langmuir **14**, 1392 (1998)
- [3] D.P. DiVincenzo, P.J. Steinhardt (Edts.), *Quasicrystals: The State of the Art*, (World Scientific, Singapore, 1999)
- [4] C. Janot, *Quasicrystals: A Primer*, (Oxford, Clarendon, 1992)
- [5] Z.M. Stadnik (Edt.), *Physical Properties of Quasicrystals*, (Springer Verlag, Berlin, 2000)
- [6] A.I. Goldman, D.J. Sordet, P.A. Thiel, J.-M. Dubois (Edts.), *New Horizons in Quasicrystals - Research and Applications*, (World Scientific, Singapore, 1997)
- [7] J.M. Dubois, P. Weinland, P. CNRS, Nany, France, Coating Materials for Metal Alloys and Metals and Method, Eur. Patent EP 0356287 A1 and U.S. Patent 5,204,191, April 20, 1993
- [8] A.I. Goldman, R.F. Kelton, Rev. Mod. Phys. **65**(1), 213 (1993)
- [9] M. Boudard, H. Klein, M. de Boissieu, M. Audier, H. Vincent, Phil. Mag. A **74**, 939 (1996)
- [10] C.S. Fadley in *Synchrotron Radiation Research: Advances in Surface Science* R.Z. Bachrach (Edt.), Vol. 1, 421-518, (Plenum, New York, 1990)
- [11] D. Naumović, Prog. Surf. Sci. **75**, 205 (2004)
- [12] M. Petukhov, G.A. Rizzi, M. Sami, G. Granozzi, Appl. Surf. Sci. **212-213**, 264 (2003) and references therein
- [13] R. Lüschnner, M. Erbudak, Y. Weisskopf, Surf. Sci. **569**, 163 (2004)
- [14] Dr. Michael Feuerbacher, Institut fuer Mikrostrukturforschung Forschungszentrum Juelich GmbH D-52425 Juelich, Germany, EMail: m.feuerbacher@fz-juelich.de

- [15] J. Ledieu, J.-T. Hoefft, D.E. Reid, J. Smerdon, R.D. Diehl, T.A. Lograsso, A.R. Ross, R. McGrath, *Phys. Rev. Lett.* **92**, 135507 (2004)
- [16] To be published
- [17] J.C. Fuggle, E. Kallne, L.M. Watson, D.J. Fabian, *Phys. Rev. B* **16**, 750 (1977)
- [18] P. Ruffieux, P. Schwaller, O. Gröning, L. Schlapbach, P. Gröning, Q.C. Herd, D. Funnemann, J. Westermann, *Rev. Sci. Instrum.* **71**, 3635 (2000)
- [19] P. Villars, L.D. Calvert, *Pearson's Handbook of Crystallographic Data for Intermetallic Phases*, (American Society for Metals, Metals Park, 1985)
- [20] J. Osterwalder, T. Greber, A. Stuck, L. Schlapbach, *Phys. Rev. B* **44**, 13764 (1993)
- [21] R. Fasel, PhD thesis, University of Fribourg (1996)
- [22] SingleCrystal Module from CrystalMaker 6.3.8, CrystalMaker Software Ltd, www.crystallmaker.com
- [23] C. Dong, *Phil. Mag. A* **73**(6), 1519 (1996)
- [24] C. Dong, A. Perrot, J.-M. Dubois, E. Belin, *Mat. Sci. Forum*, **150-151** 403 (1994)
- [25] H.G. Jiang, J. Y. Dai, H.Y. Tong, B.Z. Ding, Q.H. Song, Z. Q. Hu, *J. Appl. Phys.* **74**(10), 6165 (1993)
- [26] M. Gierer, M.A. Van Hove, A. I. Goldman, U. Shen, S.-L. Chang, P.J. Penhero, C.J. Jenks, J.W. Anderegg, C.-M. Zhang, P.A. Thiel, *Phys. Rev. B*, **57**(13), 7628 (1998)

Danksagung

Es war ein langer Weg bis zu diesen Zeilen, begleitet von vielen guten und auch erschwerlichen Momenten. Natürlich hat alles viel länger gedauert als geplant - der Umzug und Aufbau der Forschungsgruppe in Thun hatte da sicher einen wesentlichen Einfluss. Es war eine Zeit der persönlichen Erfahrungen und Veränderungen. Es gab viele Höhen und Tiefen - und nicht immer war der Kontakt zu mir einfach. Viele Leute haben mich auf meinem Weg begleitet - sei es direkt bei der Arbeit oder durch ihre Präsenz im Privaten. An dieser Stelle möchte ich diesen Personen persönlich danken. Natürlich kann diese - alphabetisch geordnete - Liste nicht vollständig sein. Dies soll meine Wertschätzung nicht mindern.

Meine Betreuer

- Pierangelo Gröning : Danke für deinen Beistand und dass du mir die Möglichkeit geben hast, in deiner Gruppe an der Empa meine These zu beenden. Unsere Denkweisen und Ansätze sind sehr verschieden, das hat wesentlich zum Erfolg beigetragen.
- Louis Schlapbach : Der mich seit meinem Studium begleitet hat. Er hat mir ermöglicht, meine Diplomarbeit und den ersten Teil meiner Doktorarbeit in seiner Gruppe zu machen. Unser Kontakt war nie ein übliches Chef/Angestellten Verhältnis was ich sehr geschätzt habe.

Meine Arbeitskollegen

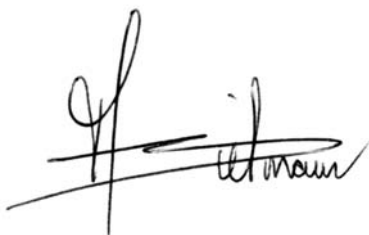
- Angel Barranco, Gilles Buchs, Patrick Schwaller, Roland Widmer
- Oliver Gröning : Der Geburtshelfer und Bändiger von Igor dem Schrecklichen. Er hat mir während der Wehen das Händchen gehalten und mir kreativen Input geliefert. Damit ist deine G*****-Schmach getilgt;-)
- Pascal Ruffieux : Der mich sowohl in fachlichen Fragen ein wichtiger Gesprächspartner war als auch Privat mich immer wieder fordert. Der Anblick deiner Hinterreifen beim Fahrrad sind mir sehr vertraut...
- Das administrative und technische Personal der Universität Freiburg und Empa Thun: Elisabeth Francois, Francis Bourqui, Oswald Raetzo, Elmar Mooser, Roland Schmid, Roger Vonlanten, Cédric Mora, Katrin Gurtner, Eveline Strubhaar, Christian Kauer, Gerhard Burki, Anton Böll und andere mehr. Danke für eure präzise und speditive Arbeit

- Alle Mitglieder der früheren Forschungsgruppe für Festkörperphysik der Universität Fribourg von L. Schlapbach. Viele von Ihnen waren in Teilaspekten meiner Arbeit involviert.

Meine Freunde

- Anna Stradner : Mit der mich eine aussergewöhnliche Freundschaft verbindet. Mehr Worte sind überflüssig.
- Christian Koitzsch : Mein guter Freund und Kollege. Ich schätze deinen Rat, der mich so oft wieder auf den Boden der Tatsachen gebracht hat. Aber pass auf: Ich werde dich im Squash noch mal schlagen!
- Michael Vogt : Deine direkte Art war Anfangs ungewohnt für mich, aber ich habe daraus gelernt, wieviel man durch so einen Weg gewinnen kann. Danke für die guten Gespräche und natürlich die guten Drinks. Wir haben viel zusammen erlebt.
- Anne Lanz, Chantal Egli, Daniel Nettels, Georg Bison, Isabelle Sturny, Katya Rüesch, Nicole Kaeser, Olivier Dessibourg, Sarah Heinzer, Tiana Nicolet
- Meine Eltern/Familie : Welche mir das Studium ermöglichen haben und mich niemals in meinen Entscheidungen einzuschränken versucht haben.

Danke das ihr mich so nehmt wie ich bin (oder wenigstens so tut als ob:-) - Ihr könnt immer auf mich zählen - whatever it takes. Worte vermögen nur unzureichend auszudrücken, wie wichtig ihr für mich seid.



Michael Biemann

Curriculum vitae

Personal details

Family name	Bielmann
First name	Michael
Date of birth	Juli 02, 1974
Place of birth	Fribourg, Switzerland
Nationality	Swiss
Status	Single

School

1980 - 1989	Basic education in Rechthalten/Plaffeien FR
1989 - 1993	High School in Fribourg, College St. Croix, Science Matura Type C

Studies

1994 - 1998	Studies in Physics University of Fribourg, Switzerland
1998	Diploma work in Solid State Physics: <i>"Charakterisierung der Adsorption von Proteinen auf Oberflächen"</i> under the direction of Dr. M. Collaud-Coen
Aug. 1999 - 2002	PhD student in the Solid State Physics Group of Prof. Dr. Louis Schlapbach University of Fribourg, Switzerland
Jan. 2003 - today	PhD student in the group nanotech@surfaces of Dr. Pierangelo Gröning Empa, Thun, Switzerland

Publications

1. Charge-density oscillation on graphite induced by the interference of electron waves
P. Ruffieux, P. Gröning, M. Melle-Franco, F. Zerbetto, O. Gröning, M. Biemann
submitted to Phys. Rev. B
2. Hydrogen chemisorption on sp²-bonded carbon: Influence of the local curvature and local electronic effects
P. Ruffieux, O. Gröning, M. Biemann and P. Gröning
Appl. Phys. A **78**, 975 (2004)
3. AgO investigated by photoelectron spectroscopy: Evidence for mixed valence
M. Biemann, P. Schwaller, P. Ruffieux, O. Gröning, L. Schlapbach, and P. Gröning
Phys. Rev. B **65**, 235431 (2002)
4. H₂ plasma treatment of silver contacts: impacts on wirebonding performance
M. Biemann, P. Ruffieux, P. Schwaller, P. Sudan, L. Schlapbach and P. Gröning
J. Electron. Mat. **31**, 1316 (2002)
5. Hydrogen adsorption on sp²-bonded carbon. Influence of the local curvature
P. Ruffieux, O. Gröning, M. Biemann, P. Mauron, L. Schlapbach and P. Gröning
Phys. Rev. B **66**, 245416 (2002)
6. Supramolecular columns of hexabenzocoronenes on copper and gold (111) surfaces
P. Ruffieux, O. Gröning, M. Biemann, C. Simpson, K. Mullen, L. Schlapbach and P. Gröning
Phys. Rev. B **66**, 073409 (2002)
7. Adsorption and Bioactivity of Protein A on Silicon Surfaces Studied by AFM and XPS
M. Collaud Coen, R. Lehmann, P. Gröning, M. Biemann, C. Galli, L. Schlapbach
Journal of Colloid and Interface Science **233**, 180-189 (2001)